

PHASE FIELD CRYSTAL MODELING OF
NANOCRYSTALLINE MATERIALS

DENSITY FUNCTIONAL MODELING OF MECHANICAL
PROPERTIES AND PHASE TRANSFORMATIONS IN
NANOCRYSTALLINE MATERIALS

By

PETER STEFANOVIC, B. ENG.

A Thesis Submitted to the School of Graduate Studies in
Partial Fulfilment of the Requirements for the Degree Doctor
of Philosophy

McMaster University
©Copyright Peter Stefanovic, 2008

DOCTOR OF PHILOSOPHY McMaster University
Materials Science And Engineering Hamilton, Ontario

TITLE: Density functional modeling of mechanical
 properties and phase transformations
 in nanocrystalline materials.
AUTHOR: Peter Stefanovic, B. ENG.
SUPERVISOR: Professor Nikolas Provatas
NUMBER OF PAGES: xv, 174

Abstract

We introduce a new phase field technique that incorporates the periodic nature of a crystal lattice by considering a free energy functional that is minimized by periodic density fields. This free energy naturally incorporates elastic and plastic deformations and multiple crystal orientations. The new phase field technique can be used to study a host of important phenomena in material processing that involve elastic and plastic effects in phase transformations. This novel phase field approach is used to study elastic and plastic deformation in nanocrystalline materials with a focus on the "reverse" Hall-Petch effect. In addition we apply the method to dendritic solidification in binary alloys and the role of dislocations in spinodal decomposition.

Acknowledgements

This thesis has been done at McMaster University in Hamilton. The work was performed at the Department of Materials Science and Engineering in computational materials science research group of Dr. Provatas. During my time at McMaster I've met a lot of people who have contributed to my learning process and the completion of this work.

First and foremost, I would like to thank my supervisor, Prof. Nikolas Provatas, for his guidance and support. Not only a great mentor, he has also been a cornerstone in my professional development. I would also like to thank Prof. Mikko Haataja for many useful discussions and debates that helped clear up lots of theoretical and technical issues.

During the course of this work I benefitted from comments and discussions with members of my supervisory committee: Prof. J. David Embury, Prof. Marek Niewczas, Prof. David S. Wilkinson, and Prof. Hatem S. Zurob.

Furthermore, I wish to thank Mark Hahn, an administrator of a high performance computers network (Sharcnet), for helping me with technical aspects of my computational simulations.

Finally, I would like to thank my parents and family for their love and care. Most of all I want to thank my dear Renée for her love and support.

Contents

Abstract	iii
Acknowledgements	iv
1 Introduction	1
I Literature Review and Main Issues	8
2 Processing and Characterization of Nanostructured Metals and Alloys	9
2.1 Categorization of Nanostructured Materials	9
2.2 Processing Techniques	10
2.3 Characterization of NC Materials	12
2.3.1 Density	13
2.3.2 Determination of Grain Size	14
3 Mechanical Properties of Nanostructured Metals and Alloys	15
3.1 Mechanical Testing	16
3.1.1 Elastic Properties	16
3.1.2 Grain Size Dependence of Strength	17
3.1.3 X-ray Diffraction and Microscopic Studies	23
3.2 Computer Simulation Studies	26
3.2.1 Current Status and Limitations	31
4 Deformation Mechanisms of Nanocrystalline Metals: A Summary	34
4.1 Microcrystalline Metals	34
4.2 Ultrafine Crystalline Materials	36
4.3 Nanocrystalline Materials	37
4.3.1 NC Materials - Strength Above Critical Grain Size	37
4.3.2 Softening of NC Materials - Strength Below Critical Grain Size	38

5	Compositional Domain Boundaries and Strengthening: Role of Dislocations in Spinodal Decomposition	42
6	Summary of Outstanding Issues	47
II	Phase Field Crystal Modeling of Nanocrystalline Materials	48
7	A New Atomistic Modeling Formalism	51
7.1	Atomic Density Field and Particle Interactions	52
7.1.1	Atomic Density	52
7.1.2	Correlation Function	55
7.2	Density Functional Theory and Phase Field Crystal Models	58
7.3	Free Energy and the Equilibrium Phase Diagram of a Pure Material .	60
7.3.1	Properties of the Free Energy in One Dimension	61
7.3.2	Properties of the Free Energy in Two Dimensions - Phase Diagram	62
7.3.3	Elastic Properties	64
7.3.4	Diffusional Dynamics	65
8	A New Phase Field Crystal Formalism: Incorporating Dynamic Elastic Interactions	67
8.1	Floquet Stability Analysis	69
8.2	Comparison with Hydrodynamics of Isothermal Solids	71
8.3	The Diffusive Limit of the Model: Polycrystalline Nucleation and Growth	73
8.4	Grain Boundary Interactions	76
8.5	Elastic Strain Relaxation Properties of the Model	78
9	Extension to Binary Alloys	81
9.1	Free Energy Functional for a Binary Alloy	82
9.2	Liquid Phase Properties	84
9.3	Crystalline Phase Properties	86
9.4	Simple Binary Alloy Model	87
9.4.1	Solid-Solid Coexistence of Phase Diagram	90
9.4.2	Solid-Liquid Coexistence	90
9.5	Calculation of Alloy Phase Diagrams	91
9.6	Dynamics	94
9.7	Dendritic Solidification	97
10	Efficient Semi-Implicit Solver Development	101
10.1	Iterative Solver	102
10.2	Multigrid Solver	103

10.2.1 Introduction	103
10.2.2 The Components of Multigrid	107
10.3 Convergence and Efficiency of Multigrid Solver	111
III Application of Phase Field Crystal Modeling to the Study of Strengthening Mechanisms	114
11 Deformation of Nanocrystalline Materials	116
11.1 Initial Conditions and Boundary Conditions	116
11.2 Strain Application	118
11.3 Strain Rates	119
11.4 Crystal Structure	120
11.5 Strain Measurements and Data Interpretation	120
11.6 Dislocation Glide	121
11.7 Modeling Strain Concentration and Fracture of Nanocrystals	123
11.8 Deformation in Polycrystalline Material	126
11.9 Applications to Spinodal Decomposition	139
12 Extension to Three Dimensions	146
13 Conclusion	149
Appendices	151
A Deriving the New Phase-Field Crystal Model Starting from Hydro- dynamics of Solids	152
B Derivation of Simple Binary Alloy Model	156
C Multigrid - Full Approximation Scheme	159

List of Figures

2.1	Severe plastic deformation method. Left: Equal-channel angular pressing setup. Right: High-pressure torsion setup [32].	11
2.2	Left: Stress-Strain results of tensile tests on NC powder. Beneficial effects of polishing. Surface flaws were related through Griffith criteria to a critical surface crack with a magnitude of about $2\mu\text{m}$ frequently observed in 'as compacted' NsM. Right: Influence of porosity on the Vickers hardness. Straight line: best 'fit' to the data for samples with average density 87-94%; Data points: sample with average density above 98%. Figures adapted from: [25, 39, 40].	13
3.1	Hall-Petch plot for Cu alloy [1].	15
3.2	Variation in hardness with $d^{-1/2}$ for NC Cu and Pd reported for the first time by Chokshi et. al. [26].	16
3.3	Young's modulus as a function of porosity for NC Pd and Cu [45].	17
3.4	Hall-Petch plot of Vickers microhardness H_v for NC Cu and Pd. The results of [26](see Fig: 3.2) are compared with those of [40]. Whereas magnitudes of the hardness values are comparable in these two investigations, the slopes are markedly different. Heat treated samples were annealed to produce grain growth.	18
3.5	Variation of hardness (left) and yield stress (right) with $1/\sqrt{d}$ for various samples reported in literature [48]. Samples produced by severe plastic deformation are above HP line while porous samples are below the expected HP line. (a, b, c, d, e, f, g, h, i, j, k, l, m, n, o, p - [48, 49, 50, 45, 35, 50, 51, 52, 53, 54, 55, 43, 56, 32, 57, 58]), respectively.	19
3.6	Yielding strength of nanocrystalline nickel [61].	20
3.7	Creep plot for a constant stress, room temperature creep test on a nanocrystalline (10nm) Pd sample [40].	21
3.8	Hardness of nanocrystalline copper (IGC) and coarse grained copper (CG) as a function of nanoindenter dwell time [65].	22
3.9	Superplastic behaviour of NC Cu sample deformed by cold rolling to elongations up to 5100% [42].	23

3.10	Room temperature strain rate sensitivity m as function of grain size for Copper. Note the steep increase in NC regime [68].	24
3.11	High resolution TEM images of the nc-Ni showing a clean atomically faceted grain boundary [22].	25
3.12	Nanoscale deformation. High-resolution transmission electron micrograph of a twin in deformed nanocrystalline aluminum [71]. This atomic resolution image illustrates the mirror symmetry between the twin and the matrix. The presence of the twin and the fact that it extends from one side of the grain to the other is unique to nanocrystalline aluminum.	27
3.13	Grain boundaries at nanoscale. $37 \times 37 \times 37 \text{nm}$ sample of Ni with mean grain size 10nm contains 4.6 million of atoms. Gray atoms sit in perfect crystalline positions, colored atoms are grain boundary atoms [76]. . .	29
3.14	Sample with $d = 20 \text{nm}$ at 14.6ps nucleated a partial dislocation $1/6[112]$. Contrary the sample with the 30nm grain size nucleated an extended $1/2[011]$ dislocation at 27.6ps . The extended dislocation consists of two partials connected by stacking fault. Applied stress is 2.3GPa in both cases [79].	30
3.15	Snapshot of NC Al structure at 11.9% strain. Variety of processes taken place. GBs are curved, a "new" grain was nucleated and a number of twins can be observed inside the grains [73].	32
4.1	Schematic illustration of a pile-up formed in grain 1 and applied resolved shear stress τ . S_2 is a source in grain 2. Dashed line would represent preferred slip planes [84].	35
4.2	Tensile Engineering Stress-Strain curves of two NC Cu samples compared with UFC Cu [60].	36
4.3	Deformation mechanism map for copper. Adapted from [38].	38
4.4	a) Mass motion of vacancies and atoms across a small grain and at a high temperature under applied stress. b) Change in shape of a grain under the mass motion shown in (a) [93]. In Coble creep mechanism mass transport is more narrowly focused to the GB region.	40
5.1	Growth of homogeneous fluctuation (a) and heterogeneous nucleation and growth (b) [96].	43
5.2	Alloy with concentration X_0 will decompose into coherent phases α_1 and α_2 without having to overcome an activation barrier. Transformation of an alloy with concentration X_0' must proceed by nucleation and growth [96].	44

5.3	Léonard and Desai showed the presence of immobile (uncooperative) dislocations influences phase separation. Both bottom and top figures represents the same time. The alloy at the bottom contains dislocations while the alloy at the top is dislocation free [98].	45
6.1	Plot of length scales and time scales accessible by common computational methods [107]. Characteristic processes for each length and time scale are in italics. Modeling techniques are in bold letters below. Dashed line highlights the modified phase field crystal (MPFC) methodology discussed in this thesis.	49
7.1	Hard sphere representation of liquid on top and solid at the bottom. Measuring the instant density in the control volume (marked dashed black) for number of time steps (right) will result in constant density profile in a liquid where atoms are constantly moving. Contrary in solids where atoms are moving only around the equilibrium position the atomic density profile will be a periodic field with periodicity of the lattice.	53
7.2	Representation of atomic configuration in a hard-sphere fluid (bottom). The pair correlation function can be obtained by choosing a particle as the origin and counting the number of atoms whose centers lie within a distance dr of a circle of radius r of the origin.	56
7.3	Direct correlation function for Cu [108].	57
7.4	Two dimensional phase diagram corresponding to the free energy in Eq. 7.19(left). Hatched areas in the figure corresponds to coexistence region. The small region enclosed by a dashed box is superimposed on the argon phase diagram on the right.	64
8.1	Simulation of heterogeneous nucleation and growth using MPFC. As time evolved several crystal seeds nucleated and grew to fill the cell. a)t=10, b)t=20, c)t=30, d)t=40. e) Plot of free energy during heterogeneous nucleation. Free energy approaches minimum with an increasing fraction of solid.	75
8.2	Left: Portion of tilted GB with $\theta = 6.4^\circ$. Right: A simple small-angle boundary formed from edge dislocations. Adapted from [113] .	76
8.3	The GB energy plotted as a function of mismatch angle. The solid line corresponds to Shockley calculations. The measurements agree with theory for small angles (left). Comparison with experimental results and PFC model (right).	77
8.4	Atoms connected by strings. Masses and spring constants are the same.	78

8.5	The displacements along a one-dimensional sample in simple uniaxial tension at three different times. Linear profiles are consistent with linear elasticity theory. Strain rate $\dot{\epsilon} = 6.5 \times 10^{-4}$	79
8.6	The displacements along a one-dimensional sample in simple uniaxial tension at three different times after a ten-fold increase in β when compared with Fig. 8.5. Non-linear profiles suggest visco-elastic behavior. Strain rate $\dot{\epsilon} = 6.5 \times 10^{-4}$	79
9.1	Phase diagram of ΔB_0 Vs. δN for the parameters $B_0^s = 1.00$, $B_1^\ell = 0$, $B_2^\ell = -1.80$, $t = 0.60$, $v = 1.00$, $w = 0.088$, $u = 4.00$, $L = 4.00$, $\gamma = 0$, $Ro = 1.00$ and $R_1 = 1.20$ (see Eq. B.4 for definitions of R_o and R_1). The solid line is a numerical solution of the one mode approximation and the dashed lines are from Eq. 9.32 for the lower solid/solid coexistence lines and Eq. 9.35 for the upper liquid/solid coexistence lines. The solid points are from numerical solutions for the minimum free energy functional given in Eq. 9.28. [114]	92
9.2	Phase diagram of ΔB_0 Vs. δN for the same parameters as those used to generate Fig. 9.1, with the exception that $w = -0.04$. The dotted lines below the eutectic temperature, $\Delta B_0^E \approx 0.028$, correspond to metastable states. [114]	93
9.3	Four stages – time steps – of rapidly solidified dendrite crystal grown from supercooled liquid with dimensionless concentration $\delta N_0 = 0.11$ and dimensionless temperature 0.05 in two dimensions. Other parameters are the same as in Fig. 9.1 except $L = 1.2$ and $R_1/R_0 = 1/4$. Frames a, b, c and d correspond to times $t = 40000$, 80000, 120000 and 160000 respectively.	98
9.4	A rapidly solidified dendrite crystal grown from supercooled liquid with dimensionless concentration $\delta N_0 = 0.11$ and dimensionless temperature 0.05 in two dimensions. Other parameters are the same as in Fig. 9.1 except $L = 1.2$ and $R_1/R_0 = 1/4$. Time corresponds to $t = 200000$. Inset: A small portion of density field n at solid-liquid interface.	98
9.5	a) Dendrite tip with highlighted line along which the microsegregation profile was plotted. b) A portion of the phase diagram Fig. 9.1. c) Micro segregation profile along the dendrite tip.	100
10.1	Left: Four level multigrid grid. Right: Density function in a multigrid representation.	103

10.2	Multigrid V-cycle. The defect equation is solved exactly on the coarsest level 1 (empty circle). On the levels 2 to 4 (full circles) only smoothing is performed by running $k - grid$ cycles using level 1 grid as an approximation. Cycle index $\gamma = 1$	104
10.3	Multigrid W-cycle. Distinction between V and W cycles is made through <i>cycle index</i> γ . See text for details.	105
10.4	Red-black distribution of grid points.	109
10.5	Bilinear interpolation used for the transfer to finer grid from the coarse grid marked by full circles. Numerics are given by the following stencils depending on the position of the calculation in the mesh. Full Circle: $I_{2h}^h \hat{v}_{2h}(x, y) = \hat{v}_{2h}(x, y)$, Box: $I_{2h}^h \hat{v}_{2h}(x, y) = 0.5[\hat{v}_{2h}(x, y+h) + \hat{v}_{2h}(x, y-h)]$, Diamond: $I_{2h}^h \hat{v}_{2h}(x, y) = 0.5[\hat{v}_{2h}(x+h, y) + \hat{v}_{2h}(x-h, y)]$, Empty Circle: $I_{2h}^h \hat{v}_{2h}(x, y) = 0.25[\hat{v}_{2h}(x+h, y+h) + \hat{v}_{2h}(x-h, y-h) + \hat{v}_{2h}(x+h, y-h) + \hat{v}_{2h}(x-h, y+h)]$	110
10.6	The convergence history of different multigrid cycles for MPFC model. V denotes a V-cycle and W a W-cycles, while the bracketed integers denote (ν_1, nu_2) described in text.	111
10.7	Complexity of successive overrelaxation (SOR) and multigrid (MG) method. Both methods are solving model Eq. 8.1 The top and bottom lines represent the theoretical complexity for the SOR and multigrid approaches, respectively. SOR and multigrid are further compared during the solidification simulation experiment where the iterative method increases the number of operations with increasing sample size by a factor of 1.3, while multigrid method increases the same by a factor of 1.1. The performance of the multigrid approach improved when simulating a deformation in a perfect crystal. In this case, the number of operations increased 1.07 times with the number of computational nodes.	113
11.1	A portion of the sample used to examine dislocation glide velocity. Parameters used: $(r, \rho_0, \Delta x, \Delta t, \alpha, \beta) = (-1, 0.49, \pi/4, 0.001, 15, 0.9)$	117
11.2	A portion of atoms in a (111) plane in face centered cubic crystal or (0001) basal plane in hcp crystal.	120
11.3	Dislocation glide velocity vs. applied strain rate.	122
11.4	Two regimes of dislocation glide. For high strain rates ($\gamma = 8 \times 10^{-5}/t$), we observed continuous glide, while at lower strain rate ($\gamma = 3.32 \times 10^{-5}/t$), the dislocation set into a stick-slip motion.	123
11.5	Distribution of stress around circular hole in an infinite plate, subjected to a uniform stress, σ	124

11.6 a) Geometry of the double U-notched sample used in the present test.	
b) Elastic stress distribution in a double notch sample measured by photoelasticity [122].	124
11.7 MPFC simulation of strain concentration in a double notched sample under a uniaxial tension. Left: A strain map of the center portion of the sample displayed at the bottom. Boundary atoms are highlighted as dark blue circles. Right: Plot represents a strain profile from the center of the sample into the root of the notch. The solid line is a guide to the eye.	126
11.8 Sample number 2 from Tab. 11.1. a) The density field $\rho(x, y)$ is plotted with highlighted angles between two couples of grains. Outline of boundary loads and loading direction is outlined by rectangles and arrows on both sides of the sample. For all simulations in this section the following parameters were used: $(\Delta x, \Delta t, \alpha, \beta, \rho_0, \tau, \dot{\epsilon}) = (\pi/4, 0.0001, 200, 0.5, 0.45, -0.6, 0.001/t)$. The same sample when only atoms with other than 6 nearest neighbors are shown, thus highlighting the imperfections in the crystals. Grain boundaries and individual dislocations are clearly outlined.	130
11.9 Deformation in the $50 \times 50\text{nm}$ sample. Average grain size is 15nm . Dislocations A, C are absorbed by surface or grain boundary respectively. Dislocation B is ejected from the GB and annihilated at the surface. Slides on Figs. 11.9, 11.10, and 11.11 correspond to simulation times $t = 30, 35$ and 40 respectively. Small arrows without labels point to a dislocation trajectory.	131
11.10 Deformation in the $50 \times 50\text{nm}$ sample. Average grain size is 15nm . Dislocations A, C are absorbed by surface or grain boundary respectively. Dislocation B is ejected from the GB and annihilated at the surface. Slides Figs. 11.9, 11.10, and 11.11 correspond to simulation times $t = 30, 35$ and 40 respectively. Small arrows without labels point to a dislocation trajectory.	132
11.11 Deformation in the $50 \times 50\text{nm}$ sample. Average grain size is 15nm . Dislocations A, C are absorbed by surface or grain boundary respectively. Dislocation B is ejected from the GB and annihilated at the surface. Slides Figs. 11.9, 11.10, and 11.11 correspond to simulation times $t = 30, 35$ and 40 respectively.	133
11.12 Two slides showing a portion of the sample with rotating grain. Initial time is $t=30$ and final time $t=40$. Dashed lines A and A' are parallel. The dotted line shows the original shape of the grain. It is superimposed onto the deformed grain on the right.	134

11.13	Three voids A, B and C are displayed in four consecutive times 25, 35, 45 and 50. Voids A and B are nucleated and continue to grow as simulation proceeds. In the second half (slides c, d) a third void C is nucleated while A and B void almost annihilate. It is also interesting to point out the dynamic nature of the process as the voids are 'gliding' along the grain boundary.	135
11.14	The effect of grain size on deformation. The average strain in the sample as function of applied strain. The curves show materials response to mechanical deformation by uniaxial tensile load. At low strains deformation is mainly elastic. Above $\approx 2\%$ of deformation plastic deformation sets in and the material starts to flow and deform plastically. Dependence of flow stress on grain size is displayed on Fig. 11.15. . .	136
11.15	Hall-Petch type plot (right) and average strain plotted against the grain size (left). Top two slides correspond yield strain and bottom slides correspond to an average flow strain in the crystal. An increase in yield strain with increasing grain size can be found up to 15nm grain size, where the curve starts to plateau. The solid lines are guides to the eye.	138
11.16	Left: Four time sequences in the evolution of the concentration field (gray scale) in a binary system with no dislocations present. superimposed on the corresponding density field. Dislocations are labeled by a square on the dislocation core surrounded by a circle. The time sequence (a)-(d) corresponds to $t = 50, 200, 600$ and 2200 . System size is: $800\Delta x \times 800\Delta x$, where $\Delta x = \pi/4$. The density difference $\delta N = 0$, while $L = 2.65$, $R_1/R_0 = 1/4$ ($R_0 = 1$) and all other parameters are the same as Fig. 9.1. Right: 2D structure factor calculated for the concentration profiles on the left.	139
11.17	Log-Log plot of the characteristic linear dimension (domain size) at time t after the quench, for the simulation shown in Fig. 11.16. Domain size is extracted from structure factor (Fig. 11.16e.)	141
11.18	A dislocation migrates toward a coherent phase boundary, thus relaxing mismatch strain. An 800×800 (units of Δx) portion of the actual simulation domain is shown. The data shows four time frames in the motion of the dislocation. Parameters of the simulation are the same as in Fig. 11.16, except the misfit between the lattice parameters, which was increased to 0.5.	142
11.19	Four time sequences in the evolution of the concentration field (gray scale), superimposed on the corresponding density field. Dislocations are labeled by a square on the dislocation core surrounded by a circle. The time sequence (a)-(d) corresponds to $t = 100, 200, 800$ and 2500 , respectively. The system size is: $1024\Delta x \times 1024\Delta x$, where $\Delta x = \pi/4$.	143

11.20	The solid line represents a time dependence of inverse of the mean wave vector of the (circularly averaged) 2D structure factor of the concentration field corresponding to the simulation in Fig. 11.19. The dashed line is a guide to the eye at a slope $t^{1/3}$. Growth regimes are outlined by dash-dotted vertical lines. Regime A is an initial growth with kinetics unaltered by dislocations. In regime B domains experience drag from the dislocations and slow down in growth rate. Regimes C, D are expanded in Fig.11.21.	144
11.21	The domain growth rate at late times for simulation displayed in Fig. 11.19. The dashed lines are guides to the eye at a slope $t^{1/3}$. Growth regimes are outlined by dash-dotted vertical lines. Regimes C is an accelerated regime, D corresponds to asymptotical regime. . . .	145
12.1	A single crystal growth with BCC and FCC structures simulated by Eq. 12.2. Coordination numbers of crystalline structures indicate a coordination number 8 in BCC and a coordination number 12 in FCC structure.	148

Chapter 1

Introduction

One of the very basic results of materials research is the notion that most properties of solids depend on the underlying microstructure. Understanding microstructure evolution and interactions of microstructure with defects enables us to predict the materials behaviour in practical applications. For example, in polycrystalline metals – the primary focus of the thesis – mechanical properties are influenced by the size of the crystallites, or grains [1]. Another example is an interaction of dislocation with second-phase particles or interactions between dislocations.

Over the years, numerous experimental and theoretical studies were devoted to study strengthening mechanisms in solids. For example, in the mid 1950's two researchers independently showed that as grain size decreases, the strength of materials will increase. This behaviour was attributed to the interaction of line defects, or dislocations, with grain boundaries and became commonly known as the Hall-Petch effect (HPE). As progress in materials processing technologies was made, it became possible to synthesize materials with a grain size in the order of nanometers, where little or no dislocations are present. While HPE proved to be very reliable to predict strength in materials where grains are tens to hundreds of micrometers in size, materials with grain size of a few nanometers pose a challenge to the validity of the HPE. These materials were first considered by Gleiter [2], who named them *nanocrystalline materials* and defined them as microstructurally heterogeneous materials consisting of nanometer-sized crystallites and grain boundaries (GBs). The synthesis, characterization, and processing of nanocrystalline materials are part of a rapidly growing field referred to as *nanotechnology*.

Progress in materials processing and synthesis was followed by advances in

microscopy, X-ray diffraction, and mechanical, and numerical testing. New tools capable of characterizing materials with force, displacement, and spatial resolution as small as picoNewton ($\text{pN} = 10^{-12} \text{ N}$), nanometer ($\text{nm} = 10^{-9} \text{ m}$), and Angstrom ($\text{\AA} = 10^{-10} \text{ m}$) became available. Increasing computer power as well as new numerical techniques allowed the study of bigger samples in more detail, often employing hundreds of computers in parallel. These experimental and computational techniques allowed significant progress in our understanding of the structure and mechanics of nanocrystalline metals. On the other hand, in spite of the increasing computer power, the atomistic computer simulations, often used to simulate processes in nanocrystalline materials, are usually confined to limited sample sizes and very short times. As a result of these limitations, less progress has been made on generalizing the results of atomic-scale simulations from nanocrystalline metals to more coarse grained metals and longer time scales. Direct extrapolations might be misleading, as new processes become active upon increase in grain size from the nanoscale length scale or as processes become diffusional.

In this thesis, we present a new modeling formalism that is able to describe processes on nanometer length scales and microscopic time scales (e.g. dislocation glide), together with processes observed over longer periods of time and distance (e.g. grain growth, dislocation climb), defined by diffusion time and length. Having a model with such properties is very useful, as we will be able to describe processes that occur in the nanoscale regime without being limited to the short time scales of molecular dynamics. A good example of such a process is the break down of the HPE [3, 4, 5] as nanoscale grain sizes are approached or non-equilibrium microstructure formation such as spinodal decomposition and solidification of pure or binary systems.

The study of non-equilibrium microstructure formation has seen considerable advances through the use of the *phase field* approach [6][7]. This methodology models the dynamics of various continuum fields that collectively characterize microstructure in phase transformations. In these phenomena, the evolution of the appropriate field(s) (e.g., solute concentration in spinodal decomposition) is assumed to be dissipative and driven by the minimization of a phenomenological free energy functional [7].

Advances in the phase field modeling of solidification phenomena have followed a progression of innovations, beginning with the development of free energies that cap-

ture the thermodynamics of pure materials [8] and alloys [6]. Several modifications were then proposed to simplify numerical simulations and improve computational efficiency. Perhaps the most important innovation was the development of matched asymptotic analysis techniques that directly connect phase field model parameters with the classical Stefan (or sharp-interface) models of pure materials or alloys [9]. These techniques were complimented by new adaptive mesh refinement algorithms [10], whose improved efficiency significantly increased the length scales accessible through numerical simulations, thus enabling the first experimentally relevant simulations of complex dendritic structures and their interactions in organic and metallic alloys [11].

A weakness of the traditional phase field methodology is that it is usually formulated in terms of fields that are spatially uniform in equilibrium. This eliminates many physical features that arise due to the periodic nature of crystalline phases, including elastic and plastic deformation, anisotropy, and multiple orientations. To circumvent this problem, traditional phase field models have been augmented by the addition of one or more auxiliary fields used to describe the density of dislocation continuum stress, strain fields, and orientation fields [12, 13, 14]. Nevertheless, it has proven quite challenging to incorporate elasto-plasticity, diffusive phase transformation kinetics, and anisotropic surface energy effects into a single, thermodynamically consistent model.

Very recently, a new extension of phase field modeling has emerged and become known as the *phase field crystal* method (PFC) [15, 16, 17]. This methodology describes the evolution of the atomic density of a system according to dissipative dynamics that are driven by free energy minimization. In the PFC approach, the free energy functional of a solid phase is minimized when the density field is periodic. The periodic nature of the density field naturally gives rise to elastic effects, multiple crystal orientations, and the nucleation and motion of dislocations. While these physical features are included in other atomistic approaches (such as molecular dynamics), a significant advantage of the PFC method is that, by construction, it is restricted to operate on diffusive time scales as opposed to the prohibitively small time scales associated with atomic lattice vibrations. In the case of pure materials, the PFC approach has been shown [15, 16] to model many phenomena dominated by atomic scale elastic and plastic deformation effects. These include grain boundary

interactions, epitaxial growth, and the yield strength of nano-crystals.

The original PFC model is among the simplest mathematical descriptions that can self-consistently combine the physics of atomic-scale elasto-plasticity with the diffusive dynamics of both phase transformations and microstructure formation. Similar to traditional phase field modeling of solidification, however further work is required to fully exploit the methodology. More specifically, it is important to be able to generalize the method to more complex situations (binary alloys, faster dynamics, different crystal structures, etc.), so as to develop more efficient numerical techniques and make a direct connection of the parameters of the model to experimental systems. Several innovations toward this goal have already been made. Goldenfeld *et al.* [18] have recently derived amplitude equations for the PFC model that are amenable to adaptive mesh refinement schemes. This work has the potential to enable simulations of mesoscopic phenomena ($\mu m \rightarrow mm$) that are resolved down to the atomic scale and incorporate all the physics discussed above.

In this thesis, we introduce two new contribution to PFC technique:

- The first is the inclusion of higher order time derivatives in the dynamics so as, to simulate “instantaneous” elastic relaxation [19]. This extension is important for modeling complex stress propagation and externally imposed strains. Taking full advantage of this improvement, we study HPE in nanocrystalline materials.
- The second is linking the PFC method to the formalism of the classical density functional theory (DFT) of freezing as formulated by Ramakrishnan and Yussouff [20]. The PFC method is then used to develop a model for binary alloys.

The thesis is divided into three main parts. In **Part I** we review current literature relevant to the topic of nanocrystalline metallic materials. We begin our discussion in chapter 2 with the classification and processing methods of nanocrystalline materials. Classification is followed by a review of the processing techniques of nanocrystalline materials. Then we review mechanical properties of polycrystalline materials as observed in experiments and in computational simulations. Chapter 4 of the thesis summarize deformation modes in polycrystalline materials. Chapter 5 introduces the topic of spinodal decomposition in binary alloys. In particular, we

focus on the interplay between growing compositional domains, dislocations, and the effect on of dislocations strengthening in binary alloys.

In **Part II**, the phase field crystal modeling (PFC) technique is reviewed. We begin in chapter 7.2 with an outline of basic terms used in the classical density functional theory of freezing. In the PFC approach, the free energy functional is written in terms of the time averaged atomic density field, ρ , (ρ_A and ρ_B in binary systems) and expanded around a liquid reference state that exists along the liquid/solid co-existence line. Formally, the expansion contains the n-point correlation functions of the liquid state. In this work, the series expansion of the free energy is truncated at the 2-point correlation function, $C(\vec{r}_1, \vec{r}_2)$ ¹. Within this framework, the derivation of a phase diagram for pure material is shown in section 7.3.

In chapter 8, we introduce our first main contribution; a modified phase field crystal model (MPFC). The MPFC model includes diffusive dynamics and elastic interactions. This inclusion is achieved by exploiting the separation of time scales that exist between diffusive dynamics and elastic relaxation processes in solids. In particular, the MPFC model is constructed to transmit long wavelength density fluctuations with wave modes that propagate up to a time scale t_w , after which the strain-relaxed density field continues to evolve according to diffusive dynamics. The key feature of our approach is that the value of t_w can be chosen to be much smaller than the characteristic time scale of diffusion, and much longer than $1/\omega_D \approx 10^{-13}s$, where ω_D denotes the Debye frequency. The MPFC model has the ability to simulate atomic-scale interactions and dynamics on time scales that are many orders of magnitude longer than those of molecular dynamics. Most importantly, our modified model naturally incorporates instantaneous elastic interactions. In section 8.1, we study the propagation of elastic perturbations in a linearized version of the MPFC by way of Floquet stability analysis. The analysis shows how the two time scale are separated and how they relate to varying sample size. Next, we compare our model to the one derived by Majaniemi et. al. [21] from more fundamental principles. The analysis shows that our original modified phase field crystal (MPFC) model follows the correct approach to elastic relaxation. To illustrate the essential properties of MPFC model, we applied the model to solidification, grain growth, grain boundary energy study,

¹The two-point correlation function, roughly speaking, represents a time-averaged of the two-particle interaction potential of molecular dynamics.

and deformation in elastic bars. These four test cases show that the model correctly reproduces processes on both diffusive and instantaneous time scales. Moreover, the final example shows a correct distribution of strains in a one dimensional sample.

In chapter 9, our second main contribution is considered, a PFC model for binary system. Similar to the case of pure material, the free energy expansion of a binary alloy will be truncated at the 2-point correlation functions for each atomic species, which are then characterized by three parameters. It is shown that the “regular” solution model used in materials physics for alloys can be obtained directly from DFT. This chapter also provides insight into the concentration dependence of various properties of the crystalline phase of a binary alloy, such as the lattice constant, effective mobilities, and elastic constants.

In the rest of the chapter 9, a simplified version of the binary alloy free energy is derived. This is done in order to provide a mathematically simpler model that can more transparently illustrate the use of PFC formalism while simultaneously modeling diverse processes such as solidification, grain growth, defect nucleation, phase segregation, and elastic as well as plastic deformation. This chapter also shows that the free energy of the simplified alloy PFC model reproduces two common phase diagrams associated with typical binary alloys in materials science. Some of the more tedious calculations in the derivation of the simplified model are shown in Appendix B. In section 9.6, the dynamical equations of motion that govern the evolution of the solute concentration and density field of the binary alloy are derived. Finally, the simplified binary alloy model is used to demonstrate the phase transformation kinetics associated with solidification.

The solution of the partial differential equation of motion poses a challenge to computational resources, in particular when large samples are studied. To circumvent this issue, we developed a semi-implicit multigrid solver described in chapter 10.

In the **Part III** of the thesis, we apply the single component and binary MPFC model to study a set of problems that are currently of interest in the scientific community. To calibrate the model and to verify essential deformation processes, we measure the velocities of individual dislocations and strain distribution in a single crystal. Exploiting a unique combination of accessible length scales and time scales of the MPFC model, we simulated grain size dependence in the deformation of NC materials. By increasing the grain size from a few nanometers to approximately 30

nanometers, we observe changes in microstructure and strength while applying a load. Simulation results are then compared to experimental results.

The third part of the thesis continues with a study of spinodal decomposition in binary alloys. First we examine the basic kinetics of spinodal decomposition in a perfect crystal, then the growth rate of compositional domains is measured and compared to growth rate observed when dislocations are present in the microstructure. Simulation results are again compared to previously published data and discussed.

Finally, we present an extension of the PFC technique to three dimensions by using a direct two point correlation function for copper.

Part I

Literature Review and Main Issues

Chapter 2

Processing and Characterization of Nanostructured Metals and Alloys

2.1 Categorization of Nanostructured Materials

Since the emergence of materials with a microstructure modified on the atomic level various structures has been synthesized. In the semiconductor industry we can find materials with reduced dimensions in the form of nanometer-sized particles, thin wires or films. Another group of materials is represented by materials with reduced size microstructure localized to layers only a few nanometers in thickness. Such coatings are used to improve corrosion resistance, hardness and wear resistance. The last group of materials with nanometer sized microstructure includes bulk solids. This thesis will focus on a microstructurally heterogenous materials consisting of crystallites (grains) with various orientations separated by grain boundaries [2].

Materials with a nanometer-sized (typically 1–100nm) microstructure are called *Nanostructured materials* (NsM) or synonymously – *Nanocrystalline* (NC) materials. These two terms are typically used interchangeably. Metals and alloys with average grain size levels in the 100 – 1000nm range are defined as ultrafine crystalline (UFC) metals and alloys. Their microcrystalline (MC) counterparts have an average grain dimension of a micrometer or larger. The synthesis, characterization and processing are part of a rapidly growing field referred to as *nanotechnology* [22].

2.2 Processing Techniques

Nanocrystalline materials are prepared by either breaking down bulk pieces of materials into nanosized particles or an atomistic assembly process. The first group is called top-down and the latter bottom up.

The oldest method to produce nanocrystalline samples is the *inert gas condensation* (IGC) technique [23]. A material is evaporated in a high purity atmosphere of He (0.1–1 kPa pressure) contained in a pre-baked ultra high vacuum evaporator. Thermal energy of evaporated metal atoms is transferred to He molecules. Subsequently evaporated metal condenses in the form of nanometer sized crystals, which accumulate at the surface of a cold finger. After restoring ultra high vacuum conditions, the crystals are scraped off the cold finger and are consolidated, using hydrostatic pressure of 5GPa, into a dense polycrystalline material. The size of the crystals depends on the pressure and the evaporation rate. IGC has certain limitations, including specimen volume, sample porosity and costly equipment. Calls for reduction in processing defects, such as impurities and porosity, lead to the development of new and improved technologies. State-of-the-art IGC technologies produce cleaner powders improved densities, ranging from 70% – which was common value in early days of NsM – to 98% of fully dense value [24, 25]. Various metals have been successfully processed using IGC method e.g. Cu, Pd [26, 27].

Another common method for a preparation of NC metals and alloys is the *electrodeposition* (ED) by means of pulse electrolysis. A soluble anode of deposited metal and insoluble cathode are placed in the electroplating bath. After the deposition the final product can be scraped of the cathode. Advantages of this method are its relative simplicity and low cost as well as its ability to form nanostructure deposits in various shapes and sizes. Using process parameters such as bath temperature and composition and current density, the modulation grain size of NC material can be tuned to values between 10–100nm. Electrodeposited samples have virtually no porosity and do not require a consolidation step. NC Ni, Co, Pd, Cu and their alloys, such as Ni-W, Ni-Cu, Ni-P and Ni-Fe, have been successfully prepared by the ED method [28, 29, 30]. Coatings of NC Ni have been successfully applied in the industry to repair tubing in nuclear power plants, improving mechanical properties and thermal stability [31]. *Crystallization from amorphous alloys* is a method with a higher yield of

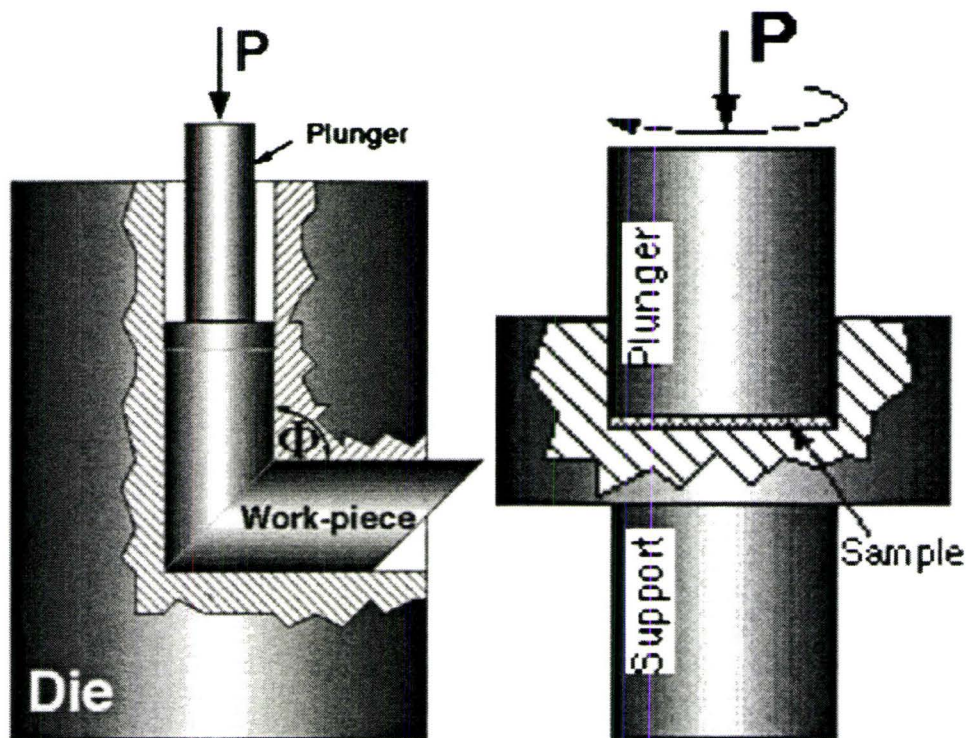


Figure 2.1: Severe plastic deformation method. **Left:** Equal-channel angular pressing setup. **Right:** High-pressure torsion setup [32].

NC material than IGC. The basic idea of the method is that, that during annealing of an amorphous alloy the crystallization will occur, which involves the formation of clusters and the nucleation and growth of nanocrystallites. An amorphous alloy usually takes the form of a ribbon, stripes or a powder and is prepared by a number of rapid quenching methods. Bulk NC alloy specimens can be made by cold compaction after crystallization. This method is limited to alloys that can be transformed into a glassy state and produces porous free samples (e.g. NiP) [33, 34].

Strength of metals after plastic deformation usually increases while its ductility decreases. However, it was shown that nanocrystalline materials prepared by a top-down method of *severe plastic deformation* (SPD) possess an extraordinary combination of strength and ductility. During SPD, bulk material is deformed by large shear strain under high pressure while the work-piece dimensions remain unchanged. Two of the most widespread methods are equal channel angular pressing (ECAP) and high pressure torsion (HPT) [35] [32]. In ECAP, a material is pressed a number of times through the same die (Fig. 2.1left). In HPT, a rotating plunger imposes large shear strains onto a sample (Fig. 2.1right). Samples are usually disks sized $20 \times 1\text{mm}$ that contain high dislocation densities and high internal elastic strains.

The last method of NsM preparation, mentioned later in our text, is the top-down, solid-state processing method of mechanical attrition and mechanical alloying known as *ball milling*. In this process, lattice defects are produced within the initially single-crystalline powder particles. The internal refining process results from the creation and self-organization of dislocation cell networks and the subsequent formation of small and high-angle GBs during the mechanical deformation process. A broad range of chemical compositions and atomic structures can be synthesized using this method. Limiting factors include the porosity and a possible contamination of powder particles by milling tools and the surrounding atmosphere [36].

2.3 Characterization of NC Materials

As mentioned in the previous section, most of the methods used to prepare NsM introduce various flaws (pores, microcracks) into the material. Before valid comparisons can be made between empirical measurements of the mechanical properties of NC metals and the model predictions, it is necessary to ensure that experimental

NsM data represents the inherent behavior of the material and are not compromised by sample imperfections. Indeed, as will be seen from the following literature review, there is a plethora of often contradictory data in NsM, which can make a unified characterization of NsM properties difficult [37, 38, 25].

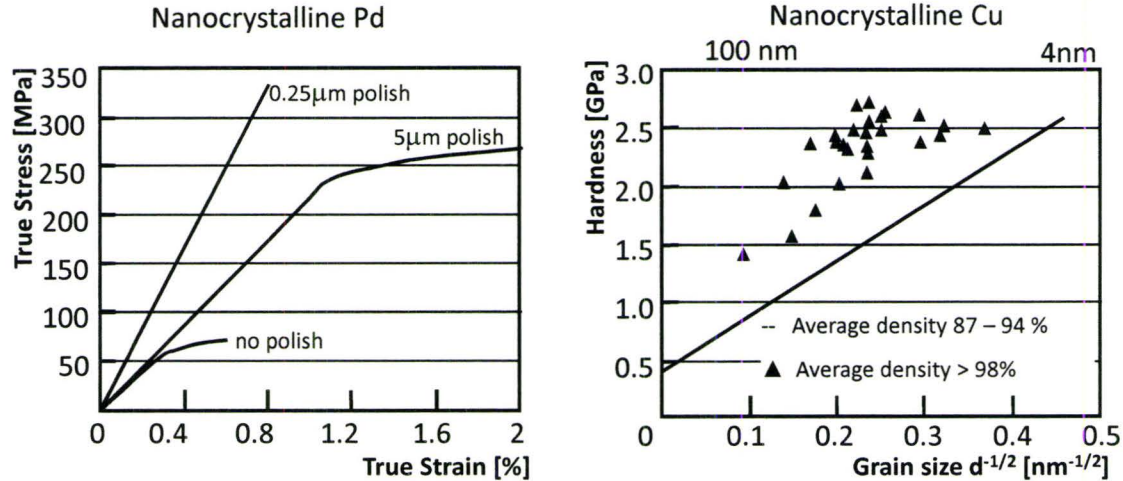


Figure 2.2: **Left:** Stress-Strain results of tensile tests on NC powder. Beneficial effects of polishing. Surface flaws were related through Griffith criteria to a critical surface crack with a magnitude of about $2\mu\text{m}$ frequently observed in 'as compacted' NsM. **Right:** Influence of porosity on the Vickers hardness. Straight line: best 'fit' to the data for samples with average density 87-94%; Data points: sample with average density above 98%. Figures adapted from: [25, 39, 40].

2.3.1 Density

After examining initial measurements of the mechanical properties of NC metals produced by the IGC method [26, 34], Nieman et.al [40] pointed out that strength of tested NC samples could be limited by processing flaws (such as porosity and surface flaws) rather than by the intrinsic behavior of the material. As a result of these findings, several improvements to the production methods have been made, and several methods of studying porosity in NC material have been developed. The basic method for measuring sample density remains based on the Archimedes principle, where samples are first weighed in the air and then submerged into liquid. Later,

small angle neutron scattering was employed to recognize pores in the range of 1–100nm [41]. All of the above mentioned methods can be coupled with optical, SEM, and TEM observations, which describe the more qualitative characteristics of the present pores. The profound influence of sample quality on the Vickers hardness and stress-strain results are displayed on Fig. 2.2.

2.3.2 Determination of Grain Size

When plotting Hall-Petch plot the grain size determination becomes an important factor. Errors in grain size determination can shift the curve to higher or lower values, making it difficult to accurately pinpoint the grain size at which a transition to different deformation behavior will occur.

Transmission electron microscopy has been used to observe the shape of the grains [26, 34, 42] the twins [43], the character of grain boundaries (Fig. 3.13), and to determine the size distribution. The drawbacks of this method are that only a small number of grains is included in the observation, the lengthy sample preparation, and destructive nature of the sample preparation [40].

Another approach to the determination of grain size is the non-destructive technique of X-ray diffraction (XRD). The advantage of XRD is that a large number of grains are included in the grain size estimation. While the position of the peaks in an XRD profile determines the phase, grain size is a function of the width of the peak. Width is measured at a half maximum peak intensity. One commonly used XRD method is the Scherrer method [34, 40] which calculates grain size as $D = \lambda/w_f \cos\theta$, where w_f is the width at half-maximum intensity, λ is the wavelength of the X-ray radiation, D is the average crystallite size and θ is the Bragg angle [44]. The Scherrer method is not sufficient when lattice strains are present in the sample, which is common if the sample is prepared by severe plastic deformation (see section 2.2). Lattice strains have a similar widening effect on the peak as the grain size. To separate the effect of lattice strains and determine the correct grain size, the shape of the peak is analyzed by Fourier analysis. The Stokes-Wilson method and Warren-Averbach method both incorporate this approach [44, 40].

Chapter 3

Mechanical Properties of Nanostructured Metals and Alloys

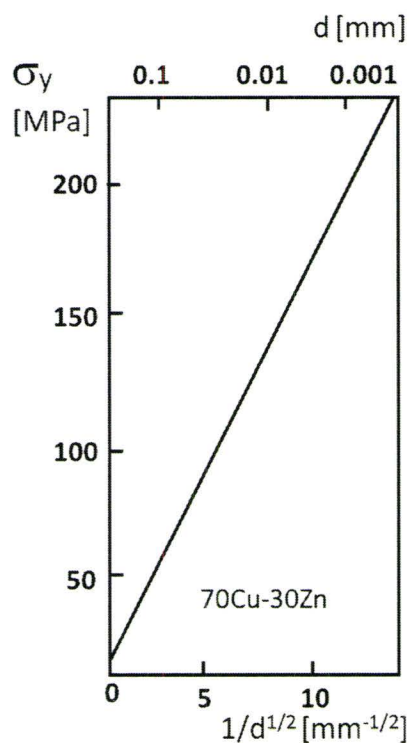


Figure 3.1: Hall-Petch plot for Cu alloy [1].

The successful application of nanocrystalline metals as structural materials in industrial applications requires a detailed knowledge of mechanical properties and understanding of deformation behavior. This chapter reviews the elastic and plastic mechanical properties of NsM, with an emphasis on grain structure, defects and sample preparation.

Most engineering materials are composed of tiny crystallites - called grains. It is a well known fact that mechanical properties of materials crucially depend on the grain size. In the mid 50's of the last century, Hall and Petch showed that, for low carbon steels with grain sizes in the mi-

rometer range, the yield strength is inversely proportional to the square root of the average grain size (Fig. 3.1) [3, 4]. The question now posed on this relationship is how far the strength of a material may be increased by refining its grain size. In early 90's, experiments on copper, palladium, and NiP alloy [26, 34] specimens showed behaviour opposite – or the 'reverse' – of what was predicted by the Hall-Petch relationship. These studies found decreasing hardness of a polycrystalline material with decreasing grain size (Fig. 3.2). From then forward, experimental studies of mechanical properties of nanocrystalline metals have concentrated on the grain size dependence of strength, usually determined by hardness measurements.

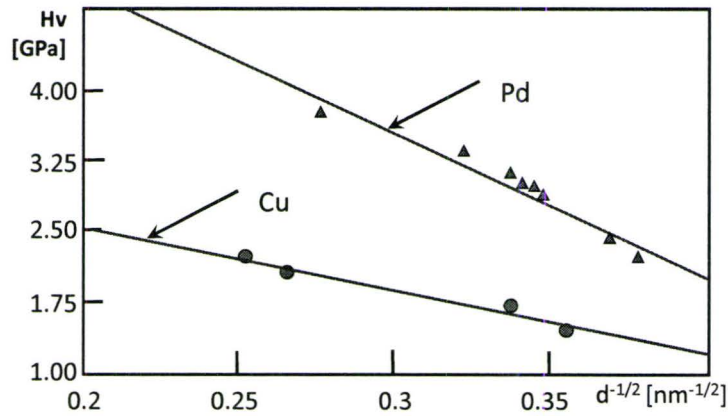


Figure 3.2: Variation in hardness with $d^{-1/2}$ for NC Cu and Pd reported for the first time by Chokshi et. al. [26].

3.1 Mechanical Testing

3.1.1 Elastic Properties

Initial measurements of elastic properties estimated the Young's modulus of the NC metals to be significantly lower than measured on conventional materials [40]. It was suggested and later confirmed, that these low modulus measurements were caused by porosity, which is typically present in NC materials produced by IGC. Later experiments showed the Young's modulus to be slightly lower than the reference value.

Modulus appears to decrease exponentially with increasing porosity. Typical values for Young’s modulus of Cu and Pd are depicted in Fig. 3.3, where curves extrapolated to 0% porosity intercept the modulus axis with values very close to those of bulk samples with large grain sizes: $E_{Cu(coarse)}=128\text{GPa}$ and $E_{Pd(coarse)}=133\text{GPa}$ [45].

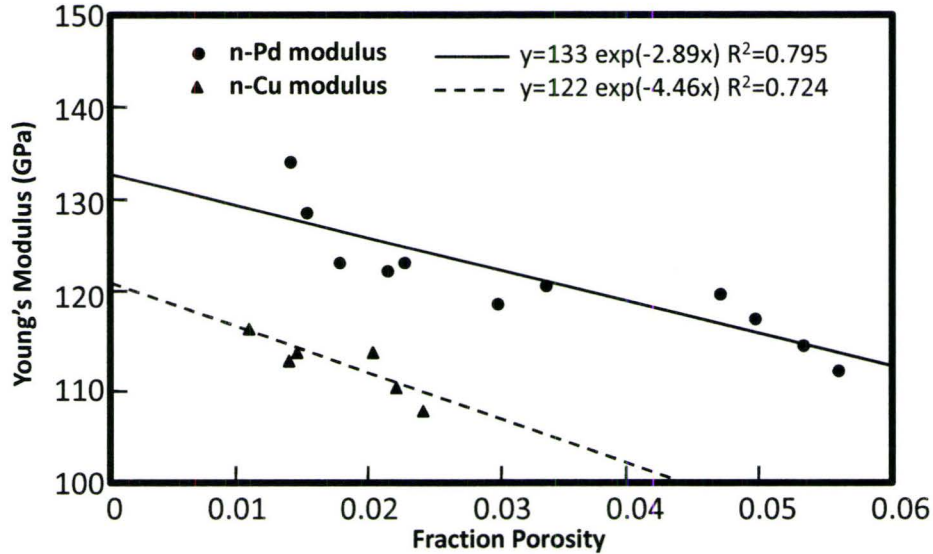


Figure 3.3: Young’s modulus as a function of porosity for NC Pd and Cu [45].

3.1.2 Grain Size Dependence of Strength

Microhardness

Because of the small size of most NC samples, studies of strength are usually confined to hardness measurements. Chokshi, Rosen, Karch and Gleiter were the first to report on the variation in the hardness with grain size for NC materials. In contrast to the Hall-Petch relationship (HPR) their results showed a decrease in hardness with a decrease as grain size decreased from 20 to 5 nm for NC copper and palladium produced by IGC [26]. Deviations from the HPR were also observed in studies on NC samples of Ni-P alloy with average grain sizes less than 37nm [34], NC nickel with average grain sizes less than 20nm [46] and Al-1.5%Mg alloy [47]. Later measurements suggested opposite behaviour (Fig. 3.4 after [40]). Initially, the

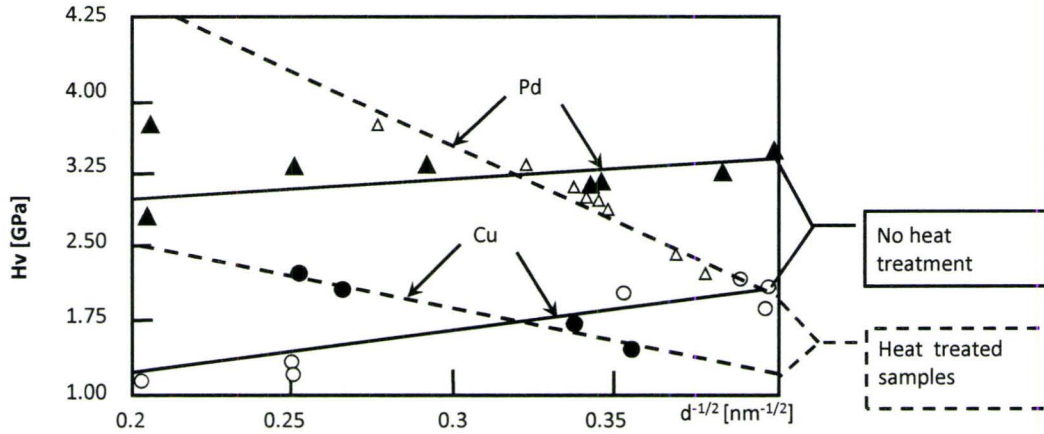


Figure 3.4: Hall-Petch plot of Vickers microhardness H_v for NC Cu and Pd. The results of [26](see Fig: 3.2) are compared with those of [40]. Whereas magnitudes of the hardness values are comparable in these two investigations, the slopes are markedly different. Heat treated samples were annealed to produce grain growth.

discrepancy was partly explained by sample porosity of and the observation that hardening and softening of NC metals can depend upon the method used to vary the grain sizes. For example annealing a sample to produce grain growth can result in hardness values greater than those as-prepared samples with similar grain sizes [27]. It is also worth mentioning that, when drawing results between microhardness H_v and grain size $d^{-1/2}$, one should consider error not only for H_v but also account for consider 10–50% uncertainty in the measured grain size.

More recent measurements on copper confirmed the validity of grain size strengthening down to 10 nm [48] while achieving compressive strength up to 3GPa. Besides the high strength, summary plot Fig. 3.5 points out that variation in production methods can have a strong influence on nanocrystalline materials properties. Points above the expected HP line are prepared by SPD method with a high dislocation density while porosity was attributed to samples with hardness below the HP line.

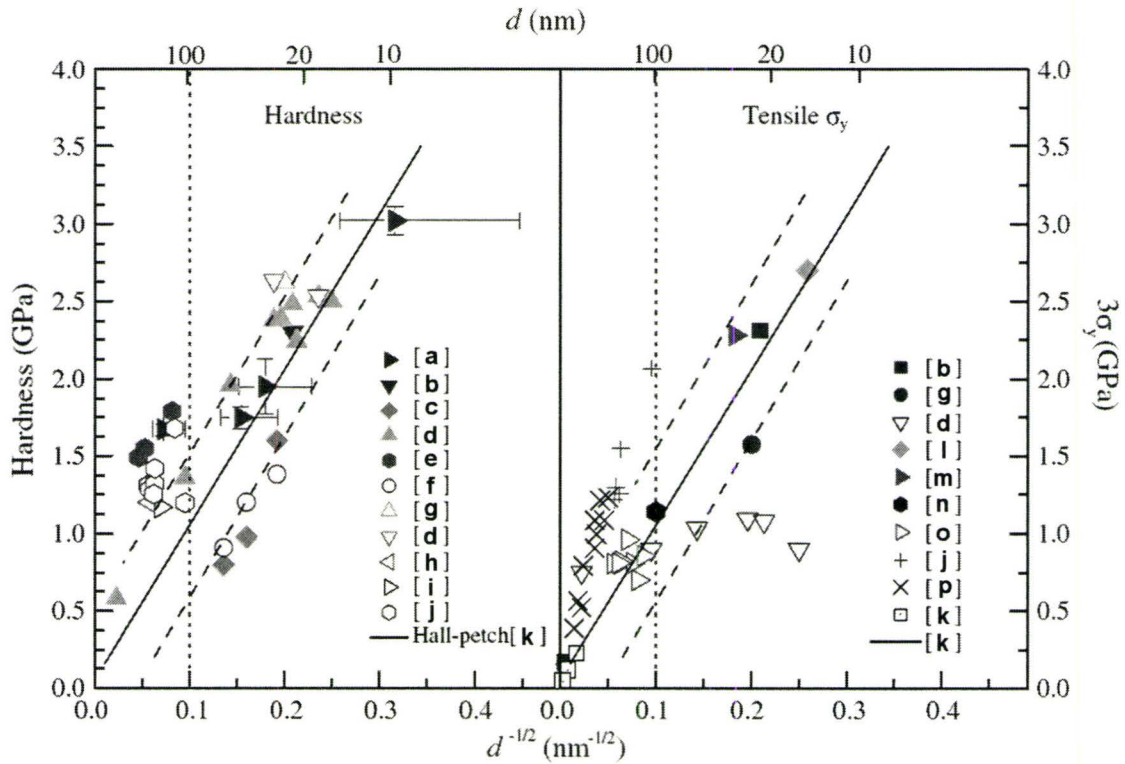


Figure 3.5: Variation of hardness (left) and yield stress (right) with $1/\sqrt{d}$ for various samples reported in literature [48]. Samples produced by severe plastic deformation are above HP line while porous samples are below the expected HP line. (a, b, c, d, e, f, g, h, i, j, k, l, m, n, o, p - [48, 49, 50, 45, 35, 50, 51, 52, 53, 54, 55, 43, 56, 32, 57, 58]), respectively.

Tensile and Yield Strength

Early measurements on the NC palladium reported that for samples with average grain sizes of 25nm, the yield stress was 185MPa, values twice as large as reported for coarse grained samples (e.g. 50 μ m [40]). The tensile data again showed an apparent flaw sensitivity [59]. A lower density of the NC sample or a few large grains in the NC sample can cause a decrease in the yield strength by a factor of two. Measurements on samples with improved porosity showed the yield strength to be 10–15 times those in the coarse-grained, annealed metal [45]. For a NC sample of copper with an average grain size of 30nm, the yield strength was measured as high

as 760MPa [60] or even 1GPa with twin boundary refinement [43]. These and similar results from other studies suggest that grain refinement leads to a large increase in the yield strength. This gain is at the expense of ductility though, as shown for NC copper and palladium [39, 61]. Tensile tests on NC nickel showed that the Hall-Petch slope becomes negative for grain sizes below 10nm (see Fig.3.6). Typical strain rates during tensile tests were in the range of $10^{-5}s^{-1}$ to $10^{-3}s^{-1}$.

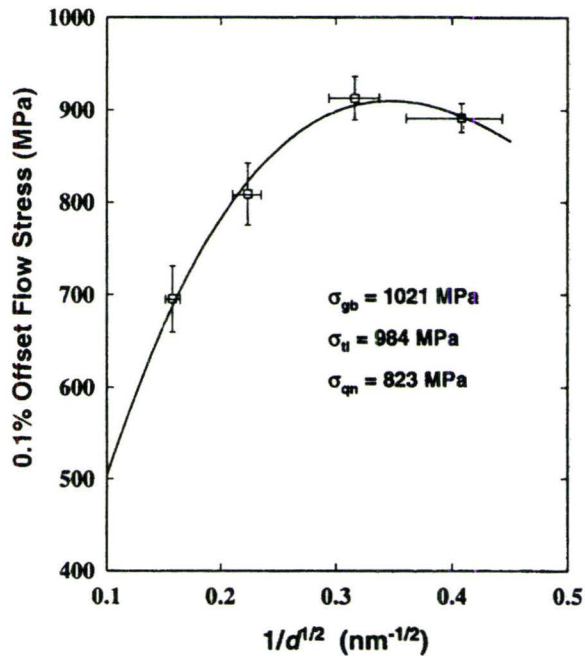


Figure 3.6: Yielding strength of nanocrystalline nickel [61].

Creep

It was predicted [23] that traditional dislocation mechanisms cease to operate in nanocrystalline materials while diffusional creep mechanisms are enhanced due to reduction of grain size.

Creep tests on NC palladium and copper produced by IGC initially did not show a significant room temperature creep rate under loads much larger than the yield stress of coarse-grained samples [59, 40]. Measurements on NC nickel showed that a creep mechanism can be significant only at high stress levels and that the average

grain size of NC sample must be below 10nm. Later measurements [62, 42] showed

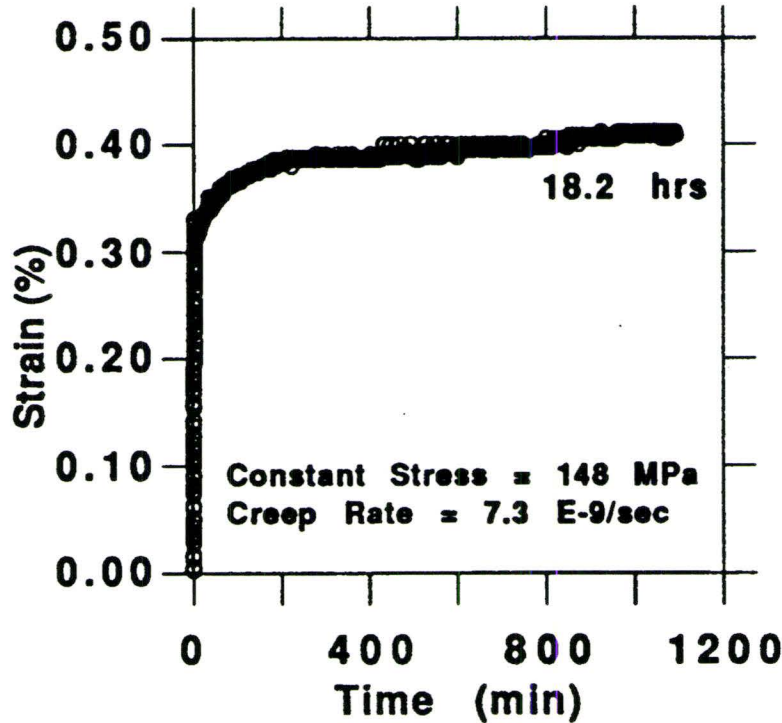


Figure 3.7: Creep plot for a constant stress, room temperature creep test on a nanocrystalline (10nm) Pd sample [40].

the presence of creep strain rates on the same order to be consistent with the Coble Creep mechanism [63]. These experiments were carried out at room temperature to prevent grain growth. It was shown that strain rates are lowered below values expected by Coble creep when grains are allowed to grow during the test or vacancies are generated due to consumption of grain boundaries [64]. Microhardness creep measurements (Fig. 3.8) on NC Cu [65] and Al [66] showed a decrease in hardness with increasing dwell time as well as rapid grain growth.

Flaws, Ductility and Strain Rate Sensitivity

Earlier NC samples were prone to low ductility and fracture due to presence of flaws (Fig. 2.2). In 2000, Lu [42] synthesized high purity Cu samples without

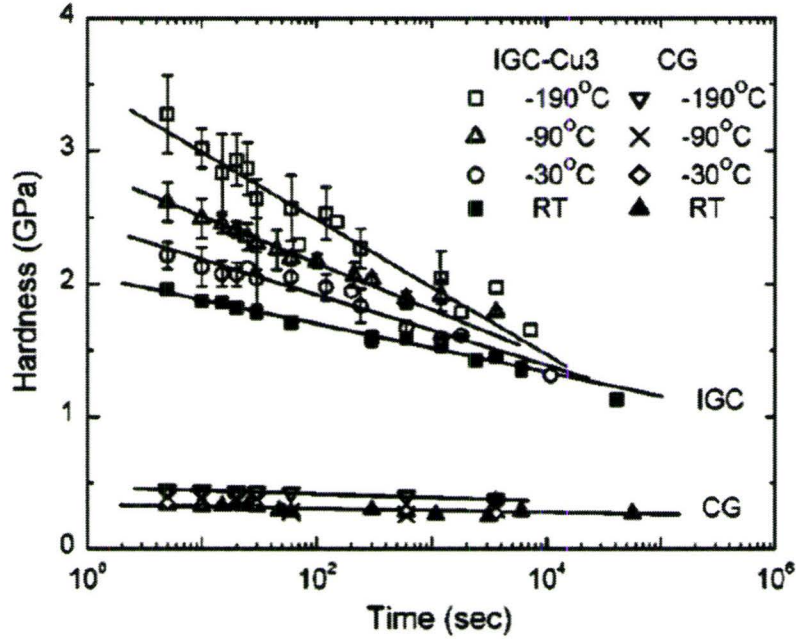


Figure 3.8: Hardness of nanocrystalline copper (IGC) and coarse grained copper (CG) as a function of nanoindenter dwell time [65].

significant porosity and was able to obtain elongation of 5000% as shown on Fig. 3.9. After repeated cold rolling, the initial sample measuring $16 \times 4 \times 1 \text{ mm}$ became a long ribbon approximately $20 \mu\text{m}$ thick with no surface cracks. Typical copper samples break at approximately 800% extension.

Similarly, NC Cu samples without flaws reported 11 times higher tensile strength than conventional coarse-grained copper, while retaining a 14% uniform tensile elongation [67]. The limiting factor to high ductility was thickness of the samples, as thin samples were failing prematurely due to increased sensitivity to surface cracks.

Early studies on NC materials [61] further emphasized the strain-rate sensitivity of NC materials. It has been shown that for the same material, the yield strength varies with the loading rate (i.e. a higher loading rate may give rise to a higher yield strength).

Strain rate sensitivity of the flow stress is represented as $\sigma_T = K\dot{\epsilon}_T^m$, where $\dot{\epsilon}_T$ is true strain rate, m is the strain rate sensitivity, and K is a constant. The maximum strain sensitivity is 1 as the stress increases linearly with strain rate – a viscous

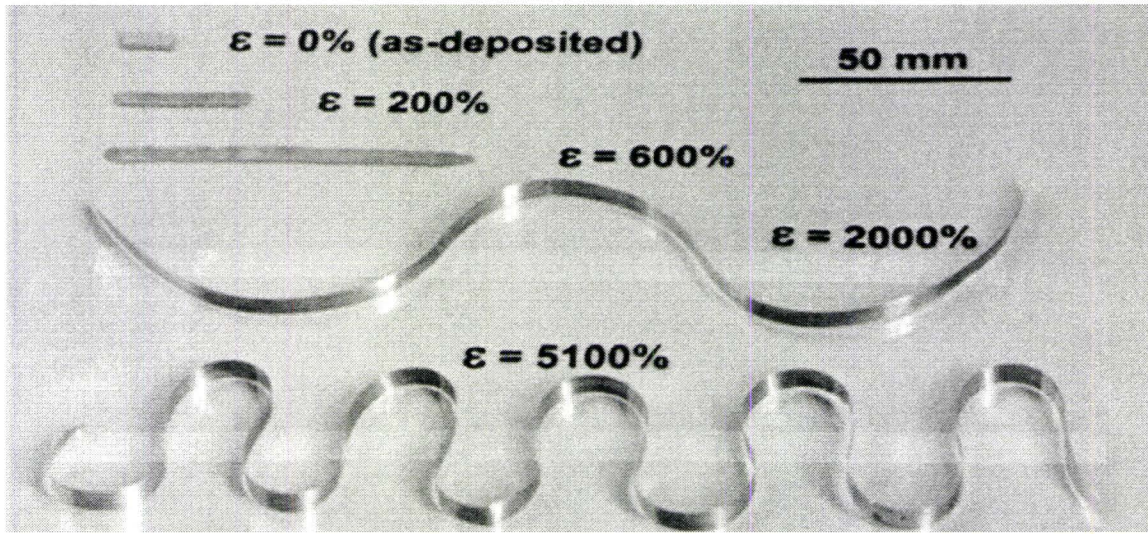


Figure 3.9: Superplastic behaviour of NC Cu sample deformed by cold rolling to elongations up to 5100% [42].

solid. High values of m indicate resistance to necking and renders these materials superplastic. As displayed on Fig. 3.10, strain-rate sensitivity for nanocrystalline materials increases by about an order in magnitude when grain size is reduced to nanocrystalline size. It is expected that NC material possess superplastic properties.

3.1.3 X-ray Diffraction and Microscopic Studies

Microscopy and X-ray analysis has been used to determine the grain size distribution as mentioned in section 2.3.2, providing another tool with which to understand the mechanical behavior of NC materials.

X-ray Diffraction

In section 2.3.2, we pointed out that both the grain size and strains in the sample will result in the broadening of the XRD profile peak. Hemker [69] pointed out that dislocations can be sources of inhomogeneous strains in the sample and will contribute to the peak broadening. Newly developed techniques allowed in situ peak

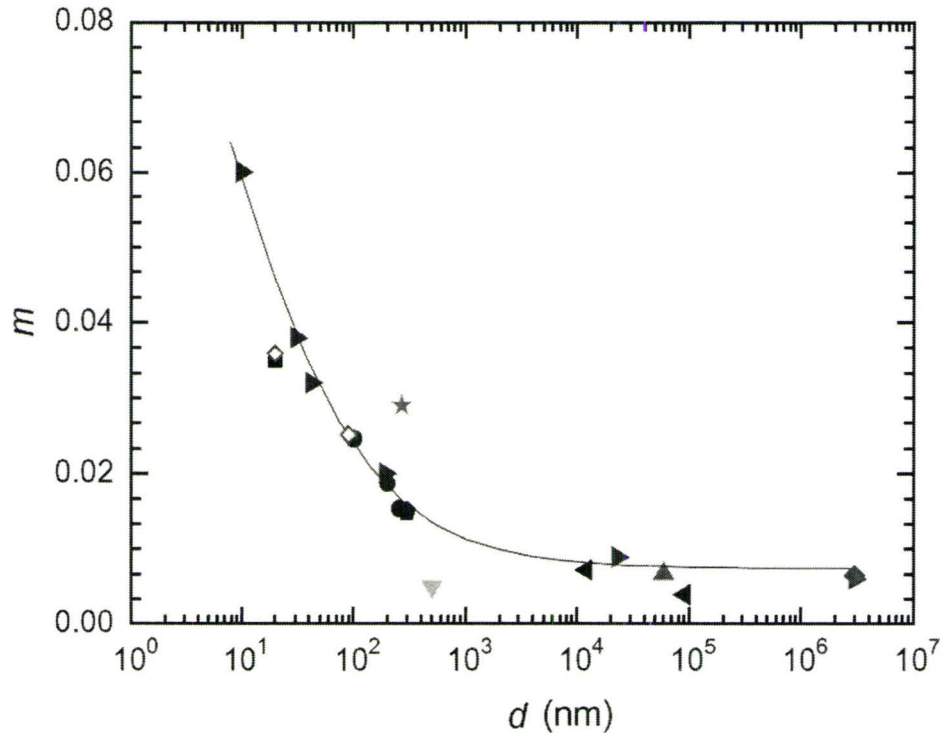


Figure 3.10: Room temperature strain rate sensitivity m as function of grain size for Copper. Note the step increase in NC regime [68].

profile analysis of samples to be deformed in the high power Swiss synchrotron light source. These in situ observations were in agreement with previous studies on NC materials. When NC Ni was loaded, the XRD peak widened and then it was completely reversed upon unloading. This result is in agreement with molecular dynamics simulation predictions (section 3.2), suggesting that dislocation are generated at the GB upon loading and are absorbed by GBs after unloading, leaving no dislocation debris [70] in the sample.

Scanning Electron Microscopy (SEM)

SEM is usually employed to examine fracture surfaces in samples. Fracture observations in NC Ni-P alloy showed traces of plastic deformation on the samples from 9nm to 37nm, though no traces of deformation were found above 37nm grain size. The authors concluded that the sample with smaller grains (less than 37nm in

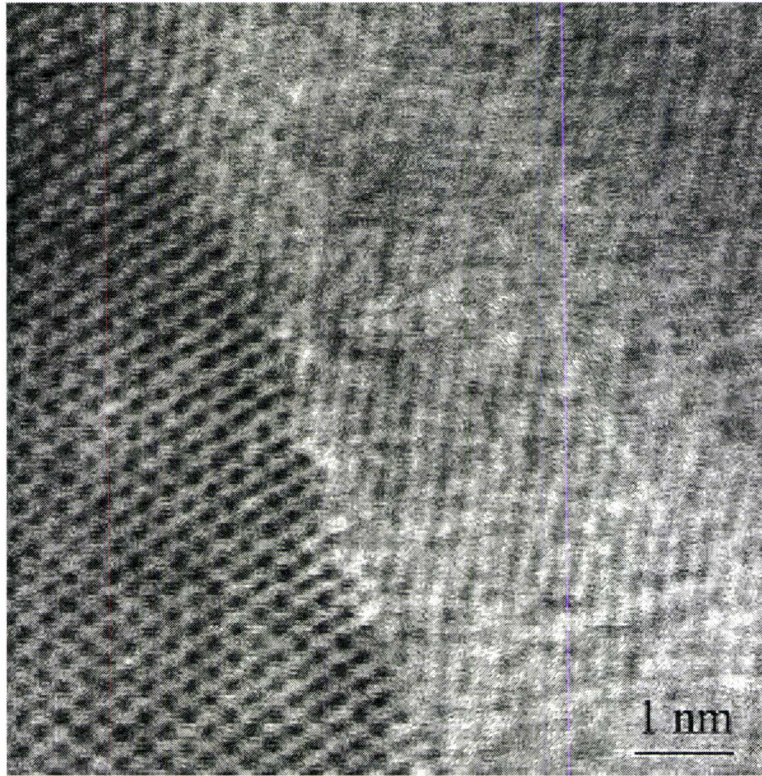


Figure 3.11: High resolution TEM images of the nc-Ni showing a clean atomically faceted grain boundary [22].

size) have a stronger tendency toward a plastic deformation (i.e. a lower strength an observation that implied a "reversing" of the HPR [34]).

Transmission Electron Microscopy (TEM)

TEM is the usual technique used to characterize NC grain boundaries. In the early days of nanotechnology, high resolution TEM studies indicated that the GBs in the as-prepared samples are in a non-equilibrium state and may be transparent to dislocations [39, 47]. Evaluation of grain boundaries of samples with average grain sizes of less than 10nm revealed considerably thicker grain boundaries, which supported the theory that grain boundary thickness increases with decreasing grain size, which in turn may have an effect on hardness in the GB region [29]. More recent experiments, however, suggested that GBs in NC materials are not anomalous but

similar to those found in polycrystalline materials and showed an absence of any grain boundary phase or amorphous regions (Fig. 3.11). The postmortem (after the deformation) TEM observations of deformed nanocrystalline metals have failed to uncover any evidence of dislocation activity, which suggests that traditional dislocation sources cease to operate below 100nm average grain sizes.

More recent in situ studies of NC materials deformation under TEM revealed evidence of dislocation motion. Kumar [22] concluded that the sources of plasticity during the deformation of NC Ni included dislocation activity, void nucleation, and void growth. Besides dislocation activity, deformation twins were found in ex-situ samples. Presence of deformation twins suggested partial dislocations activity in the samples. Samples of NC aluminum with average grain sizes ranging from 10–35nm revealed the formation of deformation twins [71] (Fig. 3.12). Further experiments using NC Ni showed that the formation of deformation twins depended on temperature. During uniaxial tensile test at cryogenic temperatures, severe partial dislocations mediated deformation was observed [72]. The generation of twin interfaces and stacking faults offers an alternative mechanism, to dislocation pile-up at grain boundaries, to explain the continuous grain size strengthening of NC materials.

Before we move on, it is interesting to point out that, while experimental observation usually precedes theoretical explanation, this was not the case for the mechanism of twinning in nanocrystalline aluminum. Twinning was, for the first time, observed using large scale *computer simulation* [73, 74] and then later confirmed by the above mentioned TEM studies.

3.2 Computer Simulation Studies

Advances in computing have made it possible to study systems of millions of atoms, enough to represent physical structures on the nanometer scale. Modeling the NC microstructure at the atomic level is widely known as *atomistic computer simulation*. Simulations performed on massively parallel supercomputers can provide details on deformation processes at the atomic level. One can perform virtual tensile-strength tests, stretching the crystal and seeing how individual atoms move. The position of every atom in the sample during the course of deformation is determined

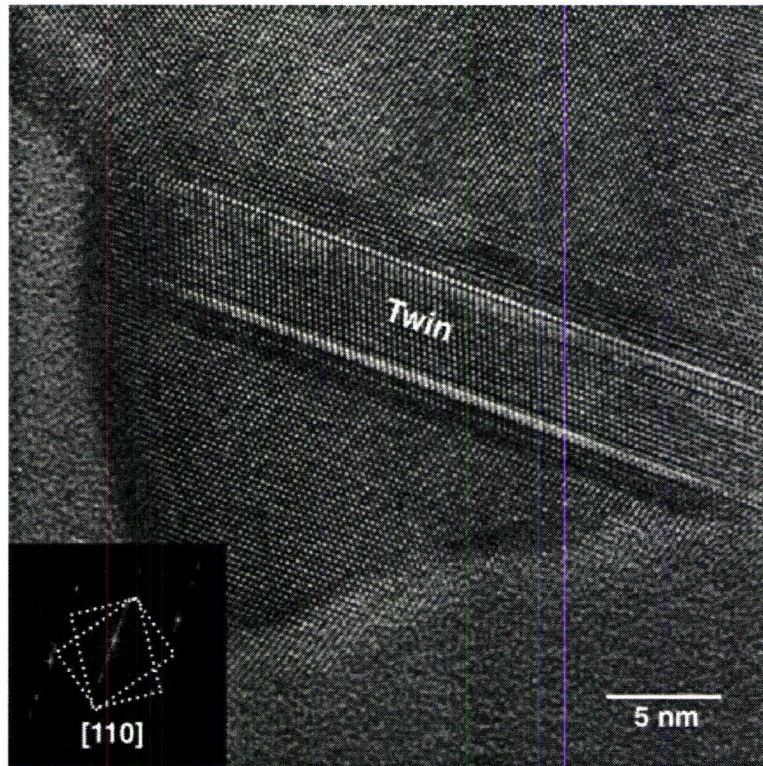


Figure 3.12: Nanoscale deformation. High-resolution transmission electron micrograph of a twin in deformed nanocrystalline aluminum [71]. This atomic resolution image illustrates the mirror symmetry between the twin and the matrix. The presence of the twin and the fact that it extends from one side of the grain to the other is unique to nanocrystalline aluminum.

and recorded. In present time, it is possible to simulate samples of three-dimensional networks of up to the order of 15 grains with a 20nm diameter, or 100 grains with a 10nm diameter, as depicted on Fig. 3.13. The main advantage of computer simulations is that they allow the non-invasive study of deformation processes. They also allow us to virtually synthesize and investigate NsM that are free of defects (pores, etc). The main atomistic-scale simulations that have been applied to NC metals are *Molecular Dynamics* (MD). The main part of MD simulation is the physical model of the system. In MD, Newton's second law is solved numerically for all atoms in the

system.

$$\frac{d\mathbf{p}_i}{dt} = -\nabla_{\mathbf{r}_i} V(\mathbf{r}_1, \dots, \mathbf{r}_n) \quad (3.1)$$

where $V(\mathbf{r}_1, \dots, \mathbf{r}_N)$ represents a potential energy. Potential energy describes the forces of interaction between particles. The validity of simulation results then depends on how realistic the description of the physical system a given potential energy offers. Examples of types of atomistic simulations are ab-initio, classical potential methods and semi-empirical methods.

The first group, as the name suggests, calculates forces between atoms from the first principles and is characterized by high accuracy, long simulation times, and high demand on computational resources.

The second approach calculates interaction between a pair of atoms based on a pair potential, such as the Lennard-Jones Potential or the Boyer Potential [75]. The shortcoming of this approach is that it does not correctly represent interactions in metallic materials.

To alleviate the above mentioned problem, semi-empirical methods are used, where pair potential is replaced with many-body potential, which takes into account the interactions between many atoms.

Without going further into the details of these simulations, let us now mention some of their interesting results.

In 1998 Schiøtz et al. [5, 77] simulated the MD of crystals with grain sizes of 3–6nm using an inter atomic potential for copper. When uniaxial deformation was applied, the stress-strain variation showed the expected yield and plastic flow. When these results were correlated with the grain size, they indicated a reverse HPR - a stress reduction with decreasing size. They predicted yield strength in the range of 1 – 1.2GPa for corresponding grain sizes of 6 – 3nm. The absence of thermally activated process in these simulations, made a direct comparison of these results with those of other experiments difficult. Interestingly, these simulations revealed the deformation processes that occur inside deforming material. The deformation process was characterized as grain boundary sliding, with an occasional nucleation of a partial dislocation from GBs. We know from dislocation theory [78] that the positions of atoms between two Shockley partial dislocation are altered. Similarly

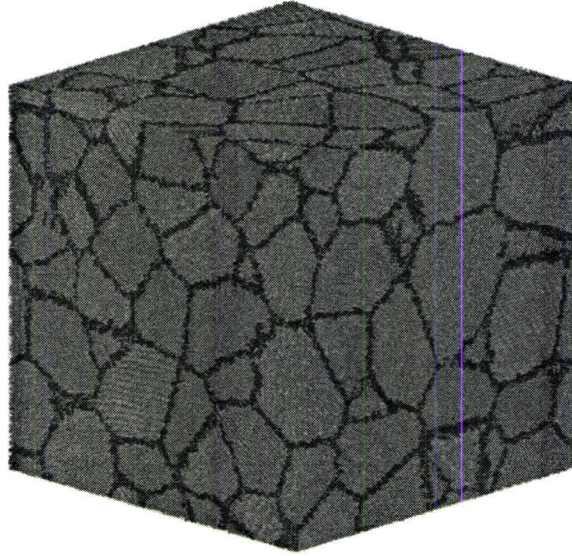


Figure 3.13: Grain boundaries at nanoscale. 37x37x37nm sample of Ni with mean grain size 10nm contains 4.6 million of atoms. Gray atoms sit in perfect crystalline positions, colored atoms are grain boundary atoms [76].

as partial dislocation emitted from GB moved through a grain, a stacking fault was created.

Yamakov et. al. (Fig. 3.14) studied systems of 4 columnar, hexagonally shaped grains with sizes ranging from 20 to 70 nm. In smaller samples they observed the emission of partial dislocations $1/6[112]$ from GBs. As the moving partial dislocation passed through the grain, a stacking fault was left behind, increasing the energy of the crystal. At higher grain sizes, the energy became too high and a second partial dislocation was emitted from the grain boundary, 'healing' the stacking fault and creating an extended dislocation $-1/2[110]$. Authors Yamakov et. al. concluded that the type of dislocation nucleated depends on the grain size and resolved shear stress. They rationalized the mechanism by comparing the distance r between two partial dislocation and average grain size d . The splitting distance r depends on the stacking fault energy Γ , the resolved shear stress σ , and the Burgers vector of partials b according to equation [80]:

$$r = \frac{K_1 b^2}{\Gamma - K_2 \sigma} \quad (3.2)$$

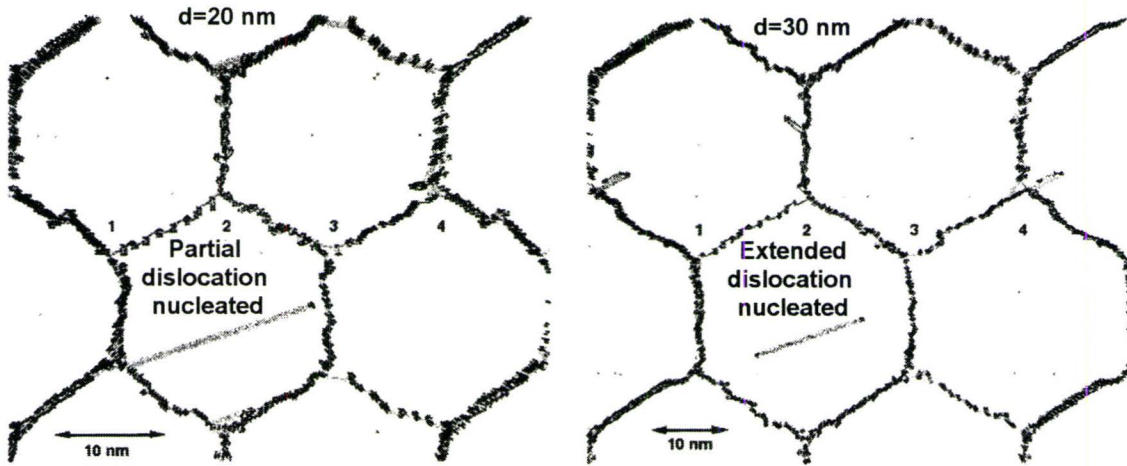


Figure 3.14: Sample with $d = 20\text{nm}$ at 14.6ps nucleated a partial dislocation $1/6[112]$. Contrary the sample with the 30nm grain size nucleated an extended $1/2[011]$ dislocation at 27.6ps . The extended dislocation consists of two partials connected by stacking fault. Applied stress is 2.3GPa in both cases [79].

where K_1, K_2 are materials constants. Large applied stresses, which are characteristic for MD, will result in significant values of r . Values of r higher than the grain size d might prevent nucleation of full dislocation. The actual deformation mechanism will depend on the interplay between r, σ and d . We will consider the following cases. If $d < r_{split}$ and $\sigma > \sigma_{flow}$, partial dislocations are nucleated from the grain boundary, but limited by the grain size, and the emitted partial dislocation will be absorbed by the opposite GB before an extended dislocation can be nucleated. On the other hand, if the grain size is bigger than r_{split} , then an extended dislocation will be formed. In the case when resolved shear stress is less than the flow stress, other than dislocation mediated deformation mechanism will prevail.

The further study of the NC Al system uncovered the presence of deformation twinning [73]. Twins were formed by the concurrent emission of partial dislocations from the same GB and the splitting and subsequent migration of GB. Deformation twinning is well known in FCC systems, such as brass, but was not expected in aluminum given the high stacking fault energy of Al. As in the previous case, these studies pointed out significance of *stacking fault energy* and its effect on the strength of

NC materials. In addition to processes inside the grains, the interaction of dislocation and GB was revealed. As seen on Fig. 3.15, after a 12% deformation GBs that were originally flat became rough even as new grain was nucleated at the center of the sample.

Yamakov et. al. [81] further studied samples of NC Al with average grain sizes of 7, 10, 18, 24 and 32nm to uncover the transition from the strengthening effect of grain refinement to reversed behaviour. Similar to the above paragraph, they observed no dislocation activity, only a partial dislocation mediated deformation for the smallest grains. In the largest grains dislocation slip was observed. Analyzing the plastic strains in the sample during the deformation they were able to pinpoint the transition to reversed behaviour the 18nm grain size.

Schiøtz and Jacobsen [82] explored grain size dependence of flow stress in NC Cu samples with grain size ranging from 5 to 50 nm. They showed an increase in the flow stress with increasing grain size for samples up to 12nm. Observations of the microstructure during the course of deformation uncovered grain boundary sliding mediated deformation. The flow stress began to decrease for grain sizes above 15nm. In this case, deformation was primarily mediated by dislocation motion through the grains, although in some grains, grain boundary sliding was observed. Plotting the flow stress against the grain size showed that the grain size with the highest flow stress - the "strongest size" - is in the range of 12 to 15nm. Another important feature observed during the deformation was the formation of dislocation pileups (see section 4.1) in grains sized 50nm. Pileups contained 5-6 dislocations and were 35 to 40 nm long.

3.2.1 Current Status and Limitations

Even though atomic-scale simulations contributed to the understanding of NC materials, one has to be aware that they cannot be directly applied to the deformation of common engineering metals as they are currently limited to sample sizes of about $100nm$.

More importantly, the typical time step of molecular dynamics simulation is of the 1fs (10^{-15}) order, below the vibrational period of an atom. As a result the strain rate required to achieve acceptable simulation time has to be at least 10^7s^{-1} .

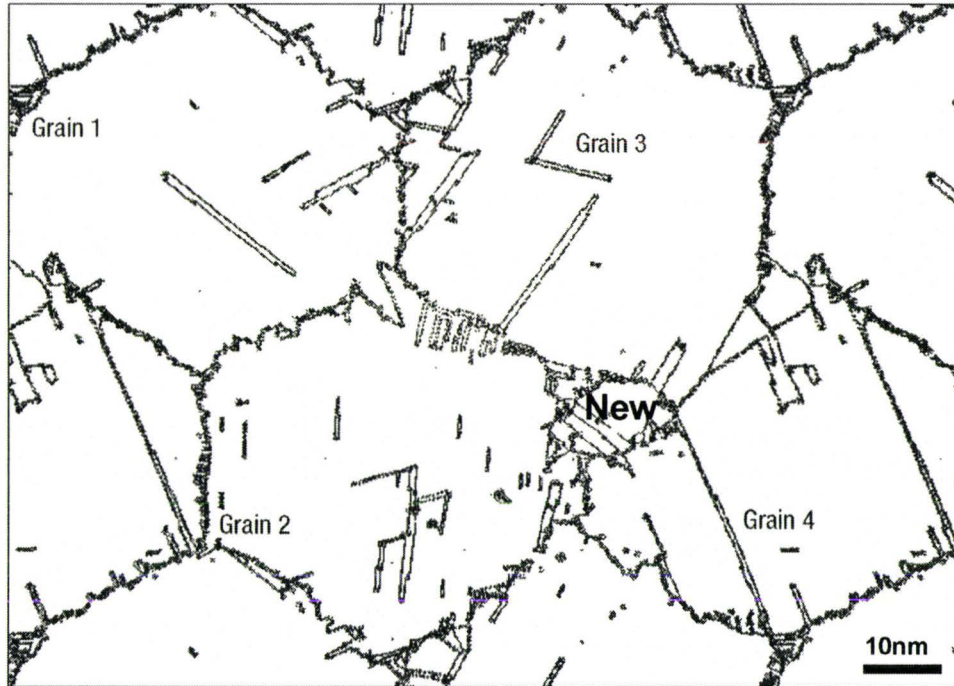


Figure 3.15: Snapshot of NC Al structure at 11.9% strain. Variety of processes taken place. GBs are curved, a "new" grain was nucleated and a number of twins can be observed inside the grains [73].

For example, the transition to reverse 'HPR' in [82] was observed under strain rates $5 \times 10^8 s^{-1}$ within the $200ps$ of simulation time. This is to be contrasted with the much slower experimental strain rates of 10^{-5} to $10^{-3} s^{-1}$ reported in section 3.1.2. Moreover, to achieve the deformation of 1% in about 1ns very high applied stresses have to be used. For example, the above mentioned studies by Yamakov et. al. [81] used a constant tensile stress of 2GPa applied to each sample. Unusually high applied stresses and strain rates raise the question to what extent MD simulations are comparable with experiments.

Van Swygenhoven [83] suggested that macroscopic stress-strain curves from MD might be misleading and the only meaningful information obtained from MD simulations are observations and a classifications of the atomistic processes during the deformation.

Chapter 4

Deformation Mechanisms of Nanocrystalline Metals: A Summary

In the previous chapter we described the mechanical behavior of NC materials as observed in experimental studies and in numerical simulations. In this chapter we will attempt to collect these separate results into a single picture describing a proposed deformation mechanism of metals with a decreasing average grain size. Using the same philosophy as in the introduction we can divide the scope of our new plot into three groups. Micro-, ultrafine- and nanocrystalline metals.

4.1 Microcrystalline Metals

It was mentioned in chapter 3 that the relationship between the yield strength and the grain size has been of interest to many authors. We also reviewed (Fig. 3.1) the work that was performed by Hall and Petch [3, 4], where they plotted yield strength σ_y against the inverse square root of the grain diameter d to obtain a linear relationship later known as the Hall-Petch relationship. This relationship can be written as follows:

$$\sigma_y = \sigma_0 + k \frac{1}{\sqrt{d}}$$

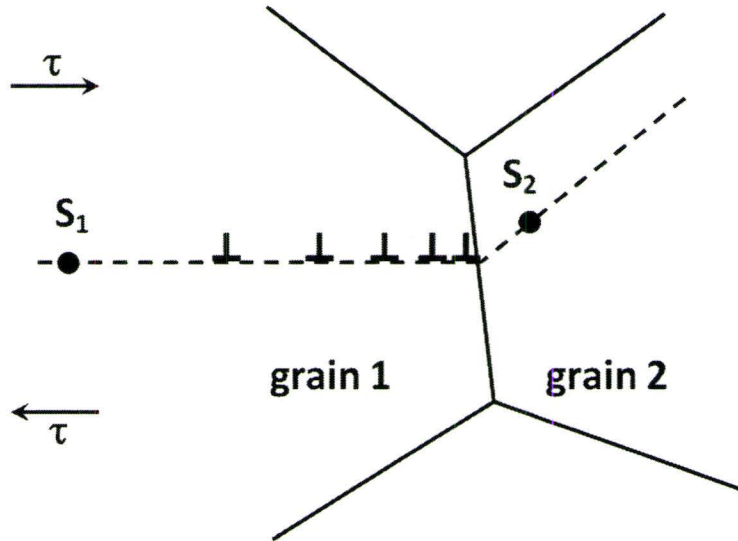


Figure 4.1: Schematic illustration of a pile-up formed in grain 1 and applied resolved shear stress τ . S_2 is a source in grain 2. Dashed line would represent preferred slip planes [84].

where, k is a measure of the stress required ahead of the array of dislocations for the propagation of yield or cracking [85]. σ_0 is the friction stress that opposes the motion of the dislocations.

This theory was rationalized through the *pileup* of dislocations at grain boundaries, created in the process of plastic deformation. Consider a grain with a dislocation source at S_1 [grain 1 on Fig. 4.1]. Suppose that that the stress required to operate the source has been achieved. Dislocations emitted from S_1 will experience repulsion near the the grain boundary interface. Dislocations will pile up along the glide plane behind the grain boundary film. The stress concentrations cause the GB to yield. Deformation is then transferred to the next grain [grain2 on Fig. 4.1], where a second dislocation source starts to operate.

The MD simulations on NC copper reviewed in section 3.2 revealed the presence of dislocations pileups inside grains larger or close to 50nm. These observations suggested that indeed the dislocation pileups are the mechanism behind the grain size strengthening.

It was shown that σ_0 reduces the stress produced ahead of the array of disloca-

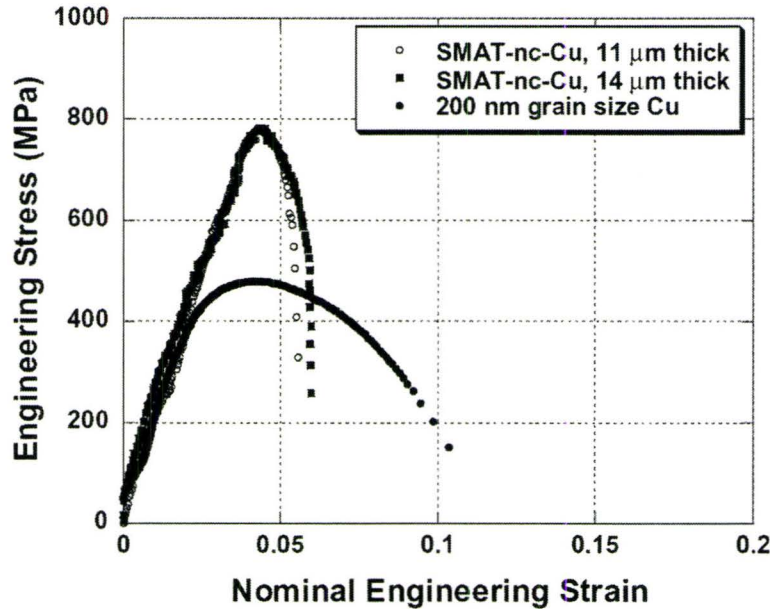


Figure 4.2: Tensile Engineering Stress-Strain curves of two NC Cu samples compared with UFC Cu [60].

tions piled up against the grain boundary film, and that it depends in part upon the frictional forces exerted by solute atoms, precipitates, and on the dislocation arrays that propagate the yield. It was also proved that σ_0 increases when the solute atom concentration is increased, by nitriding or by quenching and ageing [86].

4.2 Ultrafine Crystalline Materials

Results reviewed in previous chapter (Fig. 3.5 and Fig. 3.6) suggested that strength increases with decreasing grain size up to grain sizes somewhere in the neighborhood of 50nm grains sizes. As displayed on Fig. 4.2 and Fig. 3.5j,o tensile tests on UFC Cu with grain size close to 200nm showed yield strength of 400MPa, which is more than double that of their microcrystalline counterparts displayed on Fig. 3.1. SEM micrographs of these samples revealed a dimpled fracture surface, which suggested that fracture in ultrafine grained material was ductile i.e. mediated by plastic deformation [60, 54, 57]. More detailed exploration of UFC silver samples by HREM

confirmed signs of plasticity in grains with sizes of 200nm [87]. Deformation strains concentrated inside the grains suggested that dislocation mediated deformation is the dominant deformation mechanism in ultrafine grained materials.

4.3 Nanocrystalline Materials

Experimental results and atomistic simulations both suggested that below certain grain size ($\approx 100\text{nm}$) overall dislocation activity decreases and dislocation processes at the GBs become more dominant. An important question regarding grain boundary strengthening is what will happen with decreasing grain size below $\approx 100\text{nm}$. The main theoretical arguments claim that as the grain size in a polycrystalline material decreases, there arrives a point at which each individual grain will no longer be able support more than one dislocation; at this point the Hall-Petch relationship will no longer hold. From another point of view, when the grain size approaches zero, the material essentially becomes amorphous. The grain boundary strengthening effect will then disappear. The strength will reach a maximum where the Hall-Petch relation is fulfilled, but at the same time the dislocation microstructure is also favorable. This is schematically illustrated in Fig. 4.3. It was also shown in the previous section that at the critical grain size, the two mechanisms of grain boundary sliding and dislocation mediated deformation compete.

4.3.1 NC Materials - Strength Above Critical Grain Size

Summarizing experimental evidence from chapter 3, it is indicated that NC materials exhibit significantly higher yield strength than coarse grained materials. Furthermore, hardness and yield strength have been found to increase with decreasing grain size up to grain sizes 15 – 20nm. As the grain size decreases to the NC regime, dislocation activity shifts to GBs until it ceases at the critical grain size. Little is known about this process. Atomistic simulations partially uncovered that, as grain size decreases below 50nm, only grain boundaries act as sources of partial or full dislocations depending on grain size and the stacking fault energy associated with partial dislocations. The presence of partial dislocations and stacking faults lead to the formation of deformation twins. The generation of stacking faults and twins

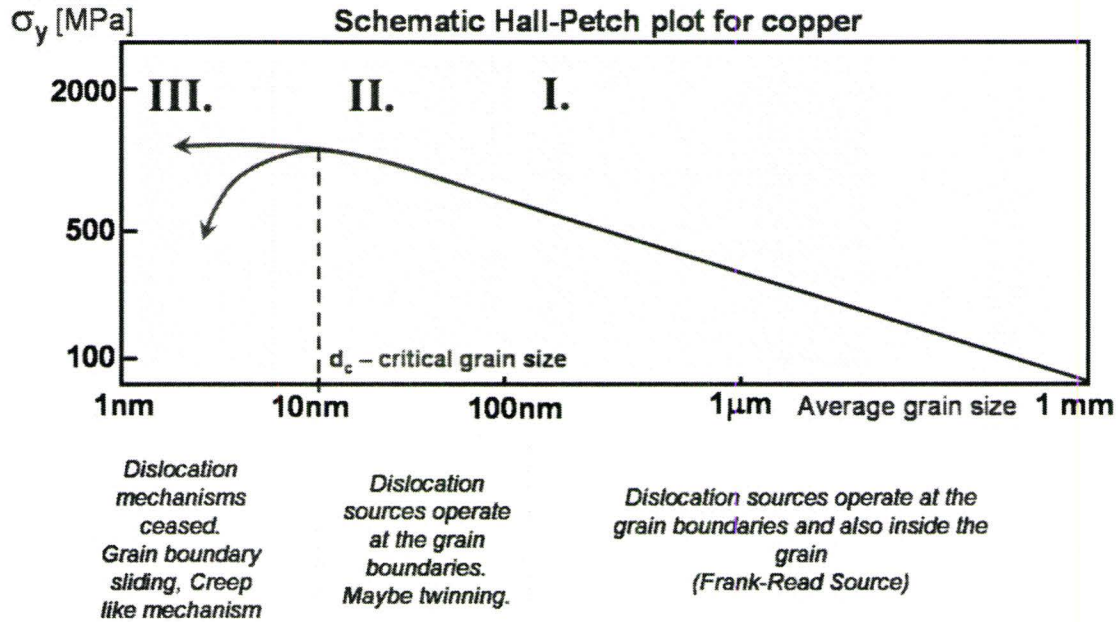


Figure 4.3: Deformation mechanism map for copper. Adapted from [38].

can be one way to rationalize strengthening below grain size of 50nm, where only small numbers of dislocations are present. These results allow one to predict the deformation mode, but to characterize it, some theoretical model is needed. Asaro et. al.[88] developed a theoretical model for deformation of nanocrystals considering the emission of partial dislocation from the GBs. Another recently published model suggests theoretical transformation of low and high angle grain boundaries under plastic deformation. In this model, decayed low angle and bowed high angle GBs act as active dislocations sources [89].

4.3.2 Softening of NC Materials - Strength Below Critical Grain Size

For grain sizes approaching ≈ 10 -20nm, experimental evidence (see section 3.1.2) and computer simulations (see section 3.2) have indicated a decrease in the strength and hardness. It is expected that other than dislocation processes will govern defor-

mation below $\approx 20\text{nm}$.

Grain Boundary Energy Models

Gleiter [2] argued that grain boundaries in NC materials are essentially different from those in conventional materials; they are of low density and in a gas like state of disorder. On the other hand, some studies of NC materials suggested that GBs in NC materials have a lower interfacial energy due to high-volume fraction of GBs. This decrease of interfacial energy should result in a decrease in the ability to cease movement of dislocations at the GB. In other words, grain boundaries will exhibit certain transparency to dislocation movement, allowing dislocation to extend into several neighboring grains [90]. Neither of these theories have been proved by direct observations using TEM (Fig. 3.11) or atomic simulations Fig. 3.13, [91, 92]. They are more likely to suggest grain boundary properties similar to those in coarse grained materials i.e. materials with grain size in micrometer range.

Creep and Grain Boundary Sliding Models

It was suggested in the early days of NC materials that below the critical grain size – in other words below the size when dislocation activity has ceased – the mechanism for deformation will be creep-like - based on *Coble creep*. The theory of Coble creep is simple. The energy that is required to form a vacancy at the top or bottom surface of the grain (Fig. 4.4) is different from the energy required to create vacancy at a side surface if a vertical tensile stress is applied to the grain. From knowledge of the rate of flow of vacancies, it is possible to calculate the rate of change of the grain dimension in the direction of the applied stress [93]. When grain boundary diffusion is added to lattice diffusion, a formula for the Coble creep rate will be:

$$\dot{\epsilon} = \frac{B\sigma\delta\Omega D_{gb}}{d^3kT} \quad (4.1)$$

where B is a constant, σ is applied stress, δ is the boundary thickness, Ω is the atomic volume, and D_{gb} is the boundary diffusion coefficient. Thus NC creep rates would be enhanced by a factor of 10^9 compared to those for micrometer grain size materials. Even though the calculation for copper suggested creep rates of $6 \times 10^{-3}\text{s}^{-1}$ for

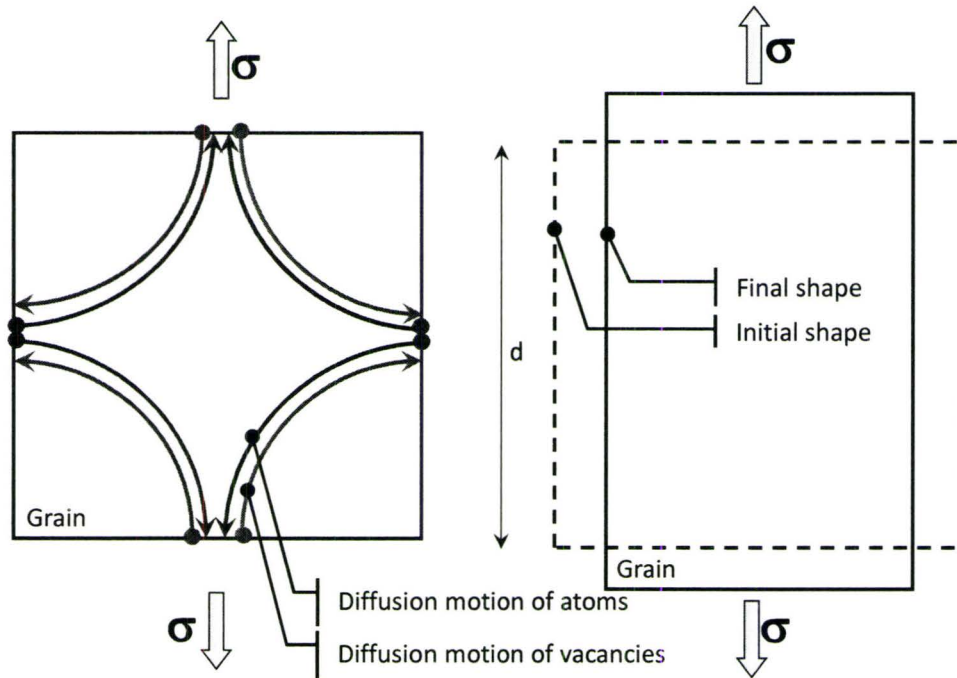


Figure 4.4: a) Mass motion of vacancies and atoms across a small grain and at a high temperature under applied stress. b) Change in shape of a grain under the mass motion shown in (a) [93]. In Coble creep mechanism mass transport is more narrowly focused to the GB region.

$\sigma=100\text{MPa}$ and $d=5\text{nm}$, direct creep measurements on NC Cu a Pd did not prove [59] this explanation and thus this remains an unanswered question. By contrast MD simulations [81] suggested creep like deformation mechanism with strain rates consistent with Coble creep mechanism. Other MD simulations [77, 82] and theoretical studies [94] suggested a deformation by the grain boundary sliding mechanism. However, it has to be pointed out that these two process must act in parallel to prevent internal void or cracks. After the grain is deformed by diffusional creep (Fig. 4.4b) one dimension is extended and the other lowered; to compensate for this change grain boundaries must slide by exactly the distance changed by diffusional creep. This theoretical observation would reconcile discrepancies between observations of both Coble creep and GB sliding.

From other proposed mechanisms for deformation on the lowest grains size level

let us mention the mechanism of rotational deformation in nanostructures suggest by Ovidko et.al. [95]. As plastic deformation proceeds, two grains might rotate and coalesce or bring their orientation closer together. The proposed mechanism suggested that deformation is mediated by a motion of line defects – disclinations.

In general, the results of all proposed theoretical models and NC copper observations data are summarized in Fig. 4.3, which describes the deformation of copper from micro- to nano-scale.

Chapter 5

Compositional Domain Boundaries and Strengthening: Role of Dislocations in Spinodal Decomposition

The experiments and computational simulations discussed in the previous sections suggested that the strength of materials is effectively increased by hindering the dislocation motion through the introduction of grain boundaries. Other obstacles such as solute atoms or second phase particles, have produced a similar effects. In the case of a second phase particle, the change in concentration between the matrix and a particle is rather sharp, as seen on schematic 5.1b. This is not the case during the process of *spinodal decomposition* were at early stages of phase separation the fluctuations in concentration are smooth - Fig. 5.1a. The rest of this chapter will discuss the process of spinodal decomposition and how these smooth compositional domain boundaries interact with dislocations and thus contribute to binary alloy strengthening.

Consider a binary alloy of composition X_o , with a phase diagram with a miscibility gap as shown in Fig. 5.2, heated to a temperature T_1 and quenched to T_2 . Initially the composition will be homogeneous everywhere (first slide on Fig. 5.1a) and its free energy will be G_0 . The free energy is plotted under the phase diagram on Fig. 5.2. The alloy will be unstable and the initial homogeneous phase will sponta-

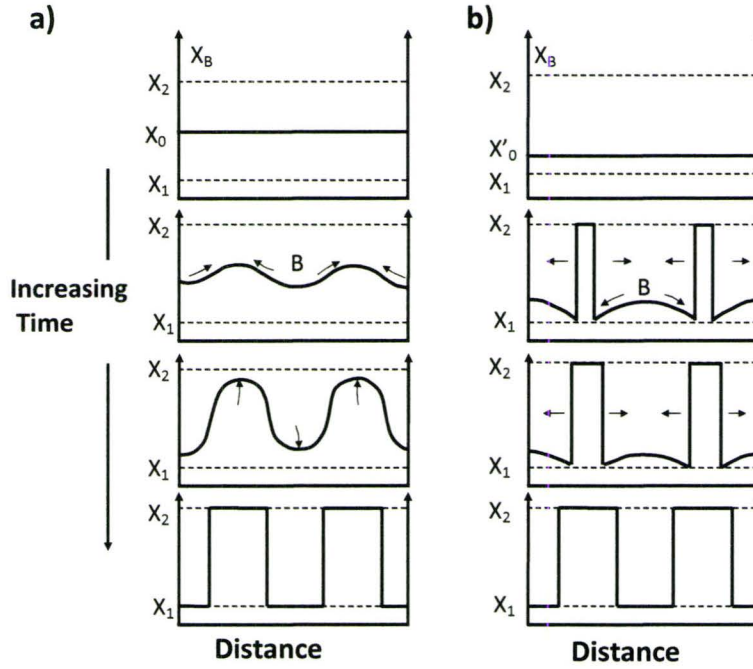


Figure 5.1: Growth of homogeneous fluctuation (a) and heterogeneous nucleation and growth (b) [96].

neously decompose into two daughter phases, lowering the total free energy (second slide on Fig. 5.1a). This mechanism of growth is only observed in the center part of the coexistence region, which is limited by the *spinodal curve*. This process is called spinodal decomposition. Entropy of mixing will increase with increasing concentration of species A or B, causing the free energy to decrease on both sides of the free energy diagram. Furthermore, we can see from Fig. 5.2 that the free energies for concentrations X_1 and X_2 lie on the linear line defined by the lever rule. Inside the coexistence region, free energy has a metastable part with a positive curvature and an unstable part with a negative curvature. The transition from negative to positive curvature defines the location of the spinodal line, or line which defines if domains will grow by nucleation and growth mechanism or by spinodal decomposition. The free energy for phase separation by spinodal decomposition is written as:

$$F = \int [f(c) + \kappa(\nabla c)^2] dV, \quad (5.1)$$

where $f(c)$ is the free energy of homogeneous composition, it has two wells. One for each phase. The second term, $\kappa(\nabla c)^2$, is the additional free energy density to account for gradients in concentration, where κ is a constant that sets the scale of the gradients energy due to compositional variations [97].

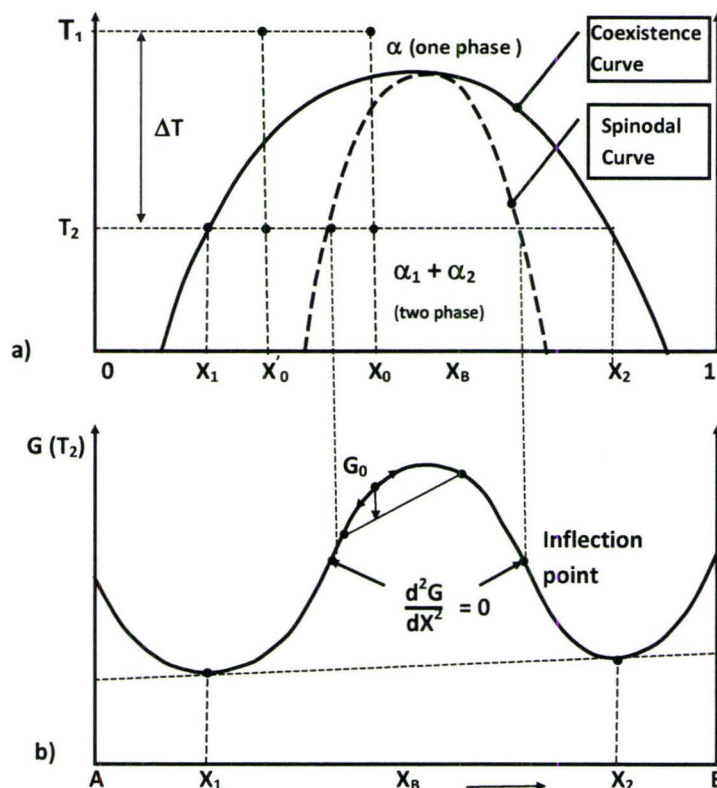


Figure 5.2: Alloy with concentration X_0 will decompose into coherent phases α_1 and α_2 without having to overcome an activation barrier. Transformation of an alloy with concentration X_0' must proceed by nucleation and growth [96].

During the process of spinodal decomposition, the domains of alternating concentration grow and coarsen to a scale of tens of nanometers. Although concentration fluctuations, displayed on Fig. 5.1a, are smooth and less pronounced in the beginning of the growth process it was shown that they interact with the dislocations. Cahn [99] and Kato et.al [100] studied how internal elastic fields and concentration gradients exert force on dislocations. Cahn analyzed dislocations in several slip systems in FCC to find strengthening effect similar to that previously found in the systems with discrete

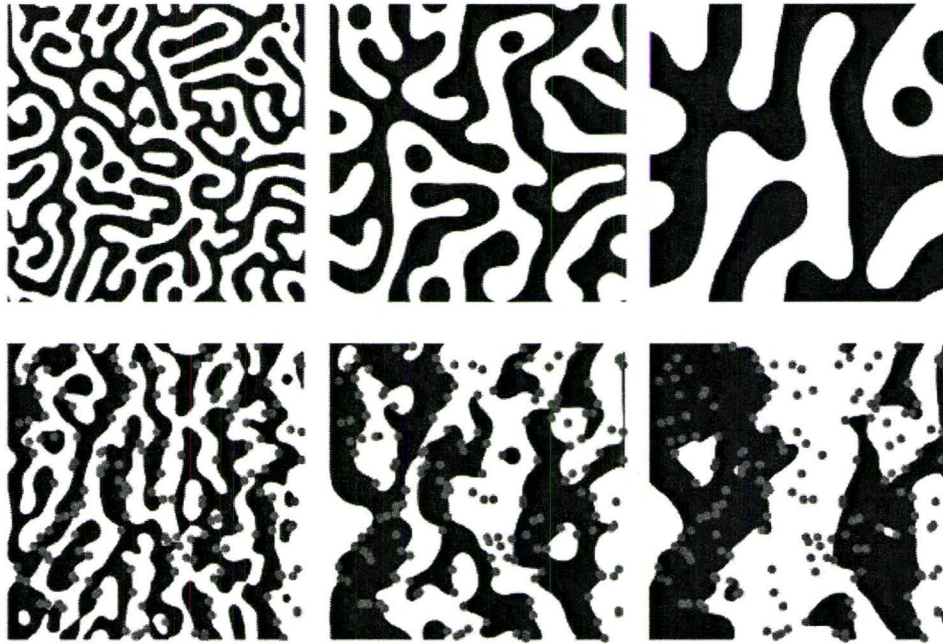


Figure 5.3: Léonard and Desai showed the presence of immobile (uncooperative) dislocations influences phase separation. Both bottom and top figures represents the same time. The alloy at the bottom contains dislocations while the alloy at the top is dislocation free [98].

particles. If the spacing between particles was small, the strengthening effect (stress to push a dislocation through "compositional" obstacles) would be linearly dependent on spacing. For particles with large distances the strengthening effect was inversely proportional to $2/3$ power of the distance. In the above cases, a force balance on an individual dislocation was used to calculate the interaction between microstructure and dislocation stress field.

The kinetics of phase separation was later studied using the previously mentioned free energy $F = \int [f(c) + \kappa(\nabla c)^2] dV$ and diffusional phase field dynamics:

$$\frac{\partial c}{\partial t} = \nabla \cdot \left(M \frac{\delta F}{\delta c(\vec{x})} \right). \quad (5.2)$$

The free energy in Eq. 5.1 can be expanded by replacing free energy density f with $f + w$ where w accounts for elastic free energy density. Cahn was the first to calculate

that the driving force for the nucleation of an incoherent second phase precipitate is higher on a dislocation than in the bulk solid [101]. A similar result was obtained by Dollins [102] for a coherent precipitate in the presence of edge dislocation with isotropic elastic properties in solid solution. Léonard and Desai [98] used Ginsburg-Landau formalism to write the free energy of the system. They analytically solved terms for elastic energies due to *a)* dislocations and *b)* the interaction between compositional stress field and dislocations. These elastic terms were then added to the general expression for the free energy. This, in turn, was used in a Cahn-Hilliard type dynamic equation to study the effects of static dislocations on the kinetics of phase separation. According to their findings, presence of dislocations changed both morphology and kinetics of spinodal decomposition. From Fig. 5.3, we can see that the compositional field is trying to accommodate stress field from immobile dislocations. Kinetics was affected only at the early stages of decomposition where accelerated phase separation was found. Hu et. al [13] expanded on the work of Léonard and Desai using a phase field model to simulate dislocation response to elastic field exerted by compositional inhomogeneities as well as by structural defects such as other dislocations, grain boundaries, cracks and inclusions.

Haataja et al. recently introduced mobile dislocations into a phase field model that couples two burgers vector fields to solute diffusion and elastic strain relaxation. It was shown that mobile dislocations altered the early and intermediate time coarsening regime in spinodal decomposition [12, 103]. Specifically, it was found that coherent strain at phase boundaries decreases the intermediate coarsening rate, since it increases stored elastic energy in the system. As dislocations migrate toward moving interfaces, they relax the excess strain energy, thus increasing the coarsening rate [103]. The growth regimes predicted by the model in Ref. [103] are in general agreement (i.e. display behaviour consistent) with several experimental studies of deformation on spinodal age hardening [104, 105, 106].

Chapter 6

Summary of Outstanding Issues

This chapter lists several unresolved issues in previous studies of nanocrystalline deformation in materials. The items on this list were chosen as they describe a suite of problems that are most likely to be (or are presently) amenable to a new generation of phase field modeling, toward which this thesis will make two new contributions. Summarized below are some of the unresolved issues that have emerged from previous studies on deformation in nanocrystalline materials:

- The interpretation of experiments have raised controversy about the interpretation of results and sample quality preparation.
- Empirical models suggest different mechanisms for the transition to 'reverse' the Hall-Petch relationship.
- Atomistic simulations are limited to high strain rates with time step of picoseconds, orders of magnitude faster than any situation in an experiment.
- The presence and properties of mobile dislocations and their effect on domain growth in spinodal decomposition.

Part II

Phase Field Crystal Modeling of Nanocrystalline Materials

Make everything as simple as possible, but not simpler. A. Einstein

It was shown that the numerical tools that are presently used to examine mechanical properties of NC materials have certain pitfalls. Atomistic simulations have shed some light on behaviour and are currently able to describe: **a)** NC materials with grain sizes up to 50nm, **b)** time scales of picoseconds, which means that only beginning of the deformation processes can be observed. Moreover as was stated in the previous chapter, materials with sufficiently small grain sizes will exhibit creep-like deformation.

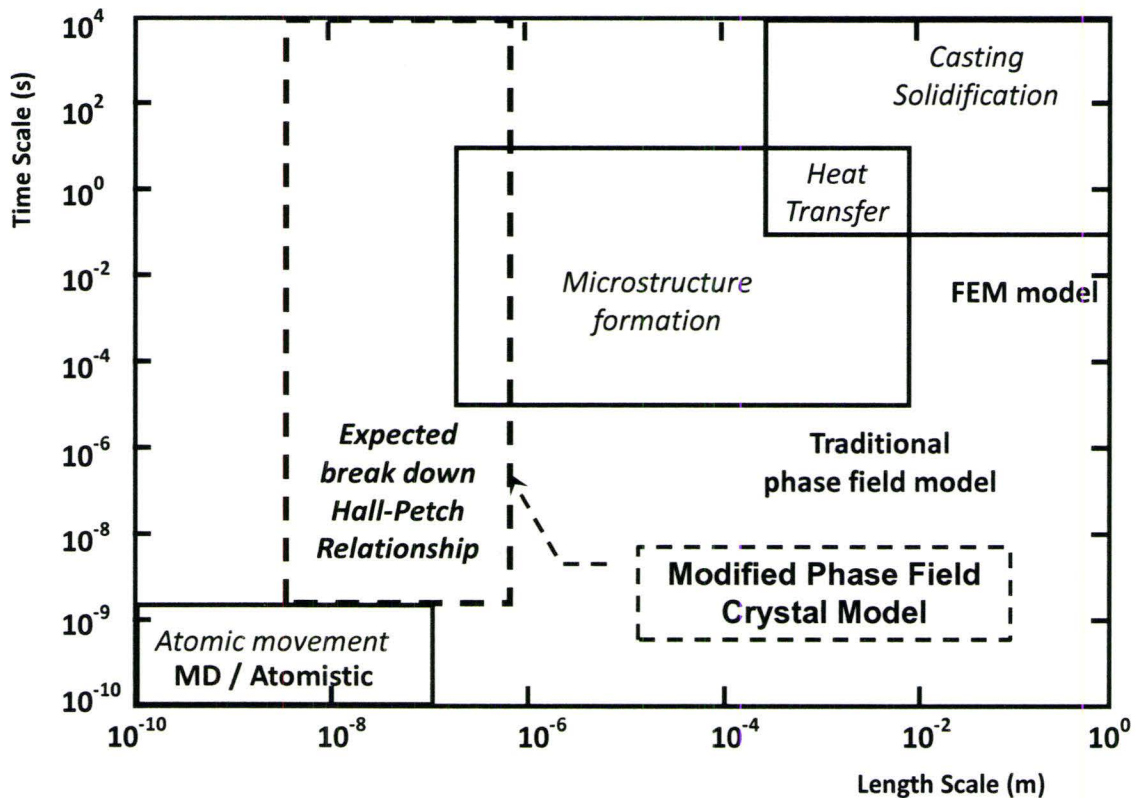


Figure 6.1: Plot of length scales and time scales accessible by common computational methods [107]. Characteristic processes for each length and time scale are in italics. Modeling techniques are in bold letters below. Dashed line highlights the modified phase field crystal (MPFC) methodology discussed in this thesis.

It is presently difficult to extrapolate results of atomistic simulation to the micrometer range. In order to describe deformation behavior as suggested on the Fig. 4.3, we need a computational methodology that can easily simulate grain sizes from nm to $10\mu m$ and time scales from *seconds* to *hours*. One way of solving this problem is to develop a phenomenological model, which is derived from fundamental principles but is robust enough to be solved at a variety of length and time scales. The objective of this thesis is to develop a new continuum field theory approach for modeling elastic and plastic deformation, free surfaces and multiple crystal orientations in systems with both hexagonal and cubic symmetry. The methodology is based on free energy and its dynamics – based on free energy minimization – incorporates both diffusive and elastic relaxation in solids. One of the models that we introduce is coined the modified phase field crystal model (MPFC). By introducing a variable elastic time, this model is able to maintain mechanical equilibrium while simulating microstructural evolution on time scales well beyond those accessible by conventional atomistic simulation methods. We apply this model to elucidate the role of defects and dislocations in fine grained crystal deformation and phase transformations - spinodal decomposition. Fig. 6.1 reviews time and length scales accessible by various computational tools and shows where our model will fit.

Chapter 7

A New Atomistic Modeling Formalism

The main principle underlying the new modeling formalism at the heart of this thesis and most materials processes is that macroscopic properties are governed by conservation laws and *broken symmetries*. In a system of particles, the number of particles, energy, and momentum are conserved. At high temperatures, the arrangement of particles is disordered, uniform, isotropic and uncorrelated. This implies a state of full rotational and translational symmetry. Symmetry of the system is lowered with decreasing temperature. A periodic crystal is invariant only with respect to a discrete set of translations. Broken symmetry is associated with distortion and defects. These defects control the properties (e.g. mechanical) of crystalline phases and materials.

In this chapter, we will introduce a new modeling technique using a density functional theory description of a crystal/liquid system written in terms of the local time averaged density field $\rho(\vec{x}, t)$. This representation of a crystal forming system will be then used to derive a free energy as a functional of this local density field. Based on variations in the free energy, a model producing periodic phase fields (i.e. crystals) and their dynamics will be constructed.

7.1 Atomic Density Field and Particle Interactions

7.1.1 Atomic Density

Consider a local, time averaged density field $\rho(\vec{x}, t)$. By this description, the liquid state is represented by a uniform ρ and the crystal state is described by the density that has the same periodic crystal symmetry as a given crystalline lattice. In this chapter we will elaborate on this density field. The starting point is the instantaneous number density of particles per unit volume at position \vec{x} [(x,y,z) in three dimensions], which can be defined by the following expression:

$$n(\vec{x}) \equiv \sum_{\alpha} \delta(\vec{x} - \vec{x}_{\alpha}), \quad (7.1)$$

where δ is Dirac delta distribution and x_{α} is the position of particle α at time t . $n(\vec{x})$ is called the number density operator and is a function of the variable x_{α} .

Taking the average of the density operator $\langle n(\vec{x}) \rangle$ (i.e. the local atomic density) for the different position \vec{x} (and a large enough volume) in liquid we would find that $\langle n(\vec{x}) \rangle$ is independent of \vec{x} and is simply the average density $n = N/V$, where N is a number of particles and V is a volume. This implies that liquids are *spatially homogeneous*. Thus, if one would rotate fluid around an arbitrary axis or translate it through any vector, the measured density of fluid would (on average) always be the same. In other words, liquids remain invariant to these *symmetry operations*. In crystals, $\langle n(\vec{x}) \rangle$ becomes a periodic function of \vec{x} and the number of symmetry operations leaving the crystal unchanged is limited. As a consequence, crystals have a lower symmetry than liquids. This is illustrated in Fig.7.1.

When a crystalline phase is formed, atoms are arranged in a periodically repeated structural unit called a *unit cell*. Equivalent points in unit cells in d-dimensional crystals lie on a *periodic lattice* consisting of a mathematical array of points. Any lattice point can be specified by a linear combination of independent primitive translation vectors $\vec{a}_1, \dots, \vec{a}_d$, (for a d -dimensional lattice):

$$\vec{R}_{\vec{l}} = l_1 \vec{a}_1 + l_2 \vec{a}_2 + \dots + l_d \vec{a}_d \quad (7.2)$$

where vector \vec{l} indexes a particular unit cell and $\vec{R}_{\vec{l}}$ specifies its position in real space.

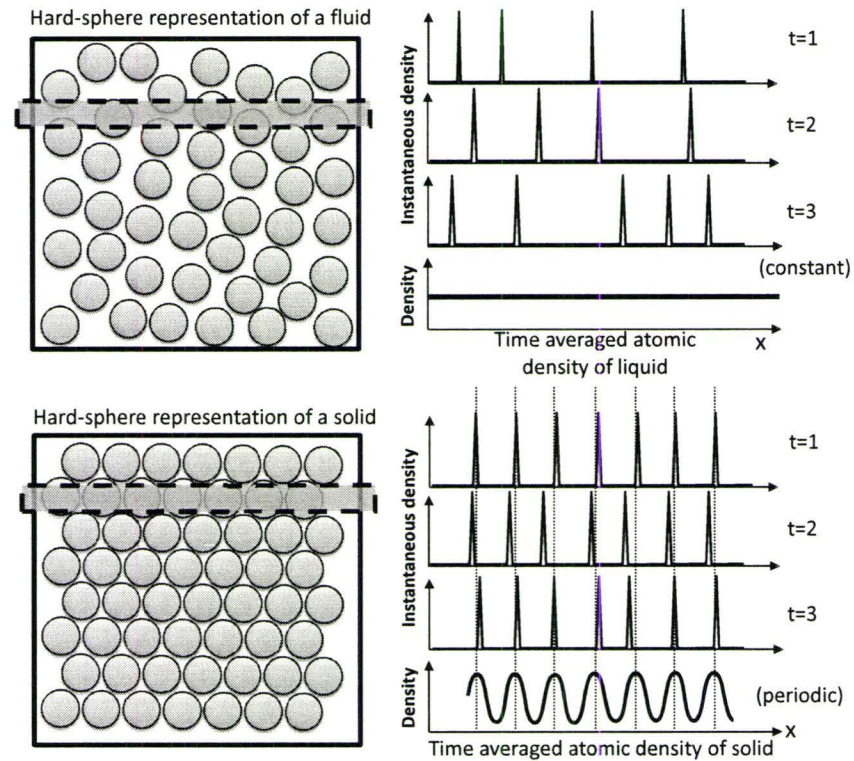


Figure 7.1: Hard sphere representation of liquid on top and solid at the bottom. Measuring the instant density in the control volume (marked dashed black) for number of time steps (right) will result in constant density profile in a liquid where atoms are constantly moving. Contrary in solids where atoms are moving only around the equilibrium position the atomic density profile will be a periodic field with periodicity of the lattice.

The translation vector $\vec{T} = \vec{R}_i - \vec{R}_j$ connects equivalent points in the lattice. The collection of lattice points in coordinate space is called the *direct lattice*. In an ideal crystal, consisting of a single type of atom located in each lattice site, the number density can be described as:

$$n(\vec{x}) \equiv \sum_{\vec{i}} \delta(\vec{x} - \vec{R}_i) \quad (7.3)$$

As mentioned above, the density of perfect crystal is invariant with respect to set of translations. One of these is translation through a lattice vector $n(\vec{x}) = n(\vec{x} + \vec{T})$. If we consider imperfections (such as vacancies, dislocations, etc.), we can consider the time-averaged density as having the periodicity of a perfect crystal:

$$\langle \rho(\vec{x}) \rangle = \langle \rho(\vec{x} + \vec{T}) \rangle \quad (7.4)$$

In this case, the effect of defect is represented through changes in amplitude of $\langle \rho(\vec{x}) \rangle$.

Atomic planes in a periodic lattice can be defined by the reciprocal lattice vector \vec{G} . Lattice vectors in a given plane are perpendicular to \vec{G} and satisfy $\vec{G} \cdot \vec{T} = 2\pi n$. The vectors \vec{G} form a periodic lattice, called a *reciprocal lattice*, with primitive translation vectors $\vec{b}_1 \dots \vec{b}_d$. The relation between primitive translation vectors and reciprocal lattice vectors is $\vec{b}_1 = 2\pi(\vec{a}_2 \times \vec{a}_3) / [\vec{a}_1 \cdot (\vec{a}_2 \times \vec{a}_3)]$. Reciprocal vectors \vec{b}_2 and \vec{b}_3 can be obtained by cyclically permuting vectors \vec{a}_1 , \vec{a}_2 and \vec{a}_3 .

It was stated above that the average density given by Eq. 7.4 has a periodicity of a perfect crystal and that the crystal can be described by the set of reciprocal lattice vectors \vec{G} . Combining these two concepts and using Fourier transformation theory we can express the time-averaged mass density in a periodic solid represented by its Fourier components $\langle \rho_{\vec{G}} \rangle$ and reciprocal lattice vectors \vec{G}

$$\langle \rho(\vec{x}) \rangle = \rho_0 + \sum_{\vec{G}} \langle \rho_{(\vec{G})} \rangle e^{i\vec{G} \cdot \vec{x}} \quad (7.5)$$

or in terms of deviation of the density from the average density ρ_0 :

$$\langle \delta\rho(\vec{x}) \rangle \equiv \langle \rho(\vec{x}) \rangle - \rho_0 = \sum_{\vec{G}} \rho_{(\vec{G})} e^{i\vec{G} \cdot \vec{x}}. \quad (7.6)$$

Since $\langle \delta\rho(\vec{x}) \rangle$ is real $\rho_{(\vec{G})}^* = \rho_{(-\vec{G})}$ in order to make the density real.

7.1.2 Correlation Function

In this section we will explain *direct correlation functions*, which are later used to describe interaction between particles in a density field.

To describe correlation of density (i.e. particles) between two points, the two-point density-density correlation function is used. This function is an average of the product of the density at two different points \vec{x}_1 and \vec{x}_2 . The average is taken over different realizations of the material as its state fluctuates in time:

$$\rho^2(\vec{x}_1, \vec{x}_2) = \langle n(\vec{x}_1)n(\vec{x}_2) \rangle = \left\langle \sum_{\alpha, \alpha'} \delta(\vec{x}_1 - \vec{x}_\alpha) \delta(\vec{x}_2 - \vec{x}_{\alpha'}) \right\rangle. \quad (7.7)$$

For systems we will be considering, ρ^2 depends only on $\vec{x}_1 - \vec{x}_2$. For example, in a non-interacting system, $\rho^{(2)}$ becomes a product of averages of one-particle densities $\rho^{(2)}(\vec{x}_1, \vec{x}_2) = \rho(\vec{x}_1)\rho(\vec{x}_2)$ i.e. the probabilities of finding particles at x_1 and x_2 are uncorrelated.

The *total pair correlation function* gives a measure as to what extent (i.e. with what probability) a particle at x_1 correlates with a particle at x_2 .

$$h^2(\vec{x}_1, \vec{x}_2) = \frac{1}{\rho(\vec{x}_1)\rho(\vec{x}_2)} \left(\rho^{(2)}(\vec{x}_1, \vec{x}_2) - \rho(\vec{x}_1)\rho(\vec{x}_2) \right) \quad (7.8)$$

We can see that h^2 is zero for uncorrelated particles. For interacting particles, it measures correlations (i.e. interactions in a time-averaged statistical sense) with reference to a system of non-interacting particles. This is visualized on Fig.7.2, where we can see an atomic configuration in liquid. Let us draw two small circles with radius r and $r + dr$ around a randomly selected particle. Counting atoms with centers lying between these two circles, we would see that (statistically) there is a near-neighbor shell consisting of approximately six particles. We say that there is a short range correlation in the position of particles. Then, leaving this shell and drawing two slightly bigger circles, a dip in density will occur. Drawing another pair of circles further in will cause an increase of density, however, less atoms can be correlated with original particle.

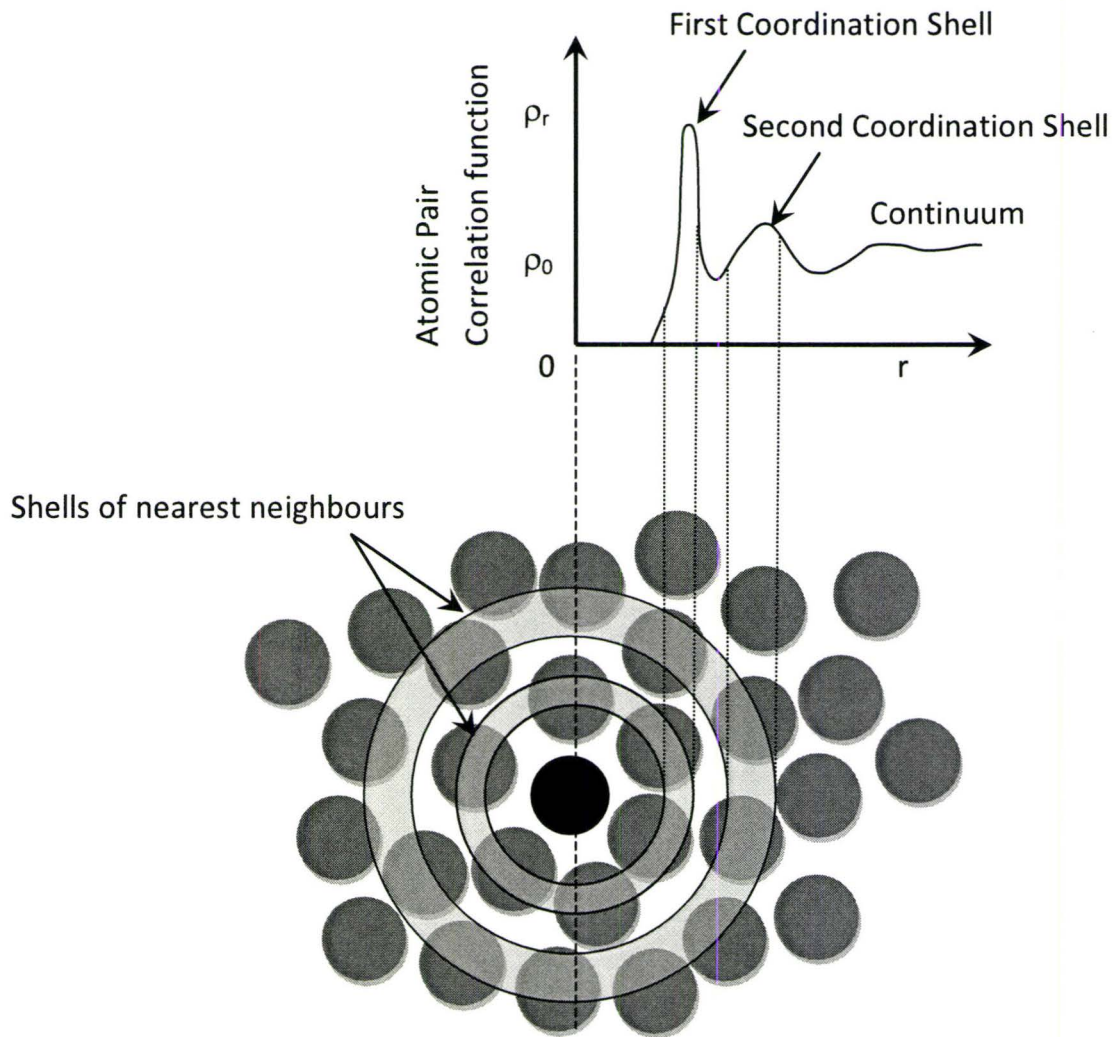


Figure 7.2: Representation of atomic configuration in a hard-sphere fluid (bottom). The pair correlation function can be obtained by choosing a particle as the origin and counting the number of atoms whose centers lie within a distance dr of a circle of radius r of the origin.

Finally, we consider the so-called direct correlation function between two particles, denoted $c^{(2)}(\vec{x}_1, \vec{x}_2)$, which can be obtained from MD simulations or from X-ray or neutron scattering experiments, and is related to h^2 as follows:

$$\hat{c}^2(\vec{x}) = \frac{1}{(2\pi)^3} \int d\vec{k} e^{i\vec{k}\cdot\vec{x}} \left(\frac{h^{(2)}(\vec{k})}{1 + \rho h^{(2)}(\vec{k})} \right) \quad (7.9)$$

A typical direct correlation function for Copper, found by MD simulation, is illustrated in frequency space in Fig. 7.3. Expanding $C(k)$ in a Taylor series around the

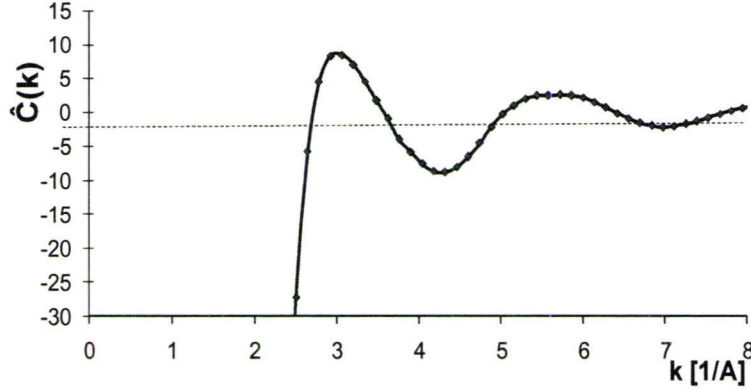


Figure 7.3: Direct correlation function for Cu [108].

peak wave vector gives a correlation function of the form

$$\hat{C} = \hat{C}_0 + \hat{C}_2 k^2 + \hat{C}_4 k^4 + \dots \quad (7.10)$$

(in real space this corresponds to a differential operator $C = (\hat{C}_0 - \hat{C}_2 \nabla^2 + \hat{C}_4 \nabla^4 - \dots) \delta(\vec{r} - \vec{r}')$, where the gradients are with respect to \vec{r}'). In this manner, the properties of the material are parameterized by the three variables, \hat{C}_0 , \hat{C}_2 and \hat{C}_4 . To fit the first peak in \hat{C} the variables \hat{C}_0 , \hat{C}_2 and \hat{C}_4 must be negative, positive and negative, respectively. These variables are related to three basic properties of the material; the liquid phase isothermal compressibility ($\sim (1 - \bar{\rho} \hat{C}_0)$), the bulk modulus of the crystal ($\sim \bar{\rho} \hat{C}_2 / |\hat{C}_4|$) and the lattice constant ($\sim (\hat{C}_2 / |\hat{C}_4|)^{1/2}$). In other words, the $k = 0$ term (i.e. that controlling correlations at the largest distances) is related to the

liquid phase isothermal compressibility, the height of the first peak is related to the bulk modulus of the crystalline phase, and the position of the first peak determines the lattice constant.

It is important to note that, at this level of simplification, the material is only defined by three quantities which may not be enough to fully parameterize any given material. For example, this simple three-parameter model always predicts triangular symmetry in two dimensions and BCC symmetry in three dimensions. Other crystal symmetries can be obtained by using more complicated 2-point correlation functions or by including higher order correlation functions defined below [75].

7.2 Density Functional Theory and Phase Field Crystal Models

In what follows we will introduce classical density functional theory (DFT) of nonuniform fluids. The theory was previously successfully applied to study liquid-solid and liquid-gas transition [20, 109, 110]. DFT gives rise to phase field crystal models, which are the main topic of this thesis.

In the density functional theory, an interacting system of particles is described by a functional of a field variable - the atomic number density, $\rho(\vec{r})$. As described in the previous section $\rho(\vec{r})$ is highly non-homogenous and possesses the crystal spatial symmetries in the solid while it remains constant in the liquid. This approach implicitly integrates out phonon modes ¹ in favour of a statistical view of the ordered phase that changes on diffusive time scales. In terms of $\rho(\vec{x})$, the free energy functional is written as

$$\begin{aligned} \mathcal{F}_c/k_B T &= \int d\vec{x} [\rho(\vec{r}) \ln (\rho(\vec{r})/\rho_l) - \delta\rho(\vec{r})] \\ &- \sum_{n=2}^{\infty} \frac{1}{n!} \int \prod_{i=1}^n d\vec{r}_i \delta\rho(\vec{r}_i) C_n(\vec{r}_1, \vec{r}_2, \vec{r}_3, \dots, \vec{r}_n), \end{aligned} \quad (7.11)$$

where \mathcal{F}_c is the free energy corresponding to the density $\rho(\vec{r})$ minus that at the constant density ρ_l , which is the liquid density at solid-liquid coexistence and serves

¹The fundamental quanta of lattice vibrations are called *phonons*, by analogy with the quanta of light (photons).

as a reference state for the expansion in Eq. 7.11. The C_n functions are n point direct correlation functions of an isotropic fluid described in a previous chapter. For example, C_2 is $c^{(2)}$ described above. C_3 describes correlations between particles 1 and 2 in the presence of interactions with a third particle.

To understand the basic features of this free energy functional, it is useful to expand the expression under both integrals in \mathcal{F} . Using the Taylor series expansion of the density $\rho(\vec{x})$ around ρ_l we expand the first part of the integral:

$$\rho \ln \frac{\rho}{\rho_l} = \frac{1}{\rho_l} \left(\frac{\rho - \rho_l}{\rho_l} + \frac{(\rho - \rho_l)^2}{2\rho_l^2} - \frac{(\rho - \rho_l)^3}{6\rho_l^3} + \frac{2(\rho - \rho_l)^4}{24\rho_l^4} \right), \quad (7.12)$$

The correlation terms are truncated to the second order, C_2 . This function is expanded according to the series expansion $C_2 = \hat{C}_0 + \hat{C}_2 k^2 + \hat{C}_4 k^4$, where k is a wave vector. In real space, this corresponds to an operator of the form $C = (C_o + C_1 \nabla^2 + C_2 \nabla^4) \delta(\vec{x} - \vec{x}')$. The free energy is then

$$\begin{aligned} \mathcal{F}/k_B T = \\ \int d\vec{r} \rho_l \left(\frac{\rho - \rho_l}{\rho_l} + \frac{(\rho - \rho_l)^2}{2\rho_l^2} - \frac{(\rho - \rho_l)^3}{6\rho_l^3} + \frac{2(\rho - \rho_l)^4}{24\rho_l^4} \right) - (\rho - \rho_l) - \\ \frac{\rho - \rho_l}{2} (C_0 - C_2 \nabla^2 + C_4 \nabla^4) (\rho - \rho_l). \end{aligned} \quad (7.13)$$

Using $\delta\rho \equiv \rho - \bar{\rho}_l$ and $n = \delta\rho/\rho_l$ (i.e. a normalized atomic density field) we obtain

$$\frac{\mathcal{F}}{k_B T \rho_l} = \int d\vec{r} \frac{n^2}{2} \underbrace{(1 - \rho_l C_0)}_{B^l} - \frac{n^3}{6} + \frac{n^4}{12} + \underbrace{\frac{\rho_l C_2^2}{4(-C_4)}}_{B^s} \left(2 \underbrace{\frac{2(-C_4)}{C_2}}_{R^2} \nabla^2 + \underbrace{\frac{4(-C_4)^2}{C_2^2}}_{R^4} \nabla^4 \right) \quad (7.14)$$

where B^s is the bulk modulus and B^l is the isothermal compressibility,

$$B^l - B^s = -\alpha(T_{melting} - T) \equiv -r. \quad (7.15)$$

After further manipulation we arrive at:

$$\frac{\mathcal{F}}{k_B T \rho_l} = \int d\vec{r} \left\{ \frac{n}{2} [(B^l - B^s) + B^s(1 + R^2 \nabla^2)^2] n - \frac{n^3}{6} + \frac{n^4}{12} \right\}, \quad (7.16)$$

Equation 7.16 can be directly related to the so-called Swift-Hohenberg equation used in polymer science to describe patterning in block co-polymers [15]. Equation 7.16 can be further simplified by the following rescalings: $\rho = n - 1/2$, $u = 1/3$, $B^l = a\Delta T + \lambda q_0^4 + 1/4$, $B^S = 4\lambda q_0^4$, $R = 1/\sqrt{(2q_0)}$, after which the free energy functional becomes

$$\mathcal{F} = \int d\vec{r} \left(\frac{\rho}{2} [a\Delta T + c(k_0^2 + \nabla^2)^2] \rho + u \frac{\rho^4}{4} \right). \quad (7.17)$$

The next section will analyze the properties of the free energy in Eq. 7.17.

7.3 Free Energy and the Equilibrium Phase Diagram of a Pure Material

Equation 7.17 derived in the previous section represents the simplest form of free energy \mathcal{F} that gives rise to periodic structures below a threshold temperature, represented in this model by the parameter ΔT . For convenience, it is useful to rewrite the free energy in dimensionless units:

$$\vec{x} = \vec{r}k_0, \quad \psi = \rho \sqrt{\frac{u}{ck_0^4}}, \quad r = \frac{a\Delta T}{ck_0^4}, \quad \tau = \Gamma\lambda k_0^6 t \quad \text{and} \quad \mathcal{F}_0 \equiv \frac{c^2 k_0^{8-d}}{u} \quad (7.18)$$

In dimensionless units free energy becomes:

$$F \equiv \frac{\mathcal{F}}{\mathcal{F}_0} = \int \left[\frac{\psi}{2} \omega(\nabla^2) \psi + \frac{\psi^4}{4} \right] dx dy, \quad (7.19)$$

where, $\omega(\nabla^2)\psi \equiv [r + (1 + \nabla^2)^2]\psi = \psi + r\psi + 2\nabla^2\psi + \nabla^4\psi$.

The free energy of the form in Eq. 7.19 gives rise to densities whose spatial structure corresponds to a solid with two dimensional hexagonal structure. By adjusting the parameters q_0 , λ , and u , we can set the inter-atomic distance and bulk modulus. To obtain different structures, such as a square lattice, the form of the correlation function C_2 in the previous section has to be changed.

Because the density $\langle \rho(\vec{x}) \rangle$ (or ψ in the dimensionless equation 7.19) is averaged over millions of atomic vibrations and over several atomic spacings, the fundamental time scale for changes in $\langle \rho(\vec{x}) \rangle$ is the diffusion time. At the atomic level, this time scale would correspond to the inverse of the vacancy-hopping frequency in the

crystal lattice. This is because the vacancy-hopping time sets the scale over which a continuous atomic probability density can be defined at each lattice site.

The time-averaged density $\langle \rho(\vec{x}) \rangle$ and the free energy represented by it (e.g. Eq. 7.19) formally describe a situation of local thermodynamic equilibrium in either the solid or liquid phases. As a result, dynamics that will be driven (see below) by free energy minimization – as in traditional phase field models – must necessarily represent evolution of diffusive time scales. In other words, in this formalism, dynamic density changes must occur so as to ensure a state of pseudo-equilibrium from the point of view of the free energy functional in Eq. 7.19.

7.3.1 Properties of the Free Energy in One Dimension

Typical representatives of the one-dimensional periodic system are crystals, liquid crystals, and block copolymers. Although the latter two are not primary targets of our investigation, it is useful to demonstrate properties of the periodic system on these simple examples. Let us demonstrate the properties of periodic systems arising from the simple free energy in Eq. 7.19, using spatially periodic density $\rho \approx A \sin(qx) + \rho_0$. Substitution of this function into Eq. 7.19 gives:

$$\begin{aligned} \frac{F^{str}}{L} \equiv \int_0^{\frac{2\pi}{q}} dx \left[\frac{\rho}{2} \omega (\nabla^2) \rho + \frac{\rho^4}{4} \right] &= \frac{\rho_0^2}{2} \left[\left(r + (1 - q^2)^2 \right) + \frac{3A^2}{2} + \frac{\rho_0^4}{2} \right] \\ &+ \frac{A^2}{4} \left[\left(r + (1 - q^2)^2 \right) + \frac{3A^2}{8} \right]. \end{aligned} \quad (7.20)$$

When Eq. 7.20 is minimized with respect to the structure parameters of wave vector q and amplitude A , the minimum free energy per unit length is then:

$$\frac{F^{str}}{L} = -\frac{r^2}{6} + \frac{\rho_0^2(1-r)}{2} - \frac{5\rho_0^2}{4} \quad (7.21)$$

i.e. the total free energy of a striped phase depends on the temperature (through r) and average density ρ_0 .

7.3.2 Properties of the Free Energy in Two Dimensions - Phase Diagram

To determine the properties of a two-dimensional periodic state, it is useful to take a so-called first mode approximation of the hexagonal density field. Using the same approach as mentioned in Eq. 7.6, we can describe this density field by:

$$\langle \delta\rho(\vec{r}) \rangle = \sum_{n,m} a_{n,m} \rho e^{i\vec{G}\cdot\vec{r}} + \rho_0, \quad (7.22)$$

where, $\vec{g} \equiv n\vec{b}_1 + m\vec{b}_2$ and the vectors \vec{b}_1 and \vec{b}_2 are reciprocal lattice vectors and, as mentioned previously, ρ_0 is the average system density. For a triangular lattice, the reciprocal lattice vectors can be written,

$$\vec{b}_1 = \frac{2\pi}{a\sqrt{3}/2} (\sqrt{3}/2\hat{x} + \hat{y}/2), \vec{b}_2 = \frac{2\pi}{a\sqrt{3}/2} \hat{y} \quad (7.23)$$

where a is the distance between the nearest neighbor local maxima of ρ and corresponds to the atomic positions. \hat{x} and \hat{y} are unit vectors. Since ρ is a real function the Fourier coefficients must satisfy following relationship $a_{n,m} = a_{-n,m} = a_{n,-m}$. The lowest order of approximation vector \vec{G} has a length of $2\pi/(a\sqrt{3}/2)$. This set of vectors includes $(n, m) = (\pm 1, 0), (0, \pm 1), (1, -1)$ and $(-1, 1)$. Considering both constraints we can write for coefficients a :

$$a_{\pm 1,0} = a_{0,\pm 1} = a_{1,-1} = a_{-1,1} \quad (7.24)$$

Using the above mentioned expressions, we can represent the two dimensional hexagonal solution for ρ by:

$$\rho_{hex} = A_{hex} \left[\cos(q_{hex}x) \cos\left(\frac{q_{hex}y}{\sqrt{3}}\right) - \frac{1}{2} \cos\left(\frac{2}{\sqrt{3}}q_{hex}y\right) \right] + \rho_0, \quad (7.25)$$

where A_{hex} is an unknown constant and $q_{hex} = 2\pi/a$. Substituting Eq. 7.25 into Eq. 7.19, minimizing with respect to A_{hex} and q_{hex} gives,

$$\frac{F^{hex}}{S} \equiv \int_0^{\frac{a}{2}} \frac{dx}{a/2} \int_0^{\frac{\sqrt{3}a}{2}} \frac{dy}{a\sqrt{3}/2} \left[\frac{\rho_{hex}}{2} \omega(\nabla^2) \rho_{hex} + \frac{\rho_{hex}^4}{4} \right] =$$

$$\begin{aligned}
 & -\frac{1}{10} \left(r^2 + \frac{13}{50} \rho_0^4 \right) + \frac{\rho_0^2}{2} \left(1 + \frac{7}{25} r \right) \\
 & + \frac{4\rho_0}{25} \sqrt{-15r - 36\rho_0^2} \left(\frac{4\rho_0^2}{5} + \frac{r}{3} \right), \tag{7.26}
 \end{aligned}$$

where

$$A_{hex} = \frac{4}{5} \left(\rho_0 + \frac{1}{3} \sqrt{-15r - 36\rho_0^2} \right) \tag{7.27}$$

$q_{hex} = \sqrt{3}/2$, and S is a unit area. To determine the phase diagram between a two-dimensional, hexagonally closed packed (HCP) crystal and its liquid, the energy for HCP Eq. 7.26 has to be compared to that of liquid state in which density is a constant i.e. $\rho_{liquid} = \rho_0$:

$$\frac{F_{min}^{liq}}{S} \equiv (1+r) \frac{\rho_0^2}{2} + \frac{\rho_0^4}{4} \tag{7.28}$$

To determine the phase diagram between striped phases (in polymer systems) and HCP phases we can compare F^{hex} (Eq. 7.26) to F^{liq} (Eq. 7.28) and striped state F^{str} (Eq. 7.21). Doing so the phase diagram in Fig. 7.4 can then be calculated from the free energy curves by the usual double-tangent construction, using the average density ρ_0 as the conserved quantity. The complete phase diagram consists of stable phase-fields of liquid, hexagonal and one dimensional periodic structures divided by coexistence regions between two phase systems. This phase diagram shows that we can simulate first order transition when liquid is undercooled into the area of solid hexagonal structure.

To make the phase diagram in Fig. 7.4 match that of a real material more precisely, a higher order expansion in correlation functions (i.e. interactions) and a more accurate reference for free energy would be required in Eq. 7.11. Moreover, the density expansion in Eq. 7.22 must incorporate higher order reciprocal lattice vectors. Nevertheless, as shown in Fig. 7.4, a small portion of the temperature-density plane of the phase diagram of our simplified model can be made – by suitable re-scaling – to match a portion of the argon phase diagram or any other phase diagram of a pure material. Thus, some of the generic features required to examine a first order transition are encapsulated in the original free energy in Eq. 7.11. As an example, we show the superposition of the portion phase diagram corresponding to Eq. 7.19 onto the argon phase diagram.

The derived phase diagram will be used below to obtain the initial conditions

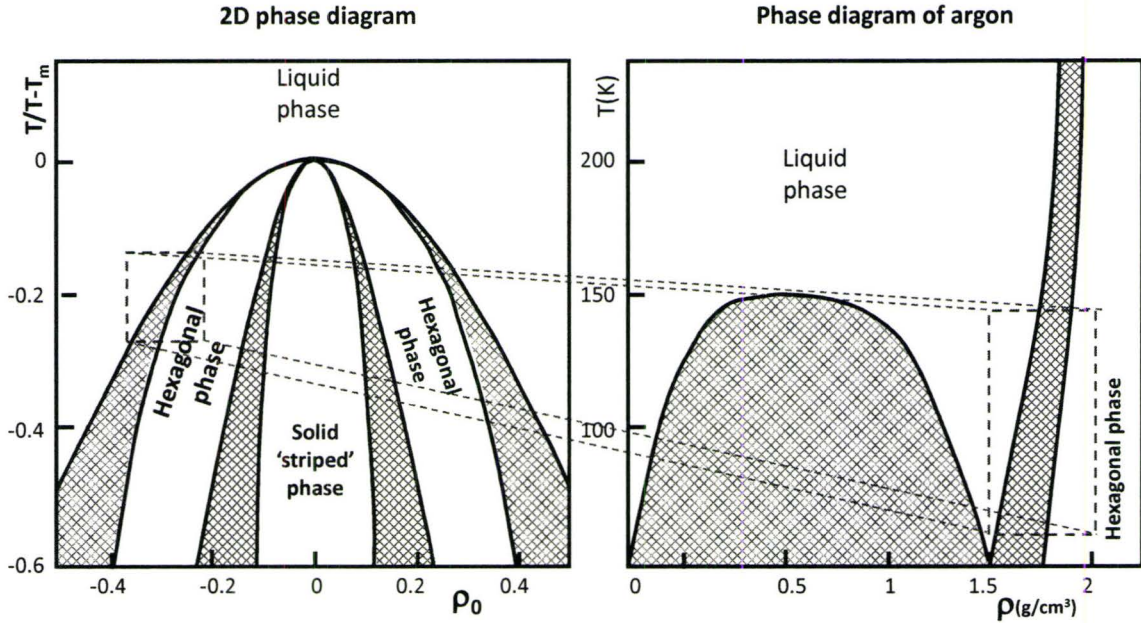


Figure 7.4: Two dimensional phase diagram corresponding to the free energy in Eq. 7.19(left). Hatched areas in the figure corresponds to coexistence region. The small region enclosed by a dashed box is superimposed on the argon phase diagram on the right.

for the crystalline structure with desired properties and orientations.

7.3.3 Elastic Properties

The elastic behaviour of periodic systems is of interest, because it allows us to simulate elastic – and later, plastic – deformations of crystalline materials. In the simplest case, consider a one dimensional structure with lattice parameter $a = 2\pi/q$. The free energy of the periodic or striped phase can be written by subtracting the minimum free energy Eq. 7.21 from the general form of free energy Eq. 7.20, which gives:

$$\frac{F^{str}}{a} - \frac{F^{str_{min}}}{a} = (K/2)(a - a_0)^2 \quad (7.29)$$

where $K = -8(r + 3\rho_0)/3$ is the bulk modulus and a_0 is the lattice constant that minimizes the free energy. In other words, this system automatically has an energy

that increases when the lattice constant deviates from the equilibrium or minimum value. Perhaps more importantly, it highlights the fact that the energy can be written in a Hooke's law form of $E = E_0 + (k\delta a)^2$. In higher dimensions, the elastic constants can be formally obtained by considering the deformation of the equilibrium (minimum free energy) state $\rho_{min}(\vec{r} + \vec{u})$, where \vec{u} is the displacement vector. Expanding to the lowest order in the strain tensor gives;

$$F = F_o + \int d\vec{r} (C_{ijkl} u_{ij} u_{kl} + \dots) \quad (7.30)$$

where $C_{ij,kl}$ are the elastic constants given by

$$C_{ij,kl} = \frac{1}{2!} \left. \frac{\partial^2 H}{\partial u_{ij} \partial u_{kl}} \right|_{eq} \quad (7.31)$$

In Eq. 7.30, the Einstein summation convention is used. Eq. 7.31 indicates that the elastic constants are related to the curvature of the free energy along the given strain directions. In addition, this result shows that the symmetry properties of C_{ijkl} are contained in H which is a function of equilibrium density field ρ_{eq} .

7.3.4 Diffusional Dynamics

The dynamics (i.e. density field changes) are assumed to be driven by minimization of F . These general ideas lead to the equation describing the relaxational dynamics:

$$\frac{\partial \phi}{\partial t} = \Gamma \nabla^2 \mu + \eta = \Gamma \nabla^2 \frac{\delta F}{\delta \phi} + \eta \quad (7.32)$$

where Γ is a phenomenological constant (relaxation time chosen to make set the time scale of changes of ρ), and η is a Gaussian stochastic field (noise) chosen to recover the correct equilibrium atomic fluctuation spectrum. Noise is important in the nucleation process of a new stable phase, but it contributes less during subsequent growth of the stable phase and is often neglected. The dimensionless equation of motion becomes,

$$\frac{\partial \phi}{\partial t} = \nabla^2 (\omega (\nabla^2) \rho + \rho^3) + \zeta, \quad (7.33)$$

where $\langle \zeta(\vec{r}_1, t_1) \zeta(\vec{r}_2, t_2) \rangle = \mathcal{D} \nabla^2 \delta(\vec{r}_1 - \vec{r}_2) \delta(\tau_1 - \tau_2)$ and $\mathcal{D} \equiv uk_B T q_0^{d-4} / c^2$. The notation $\langle \zeta(\vec{r}_1, t_1) \zeta(\vec{r}_2, t_2) \rangle$ implies that the random noise fluctuations are uncorrelated and individually distributed according to a gaussian distribution.

The model described by Eq. 7.33, or similar partial differential equations describing the evolution of a time-averaged atomic density field (through an appropriate free energy construction), was originally developed by Elder et. al. in 2002 [15] and has come to be known as the "phase field crystal" model, or PFC for short. In the next chapter, we will highlight some shortcomings of the model, in particular as it is applied to strain-induced phase transformations and nanocrystalline deformation. We will then introduce the first of our main contributions: a modification of the PFC model whose dynamics incorporate two time scales in order to rapidly relax strains without the need for simulating real phonons as in molecular dynamics. This will make it possible to emulate rapid relaxation processes on time scales such as those over which diffusion takes place.

Chapter 8

A New Phase Field Crystal Formalism: Incorporating Dynamic Elastic Interactions

The experimental work on mechanical properties of NC materials reviewed in chapter 3 revealed deformation processes ranging from atomic shuffling and sliding at the grain boundaries, to dislocation motion and pile up, to void nucleation and growth, or necking. These processes, summarized on Fig. 4.3, operate on length scales and time scales spanning several orders of magnitude. It was also discussed in section 3.2 that MD simulations are limited to the lower length scales ($\approx 10^{-9}m$) and time scales ($\approx 10^{-12}s$). This limitation is most severe when developing simulation models to study the physics and mechanics of nanostructured materials, where the relevant length scales are mesoscopic. Progress towards alleviating this limitation was made by the introduction of the phase field crystal model presented in the chapter 7.3. Unfortunately, as seen from Eq. 7.33, the original phase field crystal method evolves mass density only on diffusive time scales. In particular, it does not contain a mechanism for simulating elastic interactions. This precludes the study of phase transformation phenomena in the presence of complex mechanical deformations. While homogeneous deformations can be imposed through an affine transformation, this method is inapplicable in cases where nonhomogeneous stress distributions arise. As will be demonstrated below, these serious shortcomings of the original PFC model can be circumvented in a way that allows us to preserve the quintessential advan-

tage of the PFC model; namely, the ability to simulate atomic-scale interactions and dynamics on time scales that are many orders of magnitude longer than those of molecular dynamics. Most importantly, our modified model naturally incorporates instantaneous elastic interactions.

In this chapter, we introduce a *modified phase-field crystal* (MPFC) model that includes diffusive dynamics and elastic interactions. This is achieved by exploiting the separation of time scales that exist between diffusive dynamics and elastic relaxation processes in solids. In particular, the MPFC model is constructed to transmit long wavelength density fluctuations with wave modes that propagate up to a time scale t_w , after which the strain-relaxed density field continues to evolve according to diffusive dynamics. The key feature of our approach is that the value of t_w can be chosen to be much smaller than the characteristic time scale of diffusion, and much longer than $1/\omega_D \approx 10^{-13}$ s, where ω_D denotes the Debye frequency.

We proposed a modified phase field crystal model (MPFC) given by the following equation [19, 111]

$$\frac{\partial^2 \rho}{\partial t^2} + \beta \frac{\partial \rho}{\partial t} = \alpha^2 \nabla^2 \mu \quad (8.1)$$

where $\mu = \delta F[\rho; T]/\delta \rho$ is the chemical potential. The free energy F within this expression is the same as discussed in sections 7.2 and 7.3, and is given by Eq. 7.17. Parameters β and α are phenomenological constants, which are related to the effective sound speed and vacancy diffusion coefficient, as described in section 8.1 below. Equation 8.1 is of the form of a damped wave equation, containing two propagating density modes at early time and one diffusive mode at late times. The fast dynamics of the MPFC model are governed by the first term of Eq. 8.1, while the late time dynamics are governed by diffusional dynamics defined by Eq. 7.32.

In simple terms, the idea of this model is as follows: initially, perturbations in the atomic density will propagate their effect (i.e. strain through the crystal) very rapidly. This will be driven by the first term in Eq. 8.1. As these strain "waves" relax—due to the damping provided for in the equation—the equation turns itself into a diffusion equation exactly analogous to the original PFC model introduced in the last chapter. So long as perturbations in the strain relax faster than the time it takes for anything interesting to happen from diffusion, then the model is effectively emulating

rapid (ie. "instantaneous") elastic interactions.

The derivation of the equation Eq. 8.1 can be argued as follows; In addition to a continuum atomic density field a local effective continuum velocity field \vec{v} is defined. The combined evolution of ρ and \vec{v} are governed, respectively, by mass conservation,

$$\frac{\partial \rho}{\partial t} = -\nabla \cdot \rho \vec{v} \quad (8.2)$$

and momentum conservation

$$\frac{\partial(\rho v_i)}{\partial t} = -\nabla_j \sigma_{ij}^R + d_i = -\frac{\delta F}{\delta u_i} \quad (8.3)$$

where σ_{ij}^R represents the reactive part of a generalized stress tensor, and where d_i represents a generalized dissipation tensor. The second equality in the previous equation tacitly assumes that we can also express the free energy F in terms of the local displacements u_i of the density field. The dissipation tensor can take on various forms. The simplest one is to make it locally dependent on the local velocity. This form for the dissipative term arises quite naturally from the coupling between smooth elastic displacement fields and defect current in a more sophisticated and involved treatment that is explained in section 8.2.

8.1 Floquet Stability Analysis

Equation 8.1 is a nonlinear equation and cannot be solved analytically. To understand the behavior of this equation, we linearized the equation and performed a Floquet stability analysis. This analysis examines the way a perturbation propagates in the linearized version of Eq. 8.1, assuming a perturbation in the density of the form

$$\rho_p = \rho_{eq} + \delta\rho, \quad (8.4)$$

where

$$\rho_{eq} = \rho_o + \sum_{n,m} a_{n,m} e^{i\vec{G}_{n,m} \cdot \vec{r}}$$

$$\delta\rho = \sum_{n,m} b_{n,m}(t)e^{i\vec{G}_{n,m}\cdot\vec{r}+i\vec{Q}\cdot\vec{r}}, \quad (8.5)$$

with ρ_o the average density, $\vec{G}_{n,m} = n\hat{x} + (n+2m)/\sqrt{3}\hat{y}$ the triangular reciprocal lattice vectors, and $a_{n,m}$ their corresponding amplitudes.

The vector \vec{Q} is a perturbation wave vector and $b_{n,m}(t)$ is the perturbation amplitude associated with the perturbation of the steady state mode (m, n) . To get a linear form of Eq. 8.1 we substitute Eq. 8.4 into Eq. 8.1 and expand it to a linear order. We will study only the mode with the fastest growth rate, equal to $m = n = 0$,

$$\frac{d^2b_{00}}{dt^2} + \beta\frac{db_{00}}{dt} = -\alpha Q^2 \left\{ 3\rho_o^2 + r + (q_o^2 - Q^2)^2 + \frac{9}{8}A_{min} \right\} b_{00} \quad (8.6)$$

Equation 8.6 determines us how the perturbation will grow, decay or travel. The leading order mode satisfies $b_{0,0} \sim e^{i\omega t}$ with the dispersion relation

$$\omega(Q) = i\frac{\beta}{2} \pm \frac{\Lambda(Q)}{2}, \quad (8.7)$$

where

$$\Lambda(Q) = \sqrt{-\beta^2 + 4\alpha^2 Q^2 \left[3\rho_o^2 + r + (Q^2 - q_o^2)^2 + \frac{9}{8}A_{min}^2 \right]}. \quad (8.8)$$

Here, A_{min} is the equivalent of Eq. 7.27

$$A_{min} = \frac{4}{5} \left(\rho_o + \frac{1}{3} \sqrt{-15r - 36\rho_o^2} \right) \quad (8.9)$$

and denotes the amplitude of ρ_{eq} within a single-mode approximation [15].

Note that when $4\alpha^2 Q^2 [3\rho_o^2 + r + \lambda(Q^2 - q_o^2)^2 + 9/8A_{min}^2] \gg \beta^2$ (i.e. when $Q \rightarrow 0$, which implies long wavelength perturbations), the dispersion is approximately

$$\omega(Q) \approx i\frac{\beta}{2} \pm 2\alpha Q \sqrt{3\rho_o^2 + r + (Q^2 - q_o^2)^2 + \frac{9}{8}A_{min}^2} \equiv i\frac{\beta}{2} \pm v_{eff}Q. \quad (8.10)$$

This dispersion describes a pair of density waves that propagate undamped for time $t_w \approx 2\beta^{-1}$ and distance $\bar{L} \sim v_{eff}t_w = 4\alpha\sqrt{3\rho_o^2 + r + q_o^4 + 9/8A_{min}^2}/\beta$, after which they become effectively diffusive as in Ref. [16], with an effective vacancy diffusion

coefficient

$$D = \alpha^2 \frac{3\rho_o^2 + r + q_o^4 + \frac{9}{8}A_{min}^2}{\beta}. \quad (8.11)$$

The above analysis demonstrates that Eq. 8.1 admits propagating solutions for density disturbances with a tunable elastic interaction length \bar{L} and a tunable elastic interaction time on the order of t_{eff} . As an illustration, let $L^* = \max[L_x, L_y]$ denote the largest dimension of the system under consideration and $\Delta \equiv (3\rho_o^2 + r + q_o^4 + 9/8A_{min}^2)$. Since $D = \alpha^2\Delta/\beta$, $\bar{L} \approx 4\alpha\sqrt{\Delta}/\beta$ and we require

$$\bar{L} = \frac{4D}{\alpha\sqrt{\Delta}} \geq L^*, \quad (8.12)$$

this implies

$$\alpha \leq \frac{4D}{L^*\sqrt{\Delta}}. \quad (8.13)$$

After choosing the appropriate value for α , β is determined from

$$\beta = \frac{\alpha^2\Delta}{D}. \quad (8.14)$$

For example, to simulate a system with $D \approx 10^{-18}m^2/s$ and $\bar{L} \approx 10^{-7}m$, one would choose $\alpha = 4 \times 10^{-11}m/s$ for the effective speed of sound and $\beta = 1.6 \times 10^{-3}s^{-1}$. Contrast this with MD simulations where $\alpha \sim 10^3m/s$.

8.2 Comparison with Hydrodynamics of Isothermal Solids

Majaniemi et al. [21] derived generalized hydrodynamics for solids, partly with the aim of expanding on the nature and origins of Eq. 8.1.

Their model uses density-functional theory based free energy and a Poisson Bracket formalism, which allows them to consider nonlinearities in density, momentum density and elastic fields¹. As a result, a set of three equations of motion was

¹This is a method that treats the atomic density as a continuum –as do we– and combines it

obtained:

$$\begin{aligned}
 \partial_t \rho &= -\nabla \cdot \vec{g}; \\
 \partial_t \vec{g} &= \hat{L}\vec{g} + \hat{K}\vec{u} - \rho \nabla \mu(\rho); \\
 \partial_t \vec{u} &= \frac{1}{\rho_0} \vec{g} + \hat{A}\hat{K}\vec{u};
 \end{aligned} \tag{8.15}$$

Where $\rho(\vec{r}, t)$ is the mass density, $\vec{g}(\vec{r}, t)$ is the momentum, $\vec{u}(\mathbf{r}, t)$ is the displacement field and $\mu[\rho]$ is the chemical potential, which depends on the local atomic density. Dissipative effects of the phonon current are described by the constant tensor $\hat{A}_{ij} = a\delta_{ij}$ and those of the momentum flow are given through $(\hat{L}\vec{g})_i \equiv \hat{L}_{ij}g_j$ where $\hat{L}_{ij} \equiv \nu_1\partial_i\partial_j + \nu_2\delta_{ij}\nabla^2$ with the shear and bulk viscosities given by ν_1 and ν_2 . The elastic operator $(\hat{K}\vec{u})_i \equiv \hat{K}_{ij}u_j$ where $\hat{K}_{ij} \equiv \lambda_1\partial_i\partial_j + \lambda_2\delta_{ij}\nabla^2$ with the shear and bulk moduli λ_1 , and λ_2 , and finally $\lambda \equiv \lambda_1 + \lambda_2$, $\nu \equiv \nu_1 + \nu_2$. Equations 8.15 were written in terms of the Fourier-Laplace transformations of the density and displacement. The dynamics of the density and displacement fields were separated into a contribution moving transversely and parallel (longitudinally) to a particular wave vector \vec{k} . For example, to linear order, the longitudinal disturbance of the density and displacement vector $\vec{x}(k, s)$ follows the relation $A_L\vec{x} = \vec{\bar{x}}$, where

$$A_L(k, s) = \begin{pmatrix} s & s + c_1k^2 \\ s^2 + \nu k^2s + d_2k^2 & c_3k^2 \end{pmatrix}, \tag{8.16}$$

where $k = |\vec{k}|$, $c_1 \equiv a\lambda$, $c_3 = \lambda/\bar{\rho}_0$ and $d_2 = (1+r) + 3\rho_0^2 + (9/8)\bar{A}^2$.

The model operates on one fast timescale, propagating sound waves and two slow timescales, for diffusive phenomena. In the longitudinal direction, Majaniemi et. al obtained a sound velocity $v_s = \sqrt{c_3 + d_2}$; diffusion constant $D = c_1d_2/(c_3 + d_2)$ and sound attenuation coefficient $\Gamma = (c_1 + \nu - D)/2$ while transversal modes consisting of a pair of sound waves: $\tilde{s}_{\pm} = \pm i\tilde{v}_s|k| - \tilde{\Gamma}k^2$. The transversal sound velocity $\tilde{v}_s = \sqrt{\lambda_1/\rho_0}$ and attenuation $\Gamma = (c_1 + \nu_1)/2$.

The authors compared the structure factor $S(\mathbf{k}, t)$ from our model (Eq. 8.1)

with a momentum and displacement field. The dynamics of these fields are then determined from the variation of a Hamiltonian-like energy, written in terms of these fields. The formalism parallels that of classical mechanics whereby the evolution of discrete particle positions and their momenta are determined by the variation of a classical hamiltonian energy [112].

to an analytical prediction from their own Eqs.8.15 and found good agreement for wavelengths satisfying

$$c_3/c_1^2 \ll k^2 \ll c_3/(vc_1); w \ll c_1k^2. \quad (8.17)$$

The analysis of Majaniemi et. al. implies that the simplified MPFC model we proposed follows the correct approach to elastic relaxation on time scales many times longer than those on which real phonons propagate and on length scales many times greater than the scale of the atom (i.e. the smallest physically resolvable feature in our model). Indeed, to make this point clear, the apparent wave modes propagated by our model have been coined "quasi-phonons" to make the distinction from real phonons clear.

8.3 The Diffusive Limit of the Model: Polycrystalline Nucleation and Growth

Equation 8.1 can describe several physical phenomena depending on the initial conditions, which can be prepared with the help of the phase diagram displayed on Fig.7.4. As mentioned above, we would like to use this model to study deformation processes in crystalline materials. In order to do so, we would like to nucleate and grow crystals separated by grain boundaries, including defects and other structural elements. One way to achieve such a structure is through heterogeneous nucleation from a supercooled liquid. From the phase diagram, we chose values for density and temperature that lay in a hexagonal region - average dimensionless density $\rho_0 = 0.29$ and r (representation of normalized temperature) equals $-1/4$. Eq. 8.1 was numerically solved on a discretized uniform grid of system size $512\Delta x \times 512\Delta x$ where grid spacing Δx was chosen as $\pi/4$. Parameters α and β were chosen to be equal 1. In order to start the heterogeneous nucleation process, gaussian fluctuations with amplitude 0.01 were introduced into the liquid density field with initially constant average density of ρ_0 . The positions of the fluctuation defined the position of a later nucleus. As a result of randomness in initial conditions, the evolving crystallites have a different orientation. After the initial growth stage, crystallites impinge and form low and high angle grain boundaries (Fig. 8.1). During solidification, we found

that the effect of the first term in Eq. 8.1 was negligible, and the growth rates and morphology were essentially indistinguishable from those described by Eq. 7.33. In other words, solidification was essentially controlled by diffusive dynamics, which is no surprise.

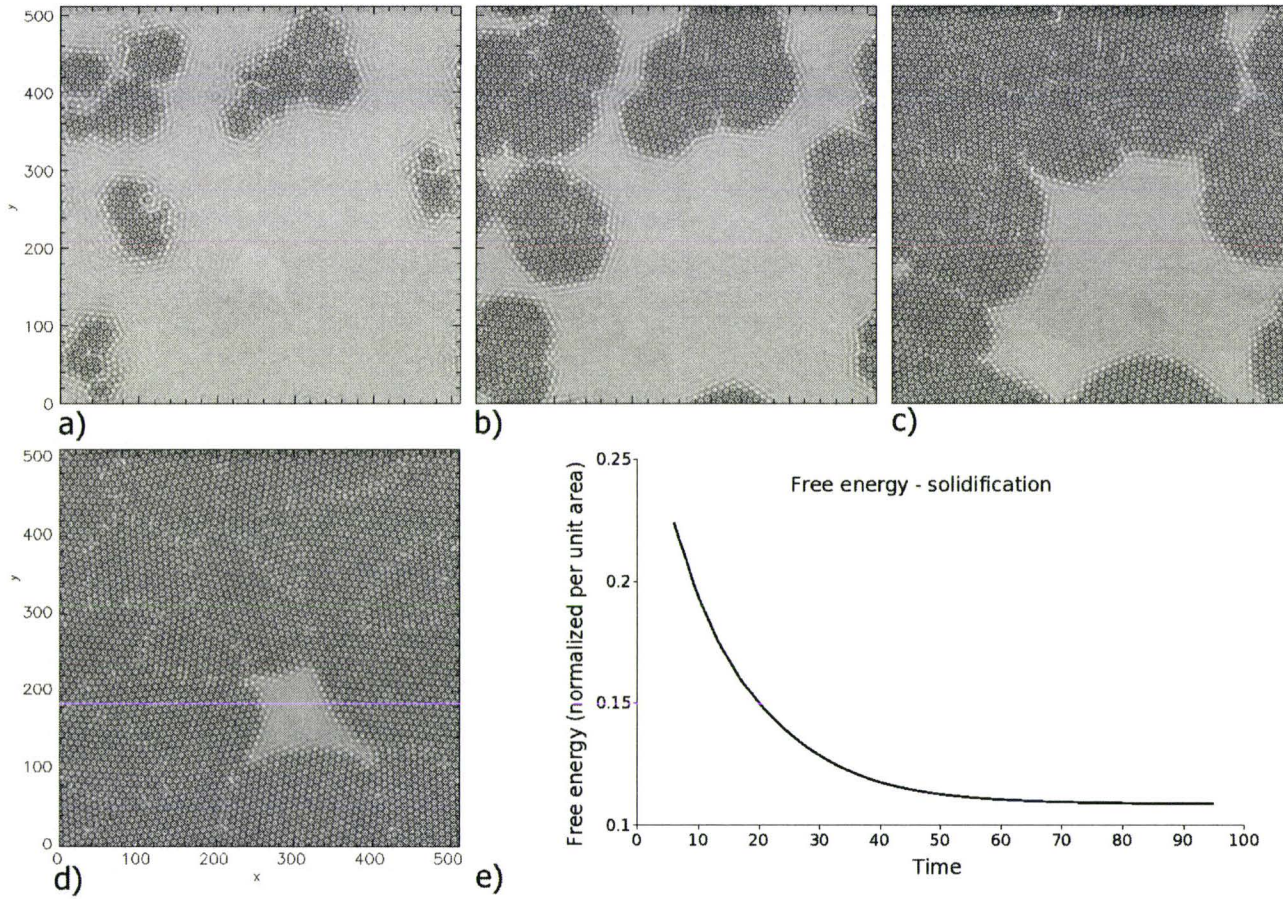


Figure 8.1: Simulation of heterogeneous nucleation and growth using MPFC. As time evolved several crystal seeds nucleated and grew to fill the cell. a) $t=10$, b) $t=20$, c) $t=30$, d) $t=40$. e) Plot of free energy during heterogeneous nucleation. Free energy approaches minimum with an increasing fraction of solid.

8.4 Grain Boundary Interactions

As we showed in the previous section, after the solidification of crystallites the grain boundaries will form. In two dimensions, we can consider a *tilt boundary* that will arise when one grain is rotated by a rotation angle θ . If the change of crystal orientation across the boundary is small (less than 10°) the entire boundary can be regarded as a line containing a regular array of dislocations. There is a relation between the length of Burgers vector b (or dislocation core size), the spacing between dislocations d , and the orientation angle θ . For small angles this relation is $\theta = b/d$ (Fig.8.2).

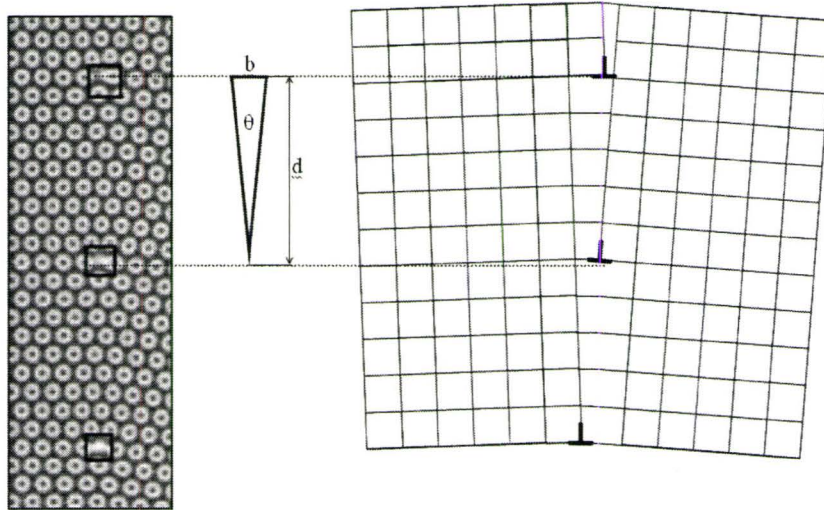


Figure 8.2: **Left:** Portion of tilted GB with $\theta = 6.4^\circ$. **Right:** A simple small-angle boundary formed from edge dislocations. Adapted from [113]

In large-angle types of boundaries (more than 10°), dislocations lie so close together that it is difficult to distinguish one from another. Such an arrangement of dislocations creates a disordered monolayer of material between the grains.

For the total energy/length in two dimensions, Read-Shockley derived the following equation:

$$\frac{F}{L} = \frac{bY_2}{8\pi d} \left[\frac{3}{2} - \ln \left(\frac{2\pi a}{d} \right) \right] \quad (8.18)$$

To examine the validity of Eq. 8.18, the grain boundary energy was measured as a function of angle. Parameters of the simulations were set to $(r, \rho_0, \Delta x, \Delta t, \alpha, \beta) =$

$(-0.2, 0.25, \pi/4, 0.001, 1, 1)$. The initial conditions were set for a different orientation of angles and the system was evolved for 100,000 time steps. The increase in the free energy due to the increase of misorientation angle was plotted against the angle θ . We found a good agreement with the numerical simulation and with Eq. 8.18 for small angles (Fig. 8.3 left). For higher angles, we had to adjust parameter Y_2 to fit the experimental results with Shockley formula (Fig. 8.3 right). Free energy is symmetric around the 30° point.

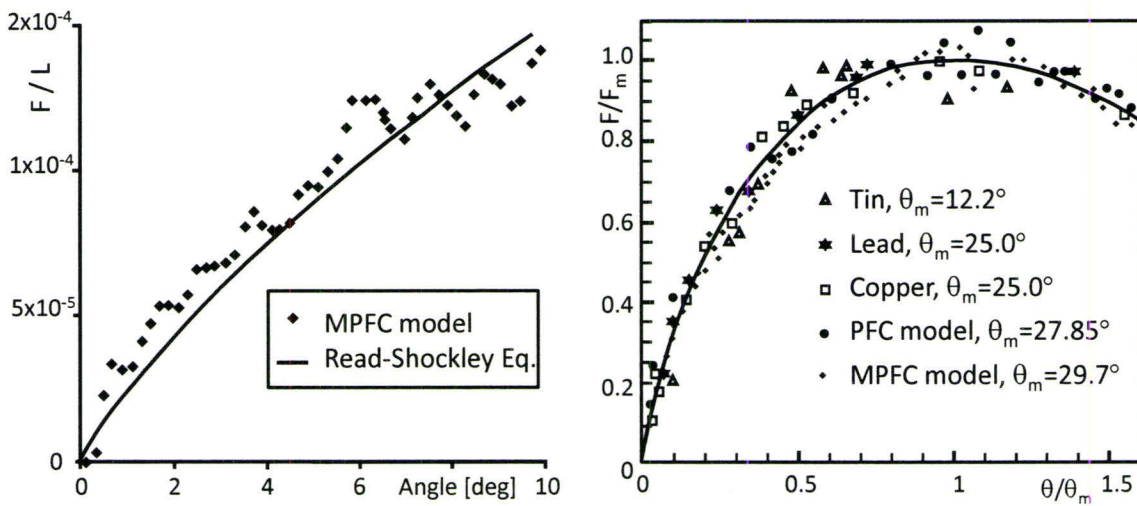


Figure 8.3: The GB energy plotted as a function of mismatch angle. The solid line corresponds to Shockley calculations. The measurements agree with theory for small angles (left). Comparison with experimental results and PFC model (right).

8.5 Elastic Strain Relaxation Properties of the Model

A tensile load applied to a semi-infinite continuum elastic bar can be theoretically modeled as an array of coupled masses and springs along the x-axis (Fig. 8.4). If the row of atoms is pulled with a displacement D_1 to the left, a tensile stress wave will propagate to the right. When atomic oscillations stop, a linear displacement distribution will be established along the bar, which, according to Hooke's law, will have a slope given by the applied load P , elastic constant E and the cross sectional area of the bar A

$$D_{(x)} = \frac{P}{EA} L_{(x)}. \quad (8.19)$$

To demonstrate the presence of elastic relaxation modes in the MPFC model Eq. 8.1,

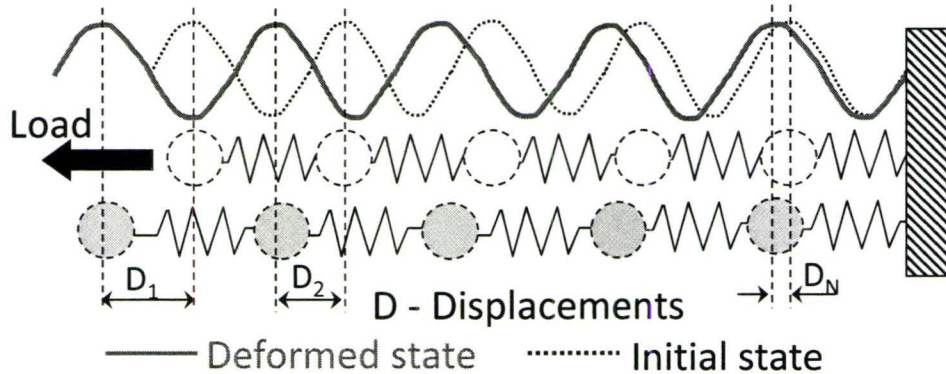


Figure 8.4: Atoms connected by strings. Masses and spring constants are the same.

we performed simulations of an effectively one-dimensional single-crystal specimen under uniaxial tension. The system was prepared in the coexistence region as given by the phase diagram, and the solid sample was surrounded by liquid. Model parameters used were $(r, \rho_0, \Delta x, \Delta t, \alpha, \beta) = (-0.4, 0.31, \pi/8, 0.001, 15, 0.9)$. Taking $a = 5\text{\AA}$, this combination of parameters implies that $D \approx 5 \times 10^{-17} m^2/s$ and $\bar{L} \approx 3.3 \times 10^{-8} m$. When an atom at the boundary is displaced by an amount D_1 to the left, a tensile stress wave will propagate to the right. When atomic oscillations stop, a linear displacement distribution, $D(x) = D_1 x/L$, will be established along the bar. Plots of displacement vs. position in the case of constant strain rate applied to the boundary atom are shown in Fig. 8.5 at three different times. Here, the displacements were

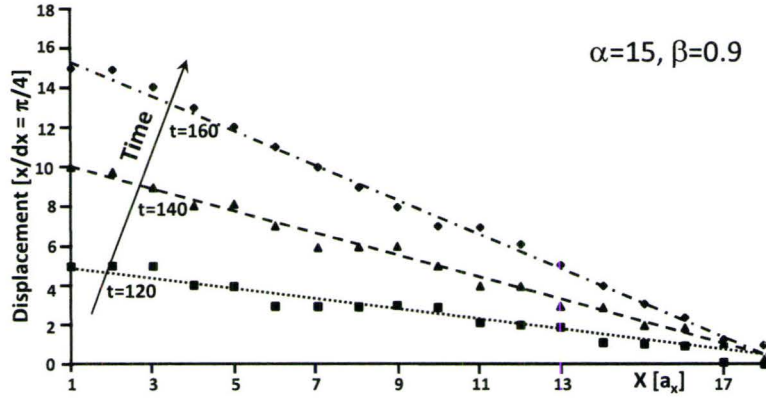


Figure 8.5: The displacements along a one-dimensional sample in simple uniaxial tension at three different times. Linear profiles are consistent with linear elasticity theory. Strain rate $\dot{\epsilon} = 6.5 \times 10^{-4}$.

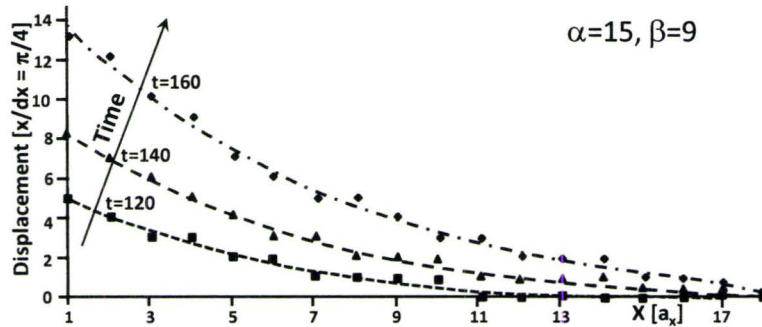


Figure 8.6: The displacements along a one-dimensional sample in simple uniaxial tension at three different times after a ten-fold increase in β when compared with Fig. 8.5. Non-linear profiles suggest visco-elastic behavior. Strain rate $\dot{\epsilon} = 6.5 \times 10^{-4}$.

extracted by a peak tracking method, where the locations of local maxima in ρ were tabulated after each time step. The data clearly shows that the response of the system is consistent with elasticity theory. To make contact with the previous PFC formulation in Eq. 7.32, we repeated the same simulations with a ten-fold increase in the damping parameter $\beta = 9$, which corresponds to $D \approx 5 \times 10^{-18} m^2/s$ and $\bar{L} \approx 3.3 \times 10^{-9} m$. The computed displacements, plotted in Fig. 8.6, show that the response becomes viscoelastic as damping is increased. Therefore, Eq. 7.32 alone does not adequately describe elastic responses in strained crystals at finite strain rates, while Eq. 8.1 naturally incorporates such phenomena. Indeed, this feature of

our approach opens a new computational window into studies of complex geometries and non-uniform stresses which are discussed in part of this thesis .

Chapter 9

Extension to Binary Alloys

In chapter 7, we described a new extension to phase field modeling known as the *phase field crystal* method (PFC). The methodology described the evolution of the atomic density of a system according to dynamics driven by free energy (Eq. 7.11) and minimization (Eq. 7.32). In the PFC approach, the free energy functional of a solid phase was minimized when the density field is periodic (section 7.3.2). As discussed in the prior section 7.3, the periodic nature of the density field naturally gives rise to elastic effects, multiple crystal orientations, and the nucleation and motion of dislocations. However, all the applications mentioned previously were related to a single component system. The original PFC model (Eq.7.32) is among the simplest mathematical descriptions that can self-consistently combine the physics of atomic-scale elasto-plasticity with the diffusive dynamics of phase transformations and microstructure formation. Nevertheless, to be able to study more complex problems, further work was required to fully exploit the methodology. In chapter 8, we introduced a new innovation for simulation of *rapid* elastic relaxations. This extension proved important for modeling deformations in complex shapes. The purpose of this chapter is to further exploit the link between DFT and PFC (or MPFC) made in section 7.2 (or chapter 9) and to study non-equilibrium microstructure formation, such as spinodal decomposition and solidification in binary alloys.

In what follows, a simple binary alloy free energy is derived. This is done in order to provide a mathematically simple model that can transparently illustrate the use of the PFC formalism in simultaneously modeling diverse processes such as solidification, grain growth, defect nucleation, phase segregation, and elastic and

plastic deformation. This section also shows that the free energy of the simplified alloy PFC model reproduces two common phase diagrams associated with typical binary alloys in materials science. Some of the more tedious calculations in the derivation of the simplified model are shown in the Appendix (Section B).

In section 9.6, dynamical equations of motion that govern the evolution of the solute concentration and density field of the binary alloy are derived.

9.1 Free Energy Functional for a Binary Alloy

In this section, the free energy functional of a binary system is presented as it is derived from the classical density functional theory of freezing. In section 7.2 we introduced free energy for a single component system. Let us repeat Eq. 7.11 below:

$$\frac{\mathcal{F}_c}{k_B T} = \int d\vec{x} \left[\rho(\vec{r}) \ln \left(\frac{\rho(\vec{r})}{\rho_l} \right) - \delta\rho(\vec{r}) \right] - \sum_{n=2}^{\infty} \frac{1}{n!} \int \prod_{i=1}^n d\vec{r}_i \delta\rho(\vec{r}_i) C_n(\vec{r}_1, \vec{r}_2, \dots, \vec{r}_n).$$

In contrast to the single component model, describing the binary alloy system requires two interwoven density fields ρ_A and ρ_B , to describe the A and B species. Similarly, the average reference density or density of liquid will become ρ_A^l for A atoms and ρ_B^l for B atoms. Furthermore the direct correlation function now has to describe the correlations between atoms of the same species C^{AA} , C^{BB} and their combination C^{AB} . Taking the above into consideration, the free energy functional for a binary alloy made up of A and B atoms can be written to the lowest order in terms of the direct correlation functions as:

$$\begin{aligned} \frac{\mathcal{F}}{k_B T} = & \int d\vec{r} \left[\rho_A \ln \left(\frac{\rho_A}{\rho_A^l} \right) - \delta\rho_A + \rho_B \ln \left(\frac{\rho_B}{\rho_B^l} \right) - \delta\rho_B \right] \\ & - \frac{1}{2} \int d\vec{r}_1 d\vec{r}_2 \left[\delta\rho_A(\vec{r}_1) C^{AA}(\vec{r}_1, \vec{r}_2) \delta\rho_A(\vec{r}_2) \right. \\ & \quad \left. + \delta\rho_B(\vec{r}_1) C^{BB}(\vec{r}_1, \vec{r}_2) \delta\rho_B(\vec{r}_2) \right. \\ & \quad \left. + 2 \delta\rho_A(\vec{r}_1) C^{AB}(\vec{r}_1, \vec{r}_2) \delta\rho_B(\vec{r}_2) \right] \end{aligned} \quad (9.1)$$

where $\delta\rho_A \equiv \rho_A - \rho_A^l$ and $\delta\rho_B \equiv \rho_B - \rho_B^l$ are the deviations of densities from their average reference value, taken at solid-liquid co-existence. In order to make a connection between the alloy free energy and standard phase field models it is useful to

define the total number density,

$$\rho \equiv \rho_A + \rho_B \quad (9.2)$$

and a local concentration field

$$c \equiv \rho_A/\rho. \quad (9.3)$$

In terms of these fields the atomic densities can be written as:

$$\rho_A = c\rho \quad (9.4)$$

and

$$\rho_B = \rho(1 - c). \quad (9.5)$$

Furthermore it is useful to define

$$\rho = \rho_l + \delta\rho \quad (9.6)$$

where $\rho_l \equiv \rho_l^A + \rho_l^B$ and $\delta c = 1/2 - c$. Substituting these definitions into Eq. (9.1) gives (using Maple),

$$\begin{aligned} \frac{\mathcal{F}}{k_B T} = & \int d\vec{r} \left[\rho \ln(\rho/\rho_\ell) - \delta\rho + \beta\delta c + F_o \right. \\ & - \frac{1}{2} \delta\rho \{ c C^{AA} + (1 - c) C^{BB} \} \delta\rho \\ & + \rho \{ c \ln(c) + (1 - c) \ln(1 - c) \} \\ & \left. + \rho c \{ (C^{AA} + C^{BB})/2 - C^{AB} \} (1 - c) \rho \right] \end{aligned} \quad (9.7)$$

where

$$\beta \equiv \rho_l (C^{AA} - C^{BB}) (\rho + \rho_l) / 2 + \rho \ln(\rho_\ell^B / \rho_\ell^A) \quad (9.8)$$

and

$$F_o \equiv \bar{\rho} \ln \left(\frac{\rho_\ell}{(\rho_\ell^A \rho_\ell^B)^{1/2}} \right) - \frac{C^{AA}}{2} \left((\rho_\ell^A)^2 + \frac{\rho_l}{2} (\rho_l + \bar{\rho}) \right) - \frac{C^{BB}}{2} \left((\rho_\ell^B)^2 + \frac{\rho_l}{2} (\rho_l + \bar{\rho}) \right) \quad (9.9)$$

To illustrate the properties of the alloy free energy in Eq. 9.7, it is useful to consider two limiting cases; a liquid phase at constant density and a crystalline phase at constant concentration. These calculations are presented in sections 9.2 and 9.3, respectively.

9.2 Liquid Phase Properties

In the liquid phase, ρ is constant on average and in the mean field limit can be replaced by $\rho = \bar{\rho}$. To simplify calculations, the case $\rho = \bar{\rho} \approx \rho_\ell$ (or $\delta\rho \approx 0$) will now be considered. As in the previous section 7.2, it is useful to expand the direct correlation functions of each species in Fourier space –where they each will exhibit a peak– in a Taylor series in the wave vector magnitude $k = |\vec{k}|$,

$$\hat{C}^{ij} = \hat{C}_0^{ij} + \hat{C}_2^{ij} k^2 + \hat{C}_4^{ij} k^4 + \dots \quad (9.10)$$

where the subscript i and j refer to a particular element. Substituting the real-space counterpart of the Fourier expansion for \hat{C}^{ij} (to order k^2) into Eq. 9.7 gives,

$$\begin{aligned} \frac{\mathcal{F}_C}{\bar{\rho} k_B T} &= \int d\vec{r} \left[c \ln(c) + (1-c) \ln(1-c) \right. \\ &\quad \left. + \frac{\bar{\rho} \Delta \hat{C}_0}{2} c(1-c) + \gamma^\ell \delta c + \frac{\bar{\rho} \Delta \hat{C}_2}{2} |\nabla c|^2 \right], \end{aligned} \quad (9.11)$$

where \mathcal{F}_C is the total free energy minus a constant that depends only on $\bar{\rho}$, ρ_A^l and ρ_B^l ,

$$\gamma^\ell \equiv (B_\ell^{BB} - B_\ell^{AA}) + \bar{\rho} \ln \left(\rho_\ell^B / \rho_\ell^A \right), \quad (9.12)$$

$$\Delta \hat{C}_n \equiv \hat{C}_n^{AA} + \hat{C}_n^{BB} - 2\hat{C}_n^{AB}. \quad (9.13)$$

and $B_\ell^{ij} = 1 - \bar{\rho} \hat{C}_0^{ij}$ is the dimensionless bulk compressibility. Equation 9.11 derives the regular solution model used in solution thermodynamics from the atomistic scale using the principles of classical density functional theory.

The coefficient of $c(1 - c)$ in Eq. 9.11 is given by

$$\bar{\rho}\Delta\hat{C}_0 = 2B_\ell^{AB} - B_\ell^{AA} - B_\ell^{BB}. \quad (9.14)$$

This result shows that in the liquid state the 'interaction' energies that enter regular solution free energies are simply the compressibilities (or the elastic energy) associated with the atomic species. The γ^ℓ term is also quite interesting as it is responsible for asymmetries in the phase diagram. Thus Eq. 9.12 implies that asymmetries can arise from either different compressibilities or different densities.

Expanding Eq. 9.11 around $c = 1/2$ gives,

$$\frac{\Delta\mathcal{F}_C}{\bar{\rho}k_B T} = \int d\vec{r} \left[\frac{r^\ell}{2} \delta c^2 + \frac{u}{4} \delta c^4 + \gamma^\ell \delta c + \frac{K}{2} |\nabla c|^2 \right] \quad (9.15)$$

where, $\Delta\mathcal{F}_C \equiv \mathcal{F}_C - \bar{\rho}k_B T \int d\vec{r} (\bar{\rho}\Delta\hat{C}_0/8 - \ln(2))$, $u \equiv 16/3$, $r^\ell \equiv (4 - \bar{\rho}\Delta\hat{C}_0)$ and $K = \bar{\rho}\Delta\hat{C}_2$. The parameter r^ℓ is related only to the $k = 0$ part of the two-point correlation function and can be written,

$$r^\ell = 4 + (B_\ell^{AA} + B_\ell^{BB} - 2B_\ell^{AB}). \quad (9.16)$$

This result implies that the instability to phase segregation in the fluid is a competition between entropy (4) and the elastic energy of a mixed fluid ($2B_\ell^{AB}$) with the elastic energy associated with a phase separated fluid ($B_\ell^{AA} + B_\ell^{BB}$). Replacing the dimensionless bulk moduli with the dimensional version (i.e., $B = \kappa/k_B T$), gives the critical point (i.e. $r^\ell = 0$) as

$$T_C^\ell = (2\kappa_{AB} - \kappa_{BB} - \kappa_{AA})/(4k_B). \quad (9.17)$$

where κ is the dimensional bulk modulus.

The properties of the crystalline phase are more complicated but at the simplest level the only real difference is that the elastic energy associated with the crystalline state must be incorporated. This is discussed in the next section.

9.3 Crystalline Phase Properties

To illustrate the properties of the crystalline state, the case in which the concentration field is a constant is considered. In this limit the free energy functional given in Eq. 9.7 can be written in the form

$$\frac{\mathcal{F}}{k_B T} \equiv \int d\vec{r} \left[\rho \ln \left(\frac{\rho}{\rho_\ell} \right) - \delta\rho - \frac{1}{2} \delta\rho \bar{C} \delta\rho + G \right] \quad (9.18)$$

where G is a function of the concentration c and ρ_ℓ and couples only linearly to $\delta\rho$. The operator \bar{C} can be written as

$$\bar{C} \equiv c^2 C^{AA} + (1-c)^2 C^{BB} + 2c(1-c) C^{AB}. \quad (9.19)$$

Thus in the limit that the concentration is constant this free energy functional is that of a pure material with an effective two point correlation function that is an average over the AA , BB and AB interactions. In this limit the calculations presented in section 7.2 can be repeated using the same approximations (i.e., expanding ρ around ρ_ℓ , expanding \bar{C} to ∇^4 and using a one mode approximation for $\delta\rho$) to obtain predictions for the concentration dependence of various quantities.

As a more specific example the equilibrium lattice constant which appears implicitly in the correlation functions in Eq. 9.19 [114] can be expanded around $c = 1/2$ to obtain in two or three dimensions,

$$a_{eq}(\delta c) = a_{eq}(0) (1 + \eta \delta c + \dots) \quad (9.20)$$

where $\delta c = c - 1/2$ and η is the solute expansion coefficient given by,

$$\eta = (\delta \hat{C}_4 - \delta \hat{C}_2)/2 \quad (9.21)$$

and where

$$\delta \hat{C}_n \equiv (\hat{C}_n^{AA} - \hat{C}_n^{BB})/\hat{\tilde{C}}_n \quad (9.22)$$

while $\hat{\tilde{C}}_n \equiv \hat{C}_n(\delta c = 0) = (\hat{C}_n^{AA} + \hat{C}_n^{BB} + 2\hat{C}_n^{AB})/4$.

This line of reasoning can also be used to understand the influence of alloy concentration on crystallization. Specifically, for the case of an alloy, the terms in

Eq. 7.26 become functions of concentration, since ΔB and A_{min} are concentration dependent. Here, ΔB can be expanded around $c = 1/2$, i.e.,

$$\Delta B(\delta c) = \Delta B_0 + \Delta B_1 \delta c + \Delta B_2 \delta c^2 + \dots \quad (9.23)$$

where $\Delta B_0 = B_0^l - B_0^s$, $\Delta B_1 = B_1^l - B_1^s$ and $\Delta B_2 = B_2^l - B_2^s$ are determined in the Appendix B. This would imply that in the crystalline phase the free energy has a term of the form, $r^c(\delta c)^2$, where

$$r^c = r^\ell + 3\Delta B_2 A_{min}^2 / 8 \quad (9.24)$$

in two dimensions (in three dimensions the $3/8$ factor is replaced with $3/4$). This result indicates that crystallization (i.e., a non-zero A_{min}) favours phase segregation, assuming $\kappa_{AA} + \kappa_{BB} < 2\kappa_{AB}$. For example, when $B_2^s = 0$, the critical temperature increases and can be written,

$$T_C^c = T_C^\ell (1 + 3A_{min}^2 / 8), \quad (9.25)$$

or $T_C^c = T_C^\ell (1 + 3A_{min}^2 / 4)$ in three dimensions.

9.4 Simple Binary Alloy Model

In this section a simple binary alloy model is proposed based on a simplification of the free energy in Eq. 9.7. The goal of this section is to develop a mathematically *simple* model free energy for a binary system that can be used to simultaneously model grain growth, solidification, phase segregation in the presence of elastic and plastic deformation. To simplify calculations it is convenient to first introduce the following dimensionless fields,

$$\begin{aligned} n_A &\equiv (\rho_A - \bar{\rho}_A) / \bar{\rho} \\ n_B &\equiv (\rho_B - \bar{\rho}_B) / \bar{\rho}. \end{aligned} \quad (9.26)$$

Also, it is convenient to expand Eq. 9.7

$$\begin{aligned}
 \frac{\mathcal{F}}{k_B T} &= \int d\vec{r} \left[\rho \ln(\rho/\rho_\ell) - \delta\rho + \beta\delta c + F_o \right. \\
 &\quad - \frac{1}{2} \delta\rho \{ c C^{AA} + (1-c) C^{BB} \} \delta\rho \\
 &\quad + \rho \{ c \ln(c) + (1-c) \ln(1-c) \} \\
 &\quad \left. + \rho c \{ (C^{AA} + C^{BB})/2 - C^{AB} \} (1-c) \rho \right]
 \end{aligned}$$

in the following two fields,

$$\begin{aligned}
 n &= n_A + n_B \\
 \delta N &= (n_B - n_A) + \frac{\bar{\rho}_B - \bar{\rho}_A}{\bar{\rho}}.
 \end{aligned} \tag{9.27}$$

The following calculations will use the field δN instead of δc . Expanding Eq. 9.7 around $\delta N = 0$ and $n = 0$ gives a free energy of the form ¹

$$\begin{aligned}
 \frac{\mathcal{F}}{\bar{\rho} k_B T} &= \int d\vec{r} \left(\frac{n}{2} \left[B^\ell + B^s (2R^2 \nabla^2 + R^4 \nabla^4) \right] n \right. \\
 &\quad + \frac{t}{3} n^3 - \frac{v}{4} n^4 + \gamma \delta N + \frac{w}{2} \delta N^2 + \frac{u}{4} \delta N^4 \\
 &\quad \left. + \frac{L^2}{2} |\vec{\nabla} \delta N|^2 + \dots \right).
 \end{aligned} \tag{9.28}$$

The calculations presented in this section are for a two dimensional system. The constants (t , v , w , u , L , R , B^ℓ and B^s) as well as the details of going from Eq. 9.7 to Eq. 9.28 are shown in Appendix B.

The transition from liquid to solid is intimately related to $\Delta B = B^\ell - B^s$, as was the case for the pure material, and can be written in terms of a temperature difference, i.e., Eq. 7.15. In addition, some of the polynomial terms in n and δN have been multiplied by variable coefficients (t , v , w and u) even though they can be derived exactly as shown in Appendix B. For example, the parameter $v = 1/3$ recovers the exact form of the n^4 term derived in Appendix B. This flexibility in the choice of coefficients was done to be able to match the parameter of the free energy

¹Most of these calculations are quite lengthy and were done using the Maple software. Only the results of these lengthy manipulations are shown here, along with the explanation necessary to reproduce all of our steps.

with experimental material parameters [115]. L is a gradients energy coefficient and R sets the scale so the inter-atomic spacing of the total density n .

To facilitate the calculation of the lowest order phase diagram corresponding to the free energy in Eq. 9.28, it is important to note that re-defined "concentration" field δN varies significantly over length scales much larger than the atomic number density field n . As a result, the density field can be integrated out of the free energy functional (i.e. treated as if it were a constant in the integrand of the free energy). Also, in the spirit of keeping calculations as simple as possible without losing the basic physics contained in the model, $\gamma = 0$ in the free energy. In this instance, the one-mode approximation for the total density (Eq. 7.25) i.e., $n = A[\cos(2qy/\sqrt{3})/2 - \cos(qx) \cos(qy\sqrt{3})]$ will be used. Substituting this expression into Eq. 9.28 and minimizing with respect to q and A (recalling that δN is assumed constant over the scale that n varies) gives

$$q_{eq} = \sqrt{3}/(2R) \quad (9.29)$$

and

$$A_{min} = 4 \frac{t + \sqrt{t^2 - 15v\Delta B}}{15v}. \quad (9.30)$$

The free energy that is minimized with respect to amplitude and lattice constant is then,

$$\begin{aligned} F_{sol} = & \frac{w}{2}\delta N^2 + \frac{u}{4}\delta N^4 + \frac{3}{16}\Delta B A_{min}^2 - \frac{t}{16}A_{min}^3 \\ & + \frac{45v}{512}A_{min}^4. \end{aligned} \quad (9.31)$$

Most coefficients are dependent of the concentration δN . For mathematical simplicity, all further calculations will be limited to the approximations $B^\ell = B_0^\ell + B_2^\ell(\delta N)^2$ and $B^s = B_0^s$. In this limit, analytic expressions can be obtained for a number of quantities and the free energy functional is still general enough to produce a eutectic phase diagram , for example.

9.4.1 Solid-Solid Coexistence of Phase Diagram

It is relatively simple to calculate the solid-solid coexistence curves by expanding F_{sol} to order $(\delta N)^4$, which then yields the solid/solid coexistence concentrations at low temperatures according to

$$\delta N_{coex} = \pm \sqrt{|a|/b} \quad (9.32)$$

where $a \equiv w + 3B_2^\ell (A_{min}^o)^2/8$, $b \equiv u - 6(B_2^\ell)^2 A_{min}^o / (15vA_{min}^o - 4t)$ and $A_{min}^o \equiv A_{min}(\delta N = 0)$ (which is thus a function of ΔB_0). The critical temperature, ΔB_0^C is determined by setting $\delta N_{coex} = 0$ and solving for ΔB_0 , which gives,

$$\Delta B_0^C = \left(15wv - 2t\sqrt{-6B_2^\ell w} \right) / (6B_2^\ell). \quad (9.33)$$

9.4.2 Solid-Liquid Coexistence

To obtain the liquid/solid coexistence lines the free energy of the liquid state must be compared to that of the solid. The mean field free energy of the liquid state is obtained by setting $n = 0$ which gives,

$$F_{liq} = \frac{w}{2}\delta N^2 + \frac{u}{4}\delta N^4. \quad (9.34)$$

To obtain the solid-liquid coexistence lines it is useful to expand the free energy of the liquid and solid states around the value of δN at which the liquid and solid states have the same free energy, i.e., when $F_{sol} = F_{liq}$. This occurs when, $\delta N_{ls} = \pm \sqrt{(\Delta B_0^{ls} - \Delta B_o)/B_2^\ell}$, where $\Delta B_o \equiv B_0^l - B_0^s$ and $\Delta B_0^{ls} \equiv 8t^2/(135v)$ is the lowest value of ΔB_0^{ls} at which a liquid can coexist with a solid. To complete the calculations, F_{sol} and F_{liq} are expanded around δN_{ls} to order $(\delta N - \delta N_{ls})^2$ and Maxwell's equal area construction rule can be used to identify the liquid/solid coexistence lines. The liquid/solid lines are;

$$\begin{aligned} \delta N_{liq}/\delta N_{ls} &= 1 + G \left(1 - \sqrt{b_{sol}/b_{liq}} \right) \\ \delta N_{sol}/\delta N_{ls} &= 1 + G \left(1 - \sqrt{b_{liq}/b_{sol}} \right). \end{aligned} \quad (9.35)$$

where, $G \equiv -8t^2/(135v(4\Delta B_0 - 3\Delta B_0^{ls}))$, $b_{liq} = (w + 3u\delta N_{ls}^2)/2$ and $b_{sol} = b_{liq} + 2B_2^\ell(4\Delta B_0 - 3\Delta B_0^{ls})/(5v)$, for $\delta N_{liq} > 0$, $\delta N_{sol} > 0$ and similar results for $\delta N_{liq} < 0$, $\delta N_{sol} < 0$, since F is a function of δN^2 in this example. The calculations in this section and the previous section are reasonably accurate when $\Delta B_0^{ls} > \Delta B_0^c$, however in the opposite limit a eutectic phase diagram forms and the accuracy of the calculations decreases. This case will be discussed below.

9.5 Calculation of Alloy Phase Diagrams

To examine the validity of some of the approximations for the phase diagrams made in the previous section, numerical simulations were conducted to determine the properties of the solid and liquid equilibrium states. The simulations were performed over a range of δN values, three values of ΔB_0 (0.07, 0.02 and -0.03) and two values of w (0.088 and -0.04). The specific values of the other constants that enter the model are given in the figure caption of Fig. 9.1. In general the numerical results for the free energy, F , the lattice constant R and bulk modulus agreed quite well with the analytic one-mode predictions presented in the previous section for all parameters. Comparisons of the analytic and numerical predictions for the phase diagram are shown in Fig. 9.1 and Fig. 9.2 for $w = 0.088$ and -0.04 , respectively. As seen in these, figures the agreement is quite good except near the eutectic point shown in Fig. 9.2. In this case, the analytic calculations (Eqns. 9.35 and Eqns. 9.32) for the coexistence lines break down at the eutectic point and higher order terms in δN are needed to accurately predict the phase diagram.

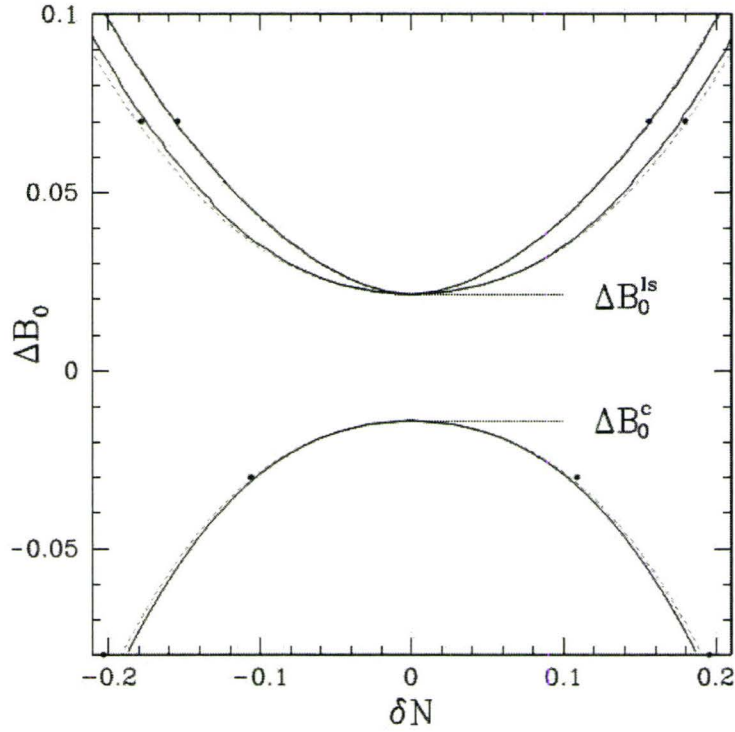


Figure 9.1: Phase diagram of ΔB_0 Vs. δN for the parameters $B_0^s = 1.00$, $B_1^\ell = 0$, $B_2^\ell = -1.80$, $t = 0.60$, $v = 1.00$, $w = 0.088$, $u = 4.00$, $L = 4.00$, $\gamma = 0$, $R_0 = 1.00$ and $R_1 = 1.20$ (see Eq. B.4 for definitions of R_0 and R_1). The solid line is a numerical solution of the one mode approximation and the dashed lines are from Eq. 9.32 for the lower solid/solid coexistence lines and Eq. 9.35 for the upper liquid/solid coexistence lines. The solid points are from numerical solutions for the minimum free energy functional given in Eq. 9.28. [114]

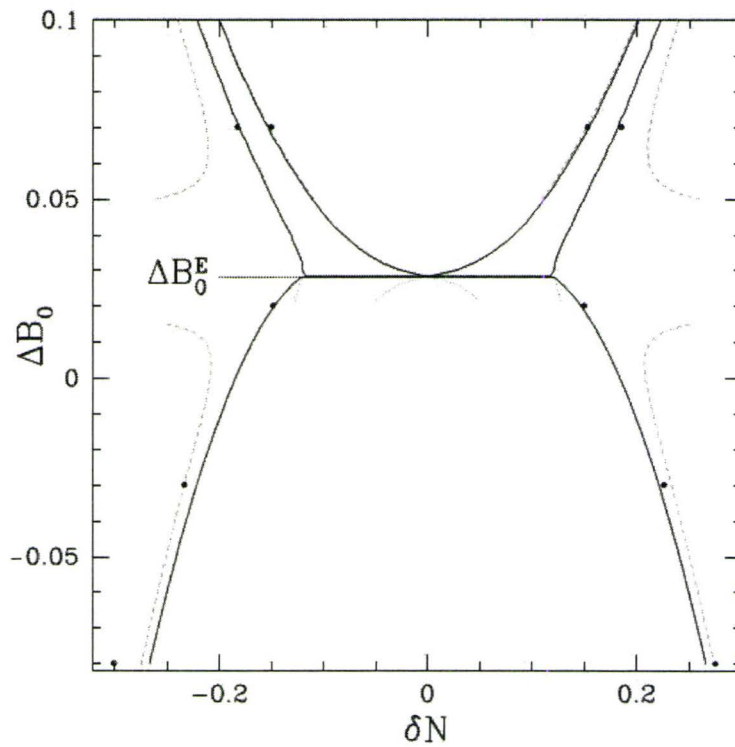


Figure 9.2: Phase diagram of ΔB_0 Vs. δN for the same parameters as those used to generate Fig. 9.1, with the exception that $w = -0.04$. The dotted lines below the eutectic temperature, $\Delta B_0^E \approx 0.028$, correspond to metastable states. [114]

9.6 Dynamics

To simulate microstructure formation in binary alloys, dynamical equations of motions for the concentration and density fields need to be developed. The starting point is the full free energy in Eq. 9.1, written in terms of ρ_A and ρ_B , i.e., $\mathcal{F}(\rho_A, \rho_B)$. The dynamics of ρ_A and ρ_B is driven by free energy minimization.

We consider changes in the continuum defined by the temporally coarse-grained density fields ρ_A and ρ_B to be consistent with some effective velocity field \vec{v} . Considering conservation of mass for each species within a control volume, we arrive at

$$\begin{aligned}\frac{\partial \rho_A}{\partial t} &= -\nabla \cdot (\rho_A \vec{v}) = -\partial_i(\rho_A v_i) \\ \frac{\partial \rho_B}{\partial t} &= -\nabla \cdot (\rho_B \vec{v}) = -\partial_i(\rho_B v_i)\end{aligned}\tag{9.36}$$

Changes to the net momentum of a control volume are similarly related to a divergence of a generalized stress tensor according to

$$\frac{\partial (\rho_{\text{tot}} v_i)}{\partial t} \equiv \frac{\partial ((\rho_A + \rho_B) v_i)}{\partial t} = -\partial_j \sigma_{ij}\tag{9.37}$$

Taking the divergence of both side of Eq. (9.37) gives

$$\frac{\partial}{\partial t} \{\partial_i(\rho_A v_i) + \partial_i(\rho_B v_i)\} = -\partial_i \partial_j \sigma_{ij}\tag{9.38}$$

which, using both of Eqs. (9.36) into Eq. (9.38), gives

$$\frac{\partial^2}{\partial t^2} \{\rho_A + \rho_B\} = \bar{\rho} \frac{\partial^2 n}{\partial t^2} = \partial_i \partial_j \sigma_{ij}\tag{9.39}$$

where we have defined $n = (\rho_A + \rho_B)/\bar{\rho}$ and $\bar{\rho}$ is the average alloy density. We did this to arrive at a modified phase field crystal alloy model written in the same field variables as our original alloy model in Ref. [19].

For one component, the contraction of the stress tensor has be shown [21] to

be of the form

$$\partial_i \partial_j \sigma_{ij} = \nabla \cdot (\rho_A \nabla \mu_A) + \mathcal{L}(\rho_A) = \nabla \cdot \left(\rho_A \frac{\delta F}{\delta \rho_A} \right) + \mathcal{L}(\rho_A) \quad (9.40)$$

where $\mathcal{L}(\rho)$ represents a generalized dissipation tensor and where terms of order $\mathcal{O}(v_i v_j)$ have been neglected. To pass onto the case of the alloy, we generalize Eq. 9.40 to have contributions due to changes in both components,

$$\partial_i \partial_j \sigma_{ij} = \nabla \cdot \left(\rho_A \frac{\delta F}{\delta \rho_A} \right) + \nabla \cdot \left(\rho_B \frac{\delta F}{\delta \rho_B} \right) + \mathcal{L}(\rho_A, \rho_B) \quad (9.41)$$

The dissipation term has also be generalized to a function of both species densities.

The simplest way to express the dissipation tensor $\mathcal{L}(\rho_A, \rho_B)$ is

$$\mathcal{L}(\rho_A, \rho_B) = -\frac{1}{\beta} \frac{\partial n}{\partial t} \quad (9.42)$$

where β is a phenomenological constant meant to make contact with the damping term in the MPFC model. While more formal expression exist [21], our aim here is merely to relax density changes across scales orders of magnitude larger than the atomic spacing on time scales significantly larger than phonon time scales but still much slower than diffusion time scales.

The chemical potential terms in Eq. 9.41 can be simplified as follows. We first write the free energy in terms of the variables n and $c = (\rho_B - \rho_A)/\bar{\rho}$ in order to make contact with the fields used in the alloy model of Ref. [114]. Doing so gives,

$$\begin{aligned} \nabla \cdot \left(\rho_A \frac{\delta F}{\delta \rho_A} \right) &= (M_A \nabla^2 + \nabla \cdot M_A \nabla) \left(\frac{\delta F}{\delta n} \frac{\delta n}{\delta \rho_A} + \frac{\delta F}{\delta c} \frac{\delta c}{\delta \rho_A} \right) \\ \nabla \cdot \left(\rho_B \frac{\delta F}{\delta \rho_B} \right) &= (M_B \nabla^2 + \nabla \cdot M_B \nabla) \left(\frac{\delta F}{\delta n} \frac{\delta n}{\delta \rho_B} + \frac{\delta F}{\delta c} \frac{\delta c}{\delta \rho_B} \right) \end{aligned} \quad (9.43)$$

Using the definitions of n and c and adding the left hand sides of Eqs. 9.43, we arrive at

$$\nabla \cdot \left(\rho_A \frac{\delta F}{\delta \rho_A} \right) + \nabla \cdot \left(\rho_B \frac{\delta F}{\delta \rho_B} \right) = \{n \nabla^2 + \nabla n \cdot \nabla\} \frac{\delta \mathcal{F}}{\delta n}$$

$$+ \left\{ c \nabla^2 + \nabla c \cdot \nabla \right\} \frac{\delta \mathcal{F}}{\delta c} \quad (9.44)$$

Equation 9.44 can be cast into the simpler form,

$$\nabla \cdot \left(\rho_A \frac{\delta F}{\delta \rho_A} \right) + \nabla \cdot \left(\rho_B \frac{\delta F}{\delta \rho_B} \right) = \vec{\nabla} \cdot \left\{ n \vec{\nabla} \frac{\delta \mathcal{F}}{\delta n} \right\} + \vec{\nabla} \cdot \left\{ c \vec{\nabla} \frac{\delta \mathcal{F}}{\delta c} \right\} \quad (9.45)$$

Substituting Eq. 9.45 and Eq. 9.42 into Eq. 9.39 gives the equation of motion for the density field,

$$\bar{\rho} \frac{\partial^2 n}{\partial t^2} + \frac{1}{\beta} \frac{\partial n}{\partial t} = \vec{\nabla} \cdot \left\{ n \vec{\nabla} \frac{\delta \mathcal{F}}{\delta n} \right\} + \vec{\nabla} \cdot \left\{ c \vec{\nabla} \frac{\delta \mathcal{F}}{\delta c} \right\} \quad (9.46)$$

The second term on the right hand side of Eq. 9.46 can be recognized as the divergence of a flux driven by change in the chemical potential with respect to the generalized concentration field $c = (\rho_B - \rho_A)/\bar{\rho}$. While n must respond on two times scales to describe the so-called "quasi-phonon" behavior and the slower diffusive re-arrangement atoms, the field c is expected to change only on diffusive time scales, and is thus thus controlled by changes of solute diffusion. Its dynamics are thus expressed as

$$\vec{\nabla} \cdot \left\{ c \vec{\nabla} \frac{\delta \mathcal{F}}{\delta c} \right\} = \frac{1}{M} \frac{\partial c}{\partial t} \quad (9.47)$$

where M is proportional to the chemical mobility controlling the rate of inter-diffusion. Equations 9.46 and 9.47 comprise a set of closed equations for the evolution of total density and density difference in a binary alloy. For alloys near the spinodal concentration $c \ll 1$ and the chemical flux term can be neglected on the right hand side of Eq. 9.46 compared to the first term. Applying this simplification, we arrive at a modified phase field crystal model

$$\begin{aligned} \bar{\rho} \frac{\partial^2 n}{\partial t^2} + \frac{1}{\beta} \frac{\partial n}{\partial t} &= \vec{\nabla} \cdot \left\{ n \vec{\nabla} \frac{\delta \mathcal{F}}{\delta n} \right\} \\ \frac{\partial c}{\partial t} &= M \left\{ \frac{\delta \mathcal{F}}{\delta c} \right\} \end{aligned} \quad (9.48)$$

9.7 Dendritic Solidification

To illustrate the dynamics described by Eqs. 9.48, using the free energy in Eq. 9.28, a simulation of heterogeneous crystallization from liquid cooled to the coexistence region in the phase diagram displayed on Fig. 9.1 was conducted. The simulation started with a small perturbation in the density introduced into super-cooled liquid. To reduce computational time the size of the simulation lattice was gradually increased as the seed grew in size. The initial perturbation developed into a circular shape (Fig. 9.3a) at $t=40000$. At later stages ($t=80000$, 120000) of solidification (Fig. 9.3b,c), we observed the formation of dendrite tips. Finally, a fully developed dendrite developed with signs of sidebranching. The dendrite developed and retained sixfold symmetry of underlying microstructure. The final shape of the dendrite, after 200000 time steps is shown on Fig. 9.4. To highlight the ability of the model to resolve multiple scales, a small portion of density field at solid-liquid interface is plotted in the top right corner of the Fig. 9.4. In other words, we can simulate the structure size of the dendrite while still retaining information on the atomistic level. This novel dendritic growth modeling can be used to study two main issues; the first being how atomic re-arrangement times at the interface can influence non-equilibrium solute partitioning during rapid solidification, the second being, the role that stresses applied to dendritic structures can have in leading to dendrite fragmentation.

To test microsegregation along in the crystal, Fig. 9.5b plots a portion of the coexistence region phase diagram of Fig. 9.1. At the bottom of the figure, the microsegregation profile along the center of the dendrite Fig. 9.5a is plotted. It should be noted here that concentration and temperature are both in dimensionless units, causing the profile to appear different than usual concentration profile. Nevertheless, it can be seen from the profile of δN that the solute is rejected from the solid. There is a build up of solute ahead of the solid and in the beginning of the solidification (center of the dendrite), an initial transient can be seen. Quantitative values from the profile can be related back to the phase diagram. Measurements such as these allow us to study microstructural properties such as the growth velocity of a dendrite tip or verify accuracy of concentration profiles with respect to the phase diagram and experimental measurements. We will explore more properties of the alloy PFC

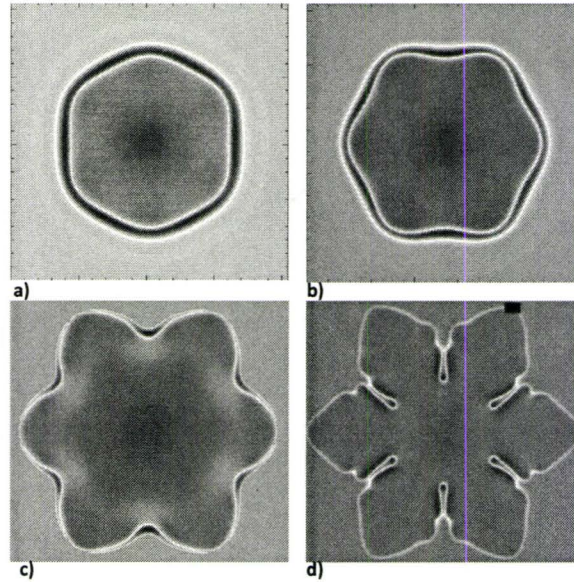


Figure 9.3: Four stages – time steps – of rapidly solidified dendrite crystal grown from supercooled liquid with dimensionless concentration $\delta N_0 = 0.11$ and dimensionless temperature 0.05 in two dimensions. Other parameters are the same as in Fig. 9.1 except $L = 1.2$ and $R_1/R_0 = 1/4$. Frames a, b, c and d correspond to times $t = 40000$, 80000, 120000 and 160000 respectively.

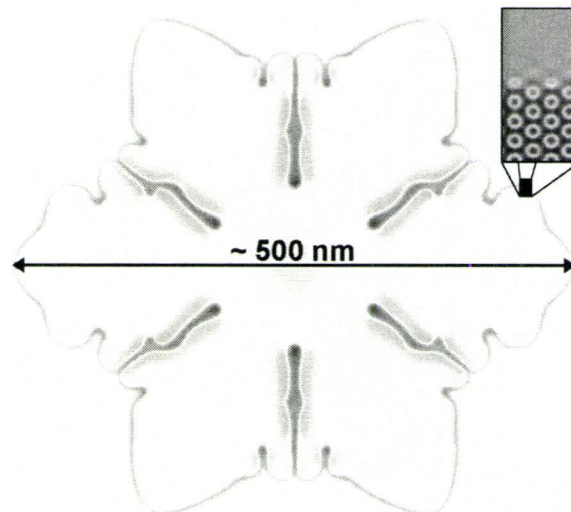


Figure 9.4: A rapidly solidified dendrite crystal grown from supercooled liquid with dimensionless concentration $\delta N_0 = 0.11$ and dimensionless temperature 0.05 in two dimensions. Other parameters are the same as in Fig. 9.1 except $L = 1.2$ and $R_1/R_0 = 1/4$. Time corresponds to $t = 200000$. **Inset:** A small portion of density field n at solid-liquid interface.

model and compare simulation results with the results from other simulations and experiments in section 11.9, which is devoted to spinodal decomposition studies.

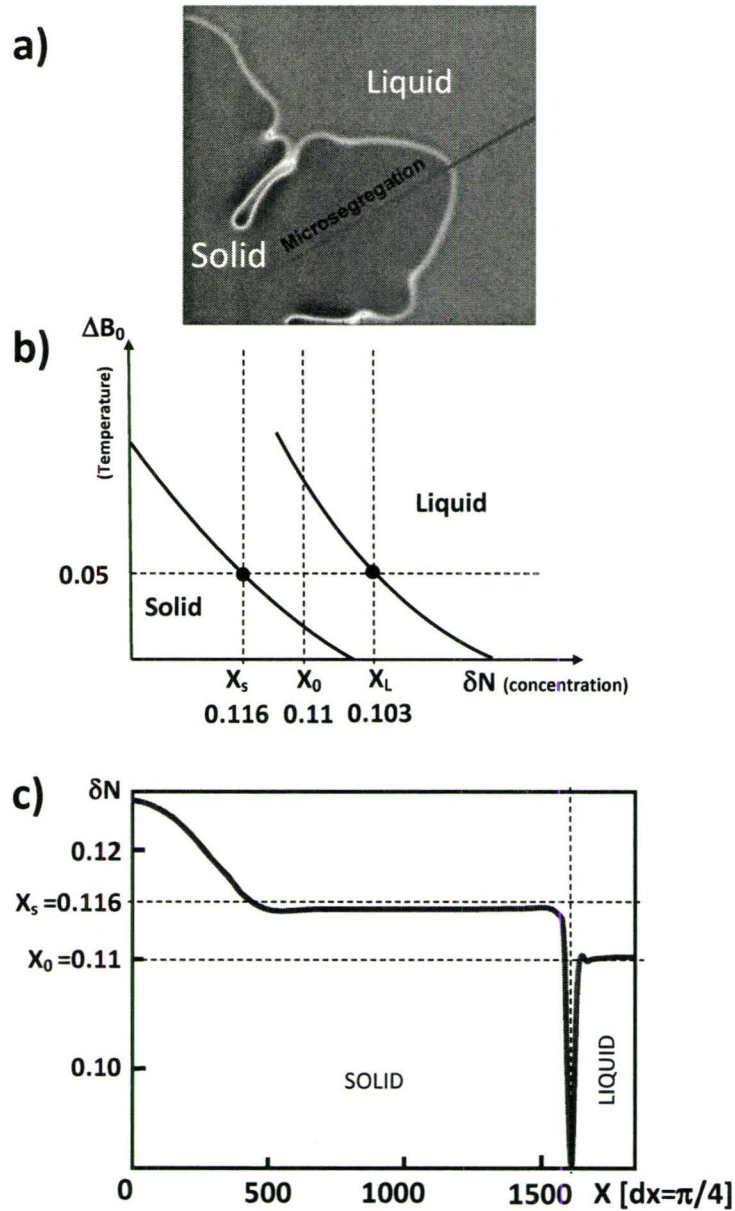


Figure 9.5: a) Dendrite tip with highlighted line along which the microsegregation profile was plotted. b) A portion of the phase diagram Fig. 9.1. c) Micro segregation profile along the dendrite tip.

Chapter 10

Efficient Semi-Implicit Solver Development

In the previous section, we outlined theory and demonstrated elastic deformations in a smaller scale model. In order to study problems such as the reversed Hall-Petch effect, we need to be able to simulate many nanocrystalline grains over longer periods of time. This poses a high demand on numerical efficiency of the solver. Currently, the size of the sample and the length of the simulation were both limited by the efficiency of explicit euler time marching methods. To circumvent the limitations we developed a semi implicit multigrid solver which will be described in the following section.

The MPFC equation of motion (Eq. 8.1) is challenging to solve numerically. The first challenge is posed by the sixth-order space derivative which introduces time step restrictions - stiffness. For the previously used explicit method, stability criteria is approximately $\Delta t < \approx \Delta x^6$. The second challenge is that there is a cubic nonlinear term on the RHS, contributing to overall stiffness of the equation. To avoid the 6th-order derivative limitation imposed by explicit methods, we employ a semi-implicit numerical scheme.

We begin by splitting the equations 8.1 into a system of three second order equations as follows:

$$\frac{\partial^2 \rho(\mathbf{x})}{\partial t^2} + \beta \frac{\partial \rho(\mathbf{x})}{\partial t} = \alpha^2 \nabla^2 \mu(\mathbf{x}), \quad (10.1)$$

$$\begin{aligned}\mu(\mathbf{x}) &= r\rho(\mathbf{x}) + \rho(\mathbf{x}) + 2v + \nabla^2 v(\mathbf{x}) + \rho(\mathbf{x})^3, \\ v(\mathbf{x}) &= \nabla^2 \rho(\mathbf{x}) \\ (\mathbf{x} \in \Omega)\end{aligned}$$

Here $\mathbf{x} = (x_1, x_2)$ and $\Omega \subset R$ is a given domain. We discretize the system 10.1 in 2D space as:

$$\begin{aligned}\frac{\partial^2 \rho_h(x, y)}{\partial t^2} + \beta \frac{\partial \rho_h(x, y)}{\partial t} &= \alpha^2 \nabla^2 \mu_h(x, y), \\ \mu_h(x, y) &= r\rho_h(x, y) + \rho_h(x, y) + 2v + \nabla^2 v_h(x, y) + \rho_h(x, y)^3, \\ v_h(x, y) &= \nabla^2 \rho_h(x, y) \\ ((x, y) \in \Omega_h)\end{aligned}\tag{10.2}$$

here h is a discretization parameter and for square uniform grid we can write: $\Omega_h = \{(x, y) : x = x_i = ih, y = y_j = jh; 1 \leq i \leq N, 1 \leq j \leq N\}$. Using the above discretization in space we discretize the system in time by the following implicit type algorithm:

$$\begin{aligned}\frac{\rho_{i,j}^{n+1} - 2\rho_{i,j}^n + \rho_{i,j}^{n-1}}{dt^2} + \frac{\beta(\rho_{i,j}^{n+1} - \rho_{i,j}^{n-1})}{2dt} &= \frac{\alpha^2(\mu_{i-1,j}^{n+1/2} + \mu_{i+1,j}^{n+1/2} + \mu_{i,j+1}^{n+1/2} + \mu_{i,j-1}^{n+1/2} - 4\mu_{i,j}^{n+1/2})}{h^2} \\ \mu_{i,j}^{n+1/2} &= \rho_{i,j}^{n+1} + r\rho_{i,j}^{n+1} + 2v_{i,j}^{n+1} + \frac{v_{i-1,j}^{n+1} + v_{i+1,j}^{n+1} + v_{i,j+1}^{n+1} + v_{i,j-1}^{n+1} - 4v_{i,j}^{n+1}}{h^2} + \hat{\phi}(\mu_{i,j}^n, \mu_{i,j}^{n+1}) \\ v_{i,j}^{n+1} &= \frac{\rho_{i-1,j}^{n+1} + \rho_{i+1,j}^{n+1} + \rho_{i,j+1}^{n+1} + \rho_{i,j-1}^{n+1} - 4\rho_{i,j}^{n+1} + \rho_{i-1,j}^n + \rho_{i+1,j}^n + \rho_{i,j+1}^n + \rho_{i,j-1}^n - 4\rho_{i,j}^n}{2h^2}\end{aligned}\tag{10.3}$$

Where: $\hat{\phi}(\mu_{i,j}^n, \mu_{i,j}^{n+1}) = (\rho_{i,j}^{n+1})^3$ is a linearized nonlinear part.

10.1 Iterative Solver

Having set up an implicit system of equations we can solve the system in Eq. 10.3 iteratively by a method of choice such as Gauss Seidel or Successive overrelaxation (SOR) [116]. The iteration update formula reads:

$$\begin{pmatrix} \beta dt/2 + 1 & 4\alpha^2 dt^2/dx^2 & 0 \\ (-1 - r) - 3/2(\rho_{i,j}^{n,2} + \rho_{i,j}^{m,2}) & 1 & 4/dx^2 - 2 \\ 2/dx^2 & 0 & 1 \end{pmatrix} \begin{pmatrix} \rho_{i,j}^{m+1} \\ \mu_{i,j}^{m+1/2} \\ v_{i,j}^{m+1} \end{pmatrix} =$$

$$\begin{pmatrix} 2\rho_{i,j}^n + \rho_{i,j}^{n-1} (\beta dt/2 - 1) + 4\alpha^2 dt^2/dx^2 (\mu_{i-1,j}^{m+1/2} + \mu_{i+1,j}^{m+1/2} + \mu_{i,j+1}^{m+1/2} + \mu_{i,j-1}^{m+1/2}) \\ (v_{i-1,j}^{m+1} + v_{i+1,j}^{m+1} + v_{i,j+1}^{m+1} + v_{i,j-1}^{m+1})/dx^2 + 1/2 (\rho_{i,j}^{n,3} + \rho_{i,j}^{m,3}) - 3/2 (\rho_{i,j}^{n,2} + \rho_{i,j}^{m,2}) \rho_{i,j}^n \\ (\rho_{i-1,j}^{m+1} + \rho_{i+1,j}^{m+1} + \rho_{i,j+1}^{m+1} + \rho_{i,j-1}^{m+1} + \rho_{i-1,j}^n + \rho_{i+1,j}^n + \rho_{i,j+1}^n + \rho_{i,j-1}^n - 4\rho_{i,j}^n)/2dx^2 \end{pmatrix} \quad (10.4)$$

Here m and $m + 1$ terms are approximations before and after iteration, respectively. For each iteration step we solve Eqs. 10.4 by inverting 3×3 matrix. A severe problem with traditional matrix solvers is that they require of N^2 order iterations to converge to the answer of the next time step, where N is the number of nodes on a numerical mesh, see also Fig. 10.7. This problem is addressed by using an efficient multi-grid solver, discussed next.

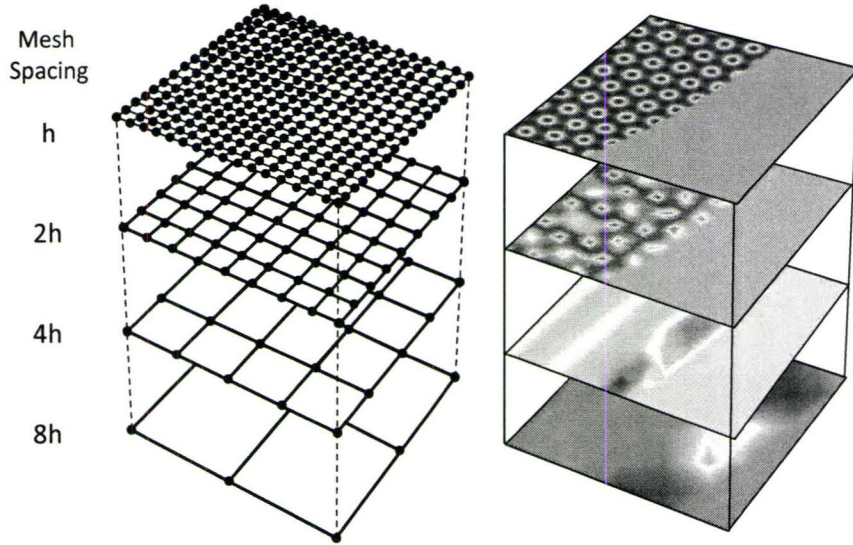


Figure 10.1: **Left:** Four level multigrid grid. **Right:** Density function in a multigrid representation.

10.2 Multigrid Solver

10.2.1 Introduction

In this section, we will discuss a *multigrid method* and its application to the solution of the MPFC equation of motion in Eq. 8.1 or the discrete analogue in Eq. 10.4. As the name suggests the multigrid method uses multiple grids – discretizations – to

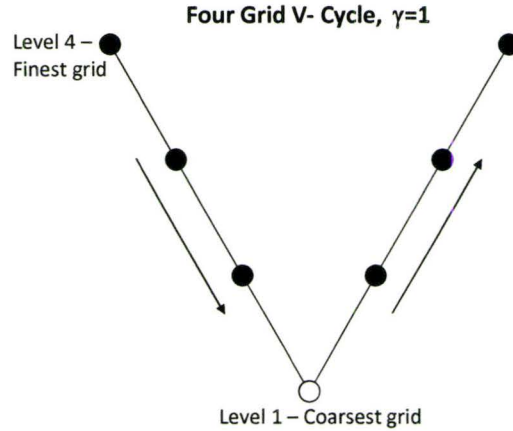


Figure 10.2: Multigrid V-cycle. The defect equation is solved exactly on the coarsest level 1 (empty circle). On the levels 2 to 4 (full circles) only smoothing is performed by running $k - grid$ cycles using level 1 grid as an approximation. Cycle index $\gamma = 1$.

represent discretized problem. Each grid (or synonymous mesh) differs in its discretizations parameter. From the finest grid (Ω_k) with discretization h , through more coarse grid (indexed as Ω_{k-1}) with the discretization parameter $2h$ up to the coarsest grid (indexed as $\Omega_{k=0}$) where only 9 discrete points are involved. An illustration of such meshing is found on Fig. 10.1.

Let us further explain the basic idea of a multigrid using the discrete poisson equation $-\nabla u_h(x, y) = f_h^\Omega(x, y), (x, y) \in \Omega_h$; in a simplified notation:

$$L_h u_h = f_h \tag{10.5}$$

where $L_h = -\nabla_h$ is the standard five point stencil (i.e. a finite difference operation) for the second order differential operator, which can be written as:

$$L_h u_h(x, y) = \frac{1}{h^2} [4u_h(x, y) - u_h(x - h, y) - u_h(x + h, y) - u_h(x, y - h) - u_h(x, y + h)] \tag{10.6}$$

In multigrid we define an *error* by

$$v_h^m = u_h - u_h^m \tag{10.7}$$

which is the difference between u_h and its approximation u_h^m , which is the solution

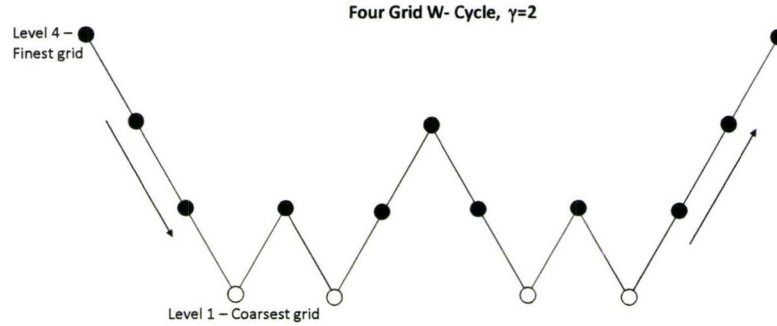


Figure 10.3: Multigrid W-cycle. Distinction between V and W cycles is made through *cycle index* γ . See text for details.

approximated after m iterations of Eq. 10.4 on a mesh of grid parameter h . The difference between the right hand side f_h and the left hand side operator $L_h u_h$ in Eq. 10.5, after m iterations (using, for instance, an iterative scheme such as Eq. 10.4), is called a *defect*:

$$d_h^m = f_h - L_h u_h^m. \quad (10.8)$$

If we substitute Eq. 10.7 into Eq. 10.8, an equation for the error in terms of the defect (called the defect equation) can be written as $L_h v_h^m = d_h^m$. The essence of a multigrid is that, instead of computing v_m on a current grid Ω_k , we restrict the defect to a coarser grid Ω_{k-1} . The restricted defect equation is then solved approximately, (or exactly on the lower grid,) to obtain the error v_{k-1}^m . The final step is to interpolate the error back to the higher level (denser) grid, thus obtaining v_k^m . The addition of v_k^m to the initial approximation after m iterations, u_k^m , can then be used to obtain the exact solution u_h . This procedure, outlined here for two grid levels, can be made recursive so that the restricted defect equation, like the original Poisson equation, can itself only be approximated by referring to an even coarser mesh Ω_{k-2} , and so on, down to the coarsest possible mesh. One multigrid cycle is obtained by repeating the previous steps from the highest to lowest grid and back, as shown in Fig. 10.2, which is called a V-cycle. Because error is accrued in the procedure of solving defects on coarser grids (i.e. obtaining estimates of u_h^m at the different levels), the V-cycles illustrated in Fig. 10.2 may have to be repeated several times, serving as iteration cycles themselves. The advantage of the multigrid method is that only a few V-cycles

are required for convergence, and each V-cycle comprises only a few smoothing steps (i.e. iterations of Eq. 10.4) (1-2) per level. As a result the total iteration "investment" for multigrid convergence is much smaller than N^2 for traditional iterative solvers that work entirely on the finest mesh. Another type of cycle is known as a W-cycle, shown in Fig. 10.3. Distinction between V and W-cycle is made through *cycle index* γ .

10.2.2 The Components of Multigrid

In the following we will show a more formal description of the multigrid method and a characteristic multigrid cycle. We start by listing key components of the multigrid:

- **A sequence of progressively coarser grids** Ω_k , characterized by a sequence of mesh sizes $h_k: \Omega_\ell, \Omega_{\ell-1}, \dots, \Omega_0$
- Set of **linear operators** for each Ω_k . $\mathcal{G}(\Omega_k)$ denotes the *linear space of grid functions on Ω_k* .
 - $L_k : \mathcal{G}(\Omega_k) \rightarrow \mathcal{G}(\Omega_k)$. L_k is the discretizations of L from Eq.10.5 on Ω_k . Eq.10.5 then reads $L_\ell u_\ell = f_\ell$.
 - Smoothing operator: $S_k : \mathcal{G}(\Omega_k) \rightarrow \mathcal{G}(\Omega_k)$. The operator S_k denote the linear operation of given smoothing method (for example, one iteration of Eqs. 10.4). Applying ν *smoothing steps* to discrete problem of the form $L_k u_k = f_k$ with initial approximation w_k . $\bar{w}_k = \text{SMOOTH}^\nu(w_k, L_k, f_k)$.
 - Restriction operator: $I_k^{k-1} : \mathcal{G}(\Omega_k) \rightarrow \mathcal{G}(\Omega_{k-1})$ is a transfer operator for coarsening i.e. the grid transfer between the Ω_k with discretizations h and $2h$ -grid Ω_{k-1} .
 - Interpolation operator: $I_k^{k-1} : \mathcal{G}(\Omega_{k-1}) \rightarrow \mathcal{G}(\Omega_k)$ is a transfer operator for prolongation i.e. the grid transfer between the Ω_{k-1} with discretizations $2h$ and h Ω_k .
- ν_1 and ν_2 define the number of **pre-smoothing and post-smoothing steps** respectively.
- **Cycle index** γ specifies the number of cycles to be carried out on the current grid level, as displayed on Fig. 10.2 and Fig. 10.3.

Next we will use the definitions of the components from the previous page to describe a typical multigrid cycle. In each multigrid cycle, a calculation of a new iterate solution u_k^{m+1} from a given u_k^m will proceed according to the following recursive algorithm:

Multigrid cycle $u_k^{m+1} = MGCYC(k, \gamma, u_k^m, L_k, f_k, \nu_1, \nu_2)$

1. Presmoothing

- Compute approximation \bar{u}_k^m by applying ν_1 smoothing steps to u_k^m

$$\bar{u}_k^m = SMOOTH^{\nu_1}(u_k^m, L_k, f_k).$$

2. Coarse grid correction

- Compute the defect $\bar{d}_k^m = f_k - L_k \bar{u}_k^m$.
- Restrict the defect $\bar{d}_{k-1}^m = I_k^{k-1} \bar{d}_k^m$.
- Compute an approximate solution \hat{v}_{k-1}^m of the defect equation on Ω_{k-1}

$$L_{k-1} \hat{v}_{k-1}^m = \bar{d}_{k-1}^m \tag{10.9}$$

by

- $k = 1$, use a direct or fast iterative solver for Eq.10.9.
- $k > 1$, solve Eq. 10.9 approximately by performing γ k -grid cycles using the zero grid (coarsest grid) function as a first approximation.

$$\hat{v}_{k-1}^m = MGCYC^\gamma = (k-1, \gamma, 0, L_{k-1}, \bar{d}_{k-1}^m, \nu_1, \nu_2).$$

- Interpolate the correction $\hat{v}_k^m = I_{k-1}^k \hat{v}_{k-1}^m$.
- Compute the corrected approximation on Ω_k $u_k^{m,after,CGC} = \bar{u}_k^m + \hat{v}_k^m$.

3. Postsmoothing

- Compute u_k^{m+1} by applying ν_2 smoothing steps to $u_k^{m,after,CGC}$:

$$u_k^{m+1} = SMOOTH^{\nu_2}(u_k^{m,afterCGC}, L_k, f_k).$$

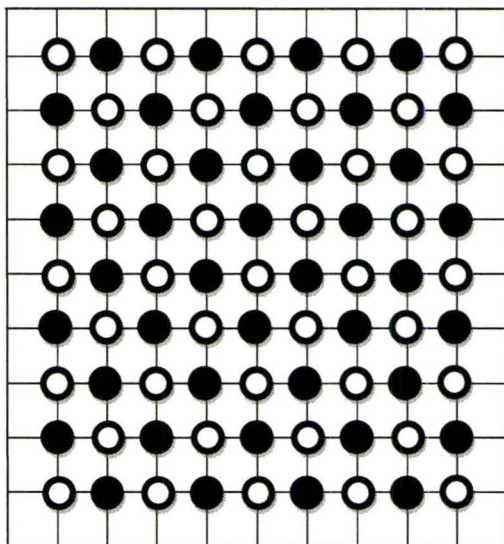


Figure 10.4: Red-black distribution of grid points.

To solve Eq. 8.1 by multigrid, we used a so-called full approximation scheme (FAS) [117, 118]. The idea behind FAS is similar to the linear multigrid described above. The main difference is in the treatment of nonlinear terms. The nonlinearity is treated using one step of Newton's iteration. Details of the FAS numerical scheme multigrid cycle are given in Appendix C. The first step is applying ν_1 presmoothing steps. The Gauss-Seidel method with red-black ordering is used as a smoothing formula in our implementation of the multigrid method. One of the advantages of this method is that relatively fewer steps (as compared to other methods) are needed to smooth the error. Moreover red-black ordering formula is easier to implement in a parallel environment i.e. solved on multiple computers. This will be necessary to study large system as it is in our case. In a red-black ordering scheme the grid points are divided into two groups – red and black (Fig. 10.4). The scheme is then executed in two half-steps. The first step updates the red points and the second step updates all black points using the values from the previously updated red points. The details of smoothing operator are outlined in Appendix C, Eq. C.6.

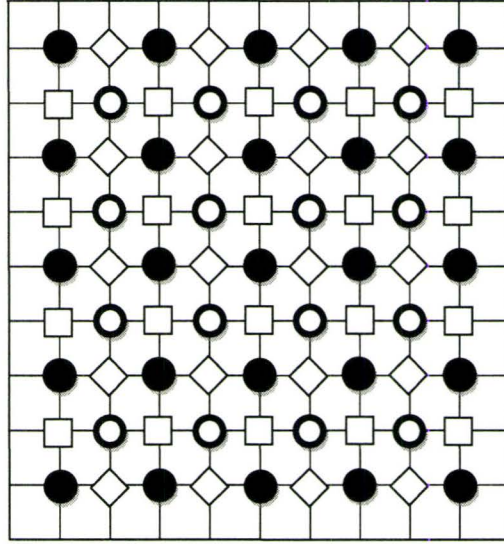


Figure 10.5: Bilinear interpolation used for the transfer to finer grid from the coarse grid marked by full circles. Numerics are given by the following stencils depending on the position of the calculation in the mesh. Full Circle: $I_{2h}^h \hat{v}_{2h}(x, y) = \hat{v}_{2h}(x, y)$, Box: $I_{2h}^h \hat{v}_{2h}(x, y) = 0.5[\hat{v}_{2h}(x, y + h) + \hat{v}_{2h}(x, y - h)]$, Diamond: $I_{2h}^h \hat{v}_{2h}(x, y) = 0.5[\hat{v}_{2h}(x + h, y) + \hat{v}_{2h}(x - h, y)]$, Empty Circle: $I_{2h}^h \hat{v}_{2h}(x, y) = 0.25[\hat{v}_{2h}(x + h, y + h) + \hat{v}_{2h}(x - h, y - h) + \hat{v}_{2h}(x + h, y - h) + \hat{v}_{2h}(x - h, y + h)]$.

In the second step, a *full weighting* restriction operator was applied to map h grid Ω_k to $2h$ grid Ω_{k-1} . Applying this operator to a grid function in two dimensions $d_h(x, y)$ means

$$d_{2h} = I_h^{2h} d_h(x, y) = \frac{1}{16} [4d_h(x, y) + 2d_h(x + h, y) + 2d_h(x - h, y) + 2d_h(x, y + h) + 2d_h(x, y - h) + d_h(x + h, y + h) + d_h(x + h, y - h) + d_h(x - h, y + h) + d_h(x - h, y - h)] \quad (10.10)$$

which is a nine-point weighted average. To interpolate back from the $2h$ Ω_{k-1} grid to the h grid Ω_k , *bilinear operator* was used (see Fig. 10.5 for details).

In addition to the numerical efficiency of the multigrid, an advantage from a scientific point of view is the representation of the solution on different grids with changing resolution. As shown in the right portion of Fig. 10.1, the finest mesh contains detailed information on the atomistic structure while coarse grids carry in-

formation about grain boundaries and other higher-scale microstructural components.

10.3 Convergence and Efficiency of Multigrid Solver

In this section, we will study the convergence and efficiency of the Full Approximation Multigrid Scheme as outlined in previous section.

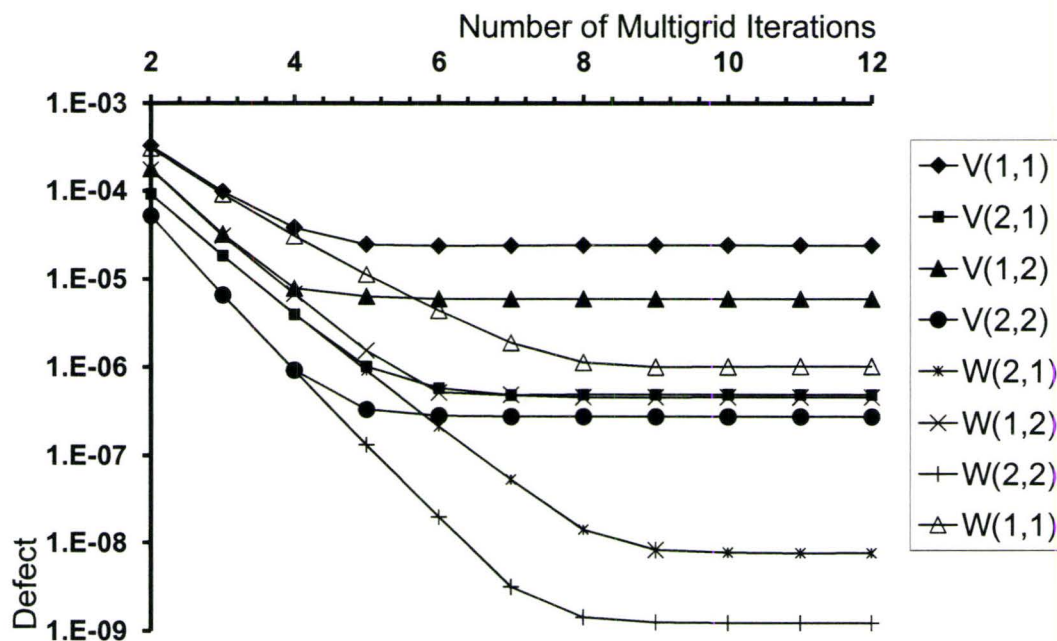


Figure 10.6: The convergence history of different multigrid cycles for MPFC model. V denotes a V-cycle and W a W-cycles, while the bracketed integers denote (ν_1, ν_2) described in text.

Multigrid convergence is closely related to the defect equation, which is an equation for the error in terms of the defect. By measuring the value of the defect (usually in terms of L_2 norm) between multigrid iteration cycles, we can determine if the defect is reduced (i.e. multigrid method converges). Convergence depends on the main input parameters of the multigrid mentioned in the previous section. It depends on the shape of the cycle (V or W) defined by the cycle index γ and the number of pre-smoothing and post-smoothing steps ν_1 and ν_2 . An example of typical notation for a multigrid cycle would be $V(0, 1)$, meaning $\gamma = 1$ with no presmoothing steps

Multigrid Cycle	Iteration Steps	Time [sec]
$V(2, 1)$	5	2.45
$V(2, 2)$	4	2.47
$W(2, 1)$	5	7.02
$W(2, 2)$	4	7.11

Table 10.1: Wall clock times and number of iterations for a defect reduction of a factor 10^{-6} for different cycles when solving for Eq. 8.1.

and one post smoothing step. Another example, $W(2, 1)$, would mean a W cycle with $\gamma = 2$, $\nu_1 = 2$ and $\nu_2 = 1$. In Fig. 10.6, the defect is plotted as a function applied to multigrid cycles for a number of combinations of V and W cycles. The figure suggests rapid convergence of the multigrid for cycles $V(2, 1)$, $V(2, 2)$, $W(2, 1)$, and $W(2, 2)$. They reduce the defect by a factor of 10^{-6} to 10^{-9} within 6 multigrid iterations. Also, the benefits of processing the coarse grid levels more frequently is evidenced by much better convergence of W-cycles.

In order to choose the most efficient solver, it is necessary to look at both its convergence speed and cost. In practice, the 'real time' needed to achieve the solution is the most interesting value. Table 10.1 shows wall clock times and number of iterations for a defect reduction of a factor 10^{-6} for different cycles. The times were measured during above convergence measurements and were done on the same computer work station. The table gave us a different point of view when considering convergence data. Both W cycles ($W(2, 1)$ and $W(2, 2)$) have the best convergence however, in the wall time measurements they appeared to be the slowest, with calculation times almost 3 times bigger the V cycles ($V(2, 1)$ and $V(2, 2)$). This measurement played a significant role in choosing the $V(2, 1)$ multigrid cycle as our main option for the large deformation simulations described in the following chapter.

In the last numerical experiment shown here, we compared the complexity (number of arithmetic operations as a function of grid size) of the multigrid with a more traditional iterative solver. Figure 10.7 gives a comparison of the complexity of 2 solvers, the successive overrelaxation (section 10.1) and the multigrid method described above. We plotted the number of operations against the grid size (i.e. total number of unknowns in the discrete system in Eq. 10.4), then calculated a trend for each solution method. We found that the multigrid follows the theoretical

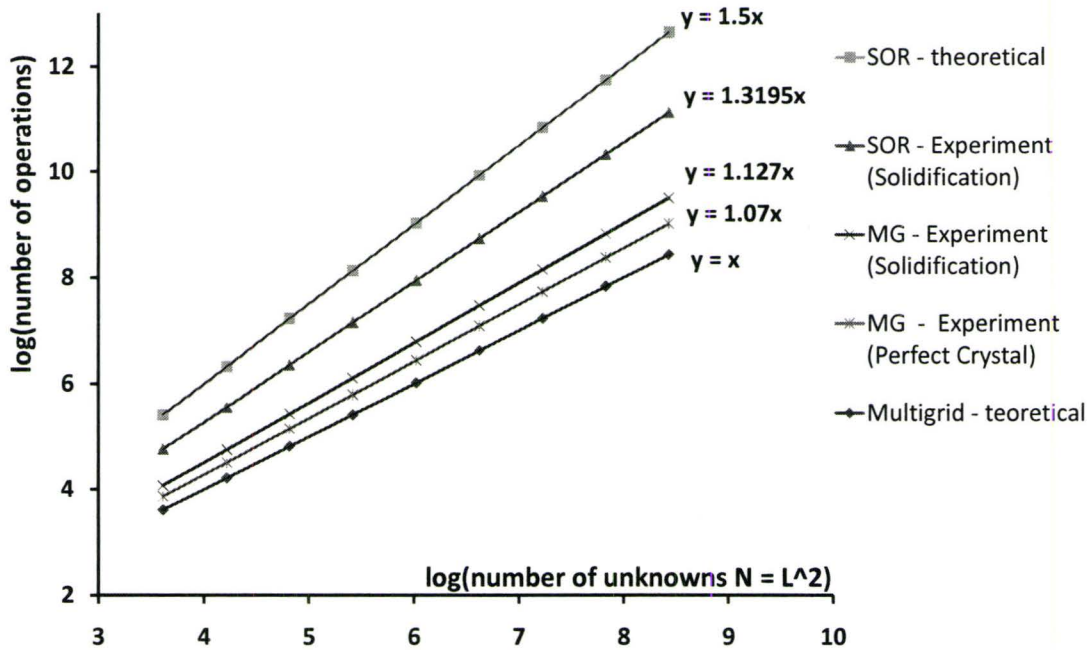


Figure 10.7: Complexity of successive overrelaxation (SOR) and multigrid (MG) method. Both methods are solving model Eq. 8.1 The top and bottom lines represent the theoretical complexity for the SOR and multigrid approaches, respectively. SOR and multigrid are further compared during the solidification simulation experiment where the iterative method increases the number of operations with increasing sample size by a factor of 1.3, while multigrid method increases the same by a factor of 1.1. The performance of the multigrid approach improved when simulating a deformation in a perfect crystal. In this case, the number of operations increased 1.07 times with the number of computational nodes.

slope of 1 closely, which means that the number of operations in our multigrid solver increased linearly with the number of computational nodes. This was not the case in the successive overrelaxation method, where the number of operation grew 1.32 times along with the size of the grid. Moreover the slope of the multigrid curves depended on initial conditions and the type of the simulated problem. For example, solidification simulations were slower than those of perfect crystal deformations.

Part III

Application of Phase Field Crystal Modeling to the Study of Strengthening Mechanisms

This part of the thesis applies the Modified Phase Field Crystal Model outlined in chapter 8 to study deformations, deformation processes, and strengthening mechanisms in nanocrystalline materials. We will first outline the dynamics of individual dislocations and strain distribution in NC samples. That is to be followed by a discussion on the strength dependence of a grain size in polycrystalline materials on a nanoscale. Finally, the binary alloy model derived in chapter 9, coupled to dynamical equations of motion derived in section 9.6, is used to demonstrate the effect of dislocation motion in spinodal decomposition.

Chapter 11

Deformation of Nanocrystalline Materials

In this chapter we will first study dislocation glide in a single crystal sample. A single dislocation velocity is measured and plotted as a function of applied shear strain rate. Then the stress distribution in a double notch sample under uniaxial tension is compared with experimentally observed values. Finally, we will study series of polycrystalline samples with different grain sizes under uniaxial tensile load to explore their deformation mechanisms and strength. We will begin by discussing the initial conditions, boundary conditions, and set up of our simulations.

11.1 Initial Conditions and Boundary Conditions

An example of the simulation setup is displayed on Fig. 11.1. For all samples, periodic boundary conditions in all directions were used. As shown in the figure, the solid sample with the hexagonal crystal structure was placed in the pool of liquid surrounding it from both or all four sides depending on the type of simulation. This was done by choosing values of r and ρ_0 from the coexistence region between hexagonal solid and liquid of the phase diagram on Fig. 7.4. Using a lever rule the amounts of liquid and solid in the simulated sample were set such that no crystallization or melting would occur.

The set-up for the dislocation glide simulations shown on Fig. 11.1 required the placement of a single dislocation into the center of the sample. This was done by

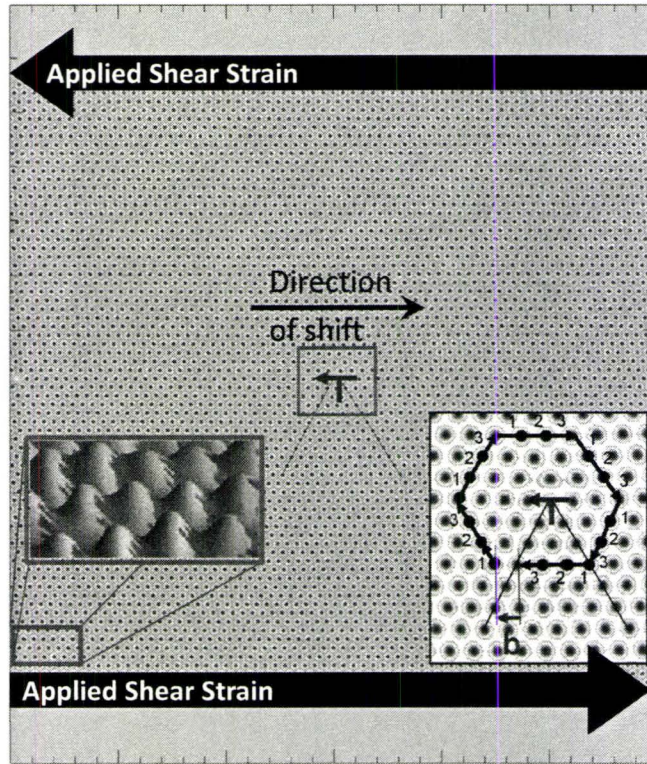


Figure 11.1: A portion of the sample used to examine dislocation glide velocity. Parameters used: $(r, \rho_0, \Delta x, \Delta t, \alpha, \beta) = (-1, 0.49, \pi/4, 0.001, 15, 0.9)$.

introducing one 'extra' row of atoms into the bottom part of the sample. Specifically, the top part of the crystal initially contained N atoms and the bottom part, $N+1$. Initial conditions for the crystalline part were set by setting the density in the form of a single mode approximation of the hexagonal crystal structure, expressed previously by Eq. 7.25 and Eq. 7.27.

To prepare polycrystalline samples containing grains with various orientations, seeds with hexagonal symmetry (Eq. 7.25) and random orientations were placed into the undercooled liquid, similar to the simulation of polycrystalline nucleation and growth discussed in section 8.4. Initial seeds were grown at high dimensionless temperature, $r = -0.3$ in the phase diagram on Fig. 7.4, to prevent the formation of faceted grain boundaries. Fully grown samples were then used to prepare tensile samples by placing portions of the 'high temperature' sample into the coexistence region at the low temperature ($r = -0.6$ in phase diagram on Fig. 7.4). As a result,

we obtained polycrystalline samples surrounded by liquid from all sides. The number of initial seeds defined the final number of grains and thus the average grain size, once a simulation box size was selected.

After the simulation set-up, all samples were left to equilibrate until the free energy did not change with time, for example Fig.8.1e.

11.2 Strain Application

Samples were deformed by shear strain (Fig. 11.1) or uniaxial tensile load (Fig. 11.7) by applying traction boundary conditions. We incorporated traction boundary conditions in the phase field crystal model using new penalty term [19]. The penalty term is a positive definite term in the free energy of Eq. 7.17. It is the square of the difference of the density field and the imposed density field ρ_{surf} comprising an external surface. To emulate the boundary traction – or the traction at specific locations in the sample – the penalty term is modulated by a function $M(\vec{x})$, which is zero outside the zone where the traction is being applied. Recall free energy as defined in Eq. 7.17.

$$\mathcal{F} = \int d\vec{r} \left(\frac{\rho}{2} [a\Delta T + c(k_0^2 + \nabla^2)^2] \rho + u \frac{\rho^4}{4} \right)$$

By adding a penalty term in the form of $M(\vec{x})(\rho - \rho_{surf})^2$ we will get free energy in the form:

$$\mathcal{F} = \int d\vec{r} \left(\frac{\rho}{2} [a\Delta T + c(k_0^2 + \nabla^2)^2] \rho + u \frac{\rho^4}{4} + M(\vec{x})(\rho - \rho_{surf})^2 \right) \quad (11.1)$$

The modified free energy Eq. 11.1 can be used without modifying the original phase diagram. To study single-crystal deformations, the shape of surface density ρ_{surf} is in the form of a single mode approximation of the hexagonal crystal structure (Eq. 7.25 and Eq. 7.27). To accommodate various crystal orientations in the case of polycrystalline materials the surface function was in the form of series of gaussians in two dimensions creating periodic field fitting the density of the original hexagonal lattice,

$$\rho(x, y) = A \exp(-\sigma((x - G_1(x))^2 + (y - G_1(y))^2)) + \quad (11.2)$$

$$A \exp(-\sigma((x - G_2(x))^2 + (y - G_2(y))^2)) + \dots \\ + A \exp(-\sigma((x - G_n(x))^2 + (y - G_n(y))^2))$$

In Eq. 11.2, A is the amplitude (Eq. 7.27), vectors $G(x,y)$ are locations of the peaks in the density field ρ_{surf} , σ sets the width of peaks, and n is the total number of peaks in the boundary field.

11.3 Strain Rates

Strain rates used in our simulation ranged from $10^{-5}/t$ to $10^{-3}/t$, where t is expressed in dimensionless units of time. To estimate strain rates in physical units, we matched the experimentally known vacancy diffusion coefficient of metals near the melting point to the one calculated for the MPFC model. The vacancy diffusion coefficient for typical metals such as Cu is in the range of 10^{-8} to $10^{-13} \text{cm}^2/\text{sec}$ [119]. An effective diffusion coefficient for PFC model was calculated from density profiles in Ref. [15]. Using an example for copper at $1063 \text{ }^\circ\text{C}$, $D_{vCu} = 10^{-9} \text{cm}^2/\text{s}$, $a_{Cu} = 3.6 \text{ \AA}$ and matching it to the model at the dimensionless temperature of $r = -0.8$, the vacancy diffusion coefficient was expressed in [17] as:

$$D_v = \frac{1.78a_{Cu}^2}{t}. \quad (11.3)$$

In the MPFC model, the effective vacancy diffusion is modified by the effective speed of sound α and the diffusion related coefficient β , Eq. 8.11. Equation 11.3 then becomes:

$$D_v = \frac{\alpha^2 1.78a_{Cu}^2}{\beta t}. \quad (11.4)$$

Thus, the applied strain rates in our simulations convert to the range of $0.01/s$ to $0.005/s$.

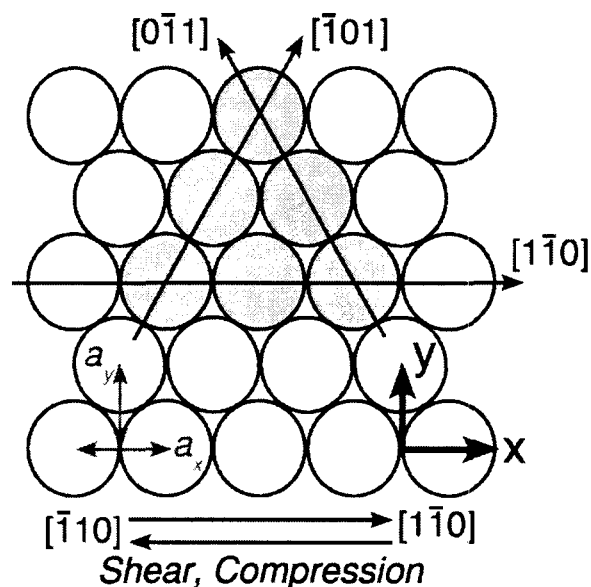


Figure 11.2: A portion of atoms in a (111) plane in face centered cubic crystal or (0001) basal plane in hcp crystal.

11.4 Crystal Structure

The triangular lattice used in our simulations can be related to a $\{111\}$ family of planes in face centered cubic (fcc) crystal (Fig. 11.2) or $\{0001\}$ family of basal planes in hexagonal close packed (hcp) structure. Slip will occur in $\langle 110 \rangle$ type directions in an fcc crystal and $\langle 11\bar{2}0 \rangle$ in an hcp structure. In both cases, only three slip systems will operate in two dimensions (2D). One should also note that a stacking fault with the structure $ABAB|BABA$ has very high potential energy in 2D hexagonal lattice. As a result of the high stacking fault energy, dislocations in 2D systems do not dissociate into partials or extended dislocation as in the three dimensional fcc case [120].

11.5 Strain Measurements and Data Interpretation

Strain in the sample and the position of the dislocations were identified by locating peaks in the density field $\rho(x, y)$. Peaks in the density field correspond to a location of atoms in the real material or MD simulation. If the atom has all six

neighbors, it is identified as part of a perfect crystal structure. If the atom had less than six neighbors it is identified as an atom neighbouring with a dislocation. By recording the position of the dislocation with time, we were then able to calculate the velocity of the dislocation.

The average shear strain was calculated from the position of the peaks in $\rho(x, y)$ by noting that, in a well equilibrated single crystal sample, each particle has another particle located in a vertical distance of $2a_y$ (Fig.11.2). If the particle is shifted in the x direction by a distance dx , then the measured shear strain will be $dx/2a_y$. Repeating the calculation for all N 'atoms' (peaks in the density field) will give the average shear strain of the sample.

$$\bar{\gamma} = \frac{1}{2Na_y} \sum_{i=1}^N dx_i \quad (11.5)$$

A similar approach was taken when the average strain was measured in a polycrystalline sample. Here however the situation differed by the presence of multiple crystal orientations in the sample. In this case, we calculated the average strain by comparing the distance of the next nearest neighbors to that of a perfect crystal lattice parameter a_x . If the distance of two nearest neighbors increased by da_x , the strain was then calculated as da_x/a_x . The calculation was then repeated over all six neighbors and the average was taken as $d\bar{a}_x = (da_{x1} + da_{x2} + \dots + da_{x6})/6$. Again, this calculation was repeated over all N particles in the sample as in the previous case and the average strain in the sample was calculated

$$\bar{\epsilon} = \frac{1}{6Na_x} \sum_{i=1}^N d\bar{a}_{xi}. \quad (11.6)$$

11.6 Dislocation Glide

To uncover deformation processes in nanocrystals simulated by our phase field crystal methodology, we first examined the dynamics of individual dislocations. After the sample is equilibrated an edge dislocation formed and a constant shear strain rate was applied (Fig. 11.1). The time-averaged dislocation glide velocity \bar{v} was found to be a linear function of the strain rate $\dot{\gamma}$, consistent with classical dislocation theory

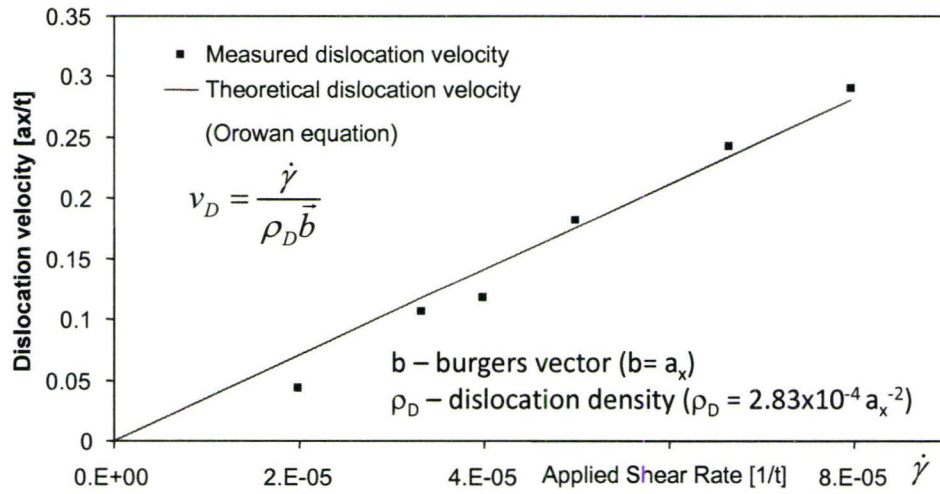


Figure 11.3: Dislocation glide velocity vs. applied strain rate.

(Fig. 11.4). This theory predicts that

$$\bar{v} = \frac{\dot{\gamma}}{\rho_d b}, \quad (11.7)$$

where ρ_d is the dislocation density and b is the magnitude of the Burger's vector [121].

To elucidate the local dynamics of individual dislocations, we computed the average strain in the crystal as a function of time for different strain rates. The first observation on Fig. 11.4 is the linear build-up of elastic strains in the sample before the dislocation slip. This observation once again shows a correct elastic response of the MPFC model to the applied strain. Further results, shown in Fig. 11.4, revealed two regimes of dislocation glide. The first was characterized by continuous glide (observed at large $\dot{\gamma}$) and the second by a stick-slip gliding of the dislocation at low $\dot{\gamma}$. In both cases the applied plastic strain was relieved by the motion of the dislocation, and the time-averaged strain remained constant.

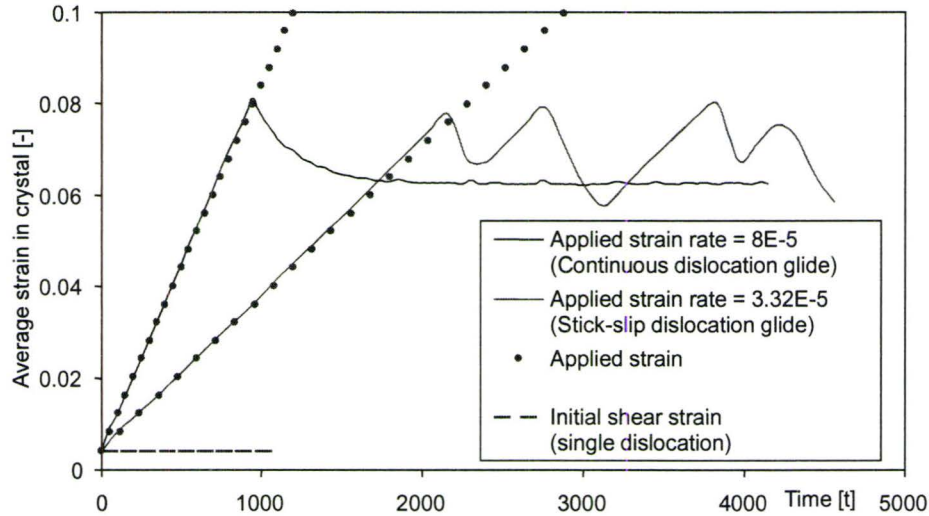


Figure 11.4: Two regimes of dislocation glide. For high strain rates ($\gamma = 8 \times 10^{-5}/t$), we observed continuous glide, while at lower strain rate ($\gamma = 3.32 \times 10^{-5}/t$), the dislocation set into a stick-slip motion.

11.7 Modeling Strain Concentration and Fracture of Nanocrystals

To further demonstrate the properties of the MPFC model, the effect of uniaxial tension in a notched sample was examined. Before we proceed, let us introduce basic terminology with the example of a circular hole in an infinite plate as plotted on Fig. 11.5.

When uniaxial tensile stress is applied to the plate, stress distribution will vary with location in the sample. It can be shown analytically that the stress σ_{yy} will vary with the distance from the center of the hole x and will be also a function of the hole diameter $2a$. The variation of σ_{yy} is given by $\sigma_{yy} = \sigma(1 + a^2/2x^2 + 3a^4/2r^4)$ [123]. We see that when $x = \infty$, σ_{yy} becomes equal to applied stress and when $x = a$, $\sigma_{yy} = 3\sigma$. The redistribution of the stress around the hole thus caused the development of the stress three times bigger than the applied stress. The hole acts as a *stress concentrator* with an *elastic stress concentration factor* of 3.

Let us consider a double notched sample with geometry shown in Fig. 11.6a. Notches in the sample, similar to the previous example, will act as stress concentrators and have a significant effect on the stress distribution around them. It is

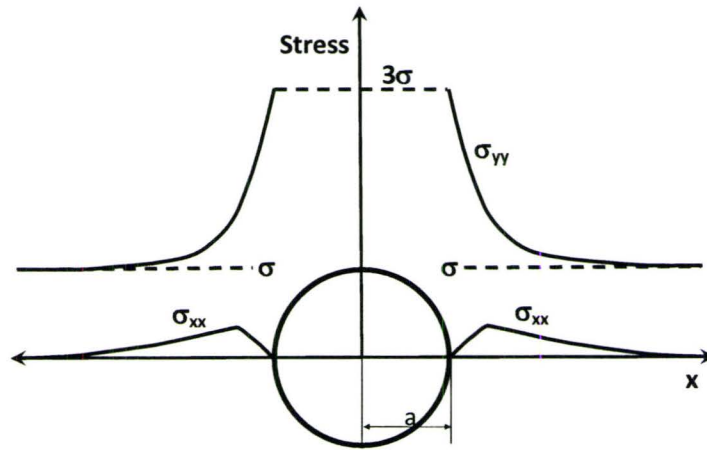


Figure 11.5: Distribution of stress around circular hole in an infinite plate, subjected to a uniform stress, σ .

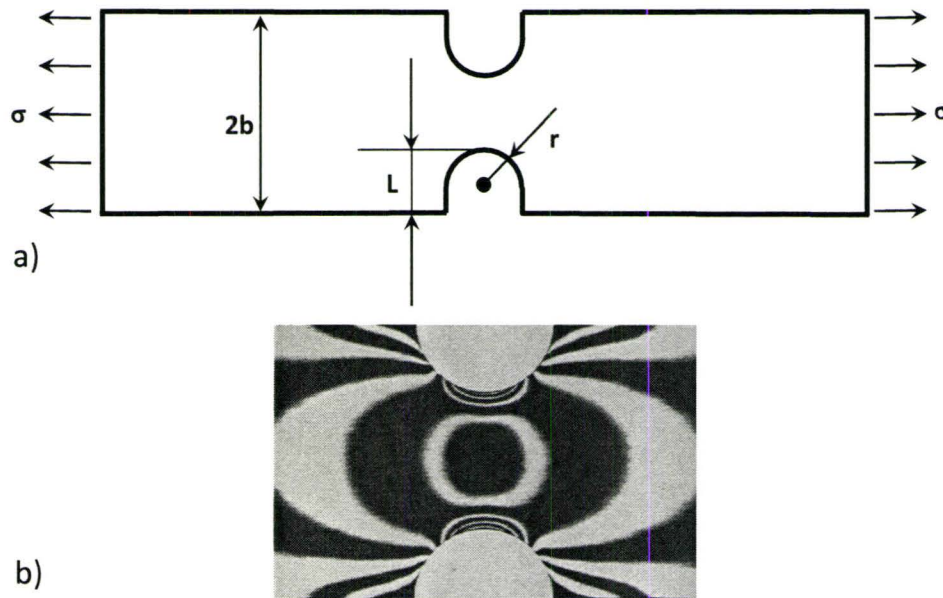


Figure 11.6: a) Geometry of the double U-notched sample used in the present test. b) Elastic stress distribution in a double notch sample measured by photoelasticity [122].

difficult to calculate stress distribution analytically for this case. However, a series of experimental measurements, such as the one shown in Fig. 11.6b, provided us with good estimates for stress concentration factors and other authors developed very accurate empirical formulas of the stress distribution [124]. Using the geometry as displayed on Fig. 11.6a and values from our simulation geometry (Fig. 11.7, $L = 4.5a_x, 2b = 22a_x, r = 4.5a_x$), we expect an elastic stress concentration factor $K_t = 1.79$ using the following formula

$$K_t = \left[0.78 + 2.243\sqrt{\frac{L}{r}} \right] \left[0.993 + 0.18\frac{L}{b} - 1.06\left(\frac{L}{b}\right)^2 + 1.71\left(\frac{L}{b}\right)^3 \right] \left(1 - \frac{L}{b}\right) \quad (11.8)$$

The results of our simulation, plotted in Fig. 11.7, show that strain in a notched sample concentrated appropriately near the notches, as expected from linear elasticity theory. The result qualitatively agreed with an example photoelastic measurement on Fig. 11.6b. We then treated the case as a double notched plate with applied uniaxial stress and calculated the elastic stress concentration factor as $K_t = \sigma_{yy}^{max} / \sigma_{yy}^0$. We found a good quantitative agreement between the theoretical result in Eq. 11.8 and our simulation result 1.81.

It is noteworthy that a simulation with the PFC model (Eq. 7.32) performed for the same system and using an affine transformation to approximate the strains in the sample, failed to produce the expected strain concentration. We also note that while the strains can be extracted in a straightforward manner (section 11.5), elastic stresses are currently obtained only within linear elasticity, as the nonlinear elastic properties of the PFC model have not been fully explored. This should be contrasted with MD, where the stresses in the crystal can be determined from e.g. the virial theorem, even in the nonlinear elastic regime.

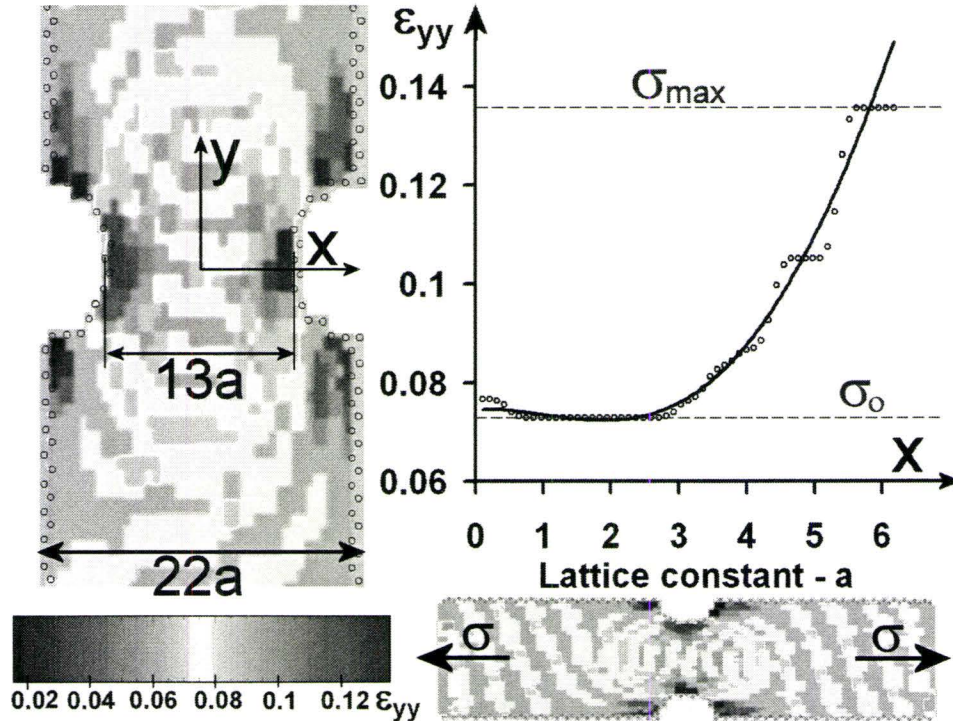


Figure 11.7: MPFC simulation of strain concentration in a double notched sample under a uniaxial tension. **Left:** A strain map of the center portion of the sample displayed at the bottom. Boundary atoms are highlighted as dark blue circles. **Right:** Plot represents a strain profile from the center of the sample into the root of the notch. The solid line is a guide to the eye.

11.8 Deformation in Polycrystalline Material

In previous sections we applied the MPFC model to deformations of single crystal samples. We showed that strains are correctly distributed when load is applied and dislocation behaviour follows theoretical and experimental observations. In this section we will study deformation mechanism and strength of polycrystalline samples for various average grain sizes. More specifically, we will focus on the phenomenon of the reverse Hall-Petch effect discussed in chapters 3 and 4. The Hall-Petch relationship (Fig. 3.1) predicts increasing yield stress with decreasing grain size. However, experimental results and MD computational simulations (section 3.2) paint a different picture for grain sizes below 50nm. As seen from Fig. 3.5, the strength in NC regime was shown to increase, decrease or plateau as a function of grain size, at the lowest

grain size level. Difficulties in sample preparation are the most often cited reason for inconsistency in experimental results. The computational approach offers the potential of preparing defect free samples and study the deformation processes during the course of deformation, which is usually prohibited in experimental work. The MD simulations discussed in section 3.2 have been used as a tool to study the deformation processes on a nanoscale. However, MD simulations were able to produce only very short simulations due to their limitation on time step in picoseconds. In this section, we circumvent the shortcomings of MD simulations using the MPFC model, which operates on time scales several orders of magnitude longer than MD simulations (section 8.1). To study samples with multiple grains, relatively large system sizes had to be used, necessitating the use of the multigrid solver described in chapter 10.

Samples

As described in section 11.1, samples were grown by heterogeneous nucleation and this growth introduced nucleation sites with various grain orientations. To facilitate the analysis of the simulations, we identified which atoms were located at the grain boundaries, around dislocations, or inside the grain by determining local crystalline order. Atoms in perfect hexagonal order (6 nearest neighbours) are considered to be inside a perfect crystal, while those with less than 6 nearest neighbours are considered to be at the grain boundary or near the dislocation. A fully developed grain boundary network structure with various grain orientations, including low angle and high angle grain boundaries, is displayed on Fig. 11.8b. Individual dislocations inside the grains are highlighted in Fig. 11.8b.

To save computational time we studied polycrystalline nanocrystalline samples of two sizes; ($1025\Delta x \times 1025\Delta x$) containing grains with smaller average grain size, and $2049\Delta x \times 2049\Delta x$, used for larger grain sizes. The first sample holds approximately 20000 atoms and the second sample holds approximately 80000 atoms. If we again use the example of copper, where the lattice parameter is 3.6\AA , the sample sizes are approximately $50 \times 50\text{nm}$ and $100 \times 100\text{nm}$, respectively. In total, we prepared 15 samples with grain sizes ranging from 5nm to 30nm. The properties of individual samples are listed in Table:11.1.

Samples of square shape were surrounded by liquid and boundary loads (section 11.2) were then applied to ≈ 30 rows of atoms on two sides. After the equili-

Table 11.1: Samples Overview

Sample number	Sample size [grid size]	Number of grains [-]	Average Grain Size Cu example [nm]
1	1025 × 1025	6	14.88
2	1025 × 1025	15	7.94
3	1025 × 1025	18	7.78
4	1025 × 1025	19	7.67
5	1025 × 1025	30	6.45
6	1025 × 1025	23	6.84
7	1025 × 1025	40	4.97
8	2049 × 2049	10	29.25
9	2049 × 2049	18	21.57
10	2049 × 2049	20	20.42
11	2049 × 2049	37	14.69
12	2049 × 2049	37	14.73
13	2049 × 2049	53	12.06
14	2049 × 2049	54	12.04
15	2049 × 2049	86	9.4

bration of the samples a uniaxial tensile load was applied at a slow constant strain rate $0.001/t$. The simulation setup with parameters of simulations is displayed on Fig. 11.8a. During the simulation free energy was calculated using Eq. 7.17 and density profiles $\rho(x, y)$. The average strain in the sample was calculated for every 2000 time steps.

Samples Above ≈ 12 nm Grain Size

Upon loading, all samples initially deformed elastically as seen from average strain build-up plotted on Fig. 11.14. At about 2 to 3% of deformation, individual dislocations started to glide to relieve applied stress. A typical example of this behaviour are the dislocations A, and C in Fig. 11.9. Dislocations either relaxed towards the sample surface creating a ledge (dislocation A, Fig. 11.9), or were absorbed by a grain boundary (dislocation C, Fig. 11.9). Upon further loading, when all individual dislocations were exhausted, the load is carried only by the grain boundaries. Even the largest grains on a nanoscale are too small for traditional sources (such as the Frank-Read source) to operate. Grain boundaries are the only possible sources of dislocations. We observed low-angle grain boundaries beginning to decay and act as a source of dislocations (dislocation B, Fig. 11.9), thus contributing more gliding dislocations to plastic flow. As the dislocation left the low angle grain boundary, the original grain rotated and was extended onto a neighboring grain, effectively causing a grain growth. On Fig. 11.12, a portion of the sample with a small grain is displayed. At about 4% of deformation, the grain boundary of the displayed grain started to decay by the mechanism of dislocation glide. As a result, the grain rotated about 2° and its diameter decreased.

Samples Below ≈ 12 nm Grain Size

As the grain size decreased, the fraction of the grain boundaries in the sample increased and fewer individual dislocations were observed. Moreover, some individual dislocations were 'trapped' in the center of small grains and were prohibited from gliding. Upon loading, most of the load was immediately transferred to the grain boundaries. Initially, the deformation was accommodated by a series of short gliding events of free dislocations. Similar to behaviour in larger grains, low angle grain boundaries decayed and became sources of mobile dislocations. Contrary to the first case, fracture, and void creation, and growth was observed at triple junctions, crystal surfaces and high-angle grain boundaries. Voids contributed to decrease in strength. Once a nanovoid was nucleated, the resulting stress-free surface of the void caused a localized stress and strain concentration. Free dislocations and dislocations generated from the grain boundaries glided towards the stress concentration around the void to

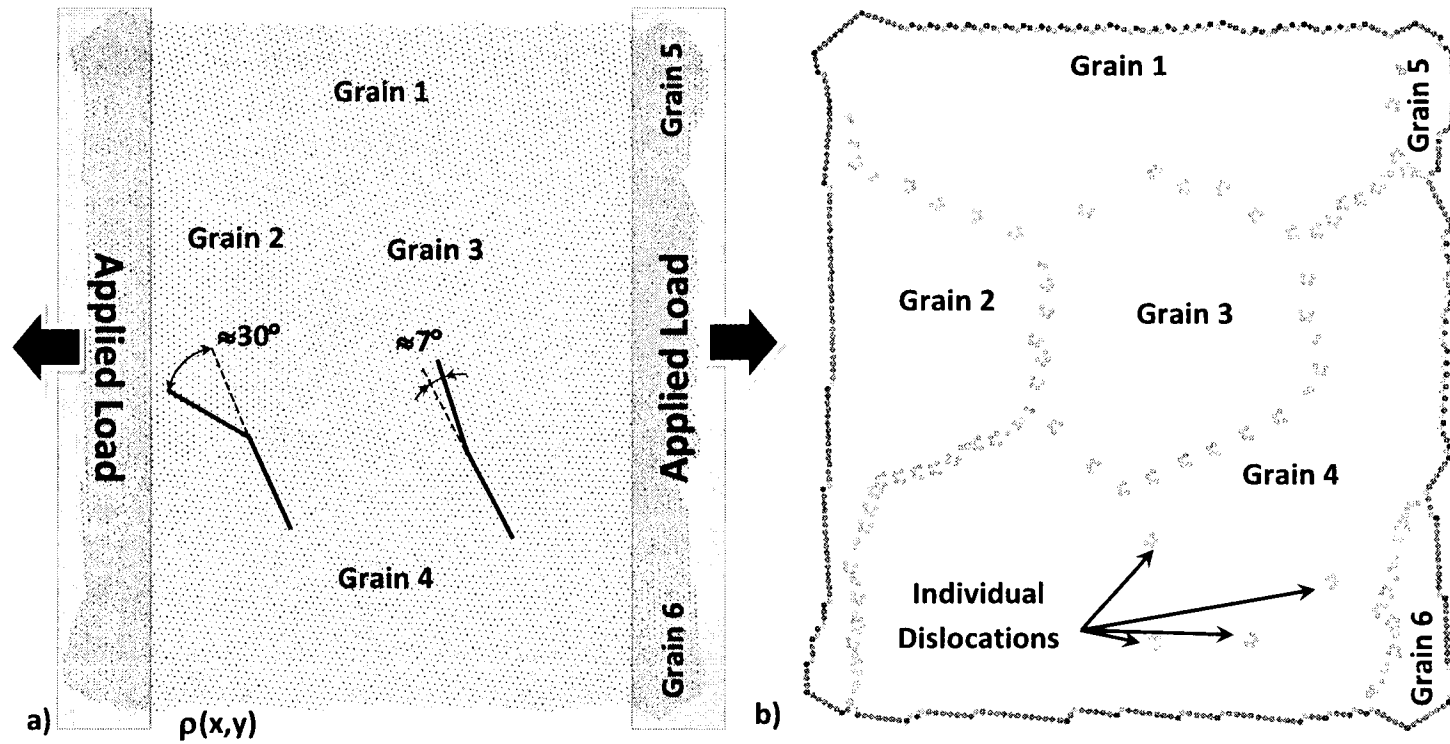


Figure 11.8: Sample number 2 from Tab. 11.1. a) The density field $\rho(x,y)$ is plotted with highlighted angles between two couples of grains. Outline of boundary loads and loading direction is outlined by rectangles and arrows on both sides of the sample. For all simulations in this section the following parameters were used: $(\Delta x, \Delta t, \alpha, \beta, \rho_0, r, \dot{\epsilon}) = (\pi/4, 0.0001, 200, 0.5, 0.45, -0.6, 0.001/t)$. The same sample when only atoms with other than 6 nearest neighbors are shown, thus highlighting the imperfections in the crystals. Grain boundaries and individual dislocations are clearly outlined.

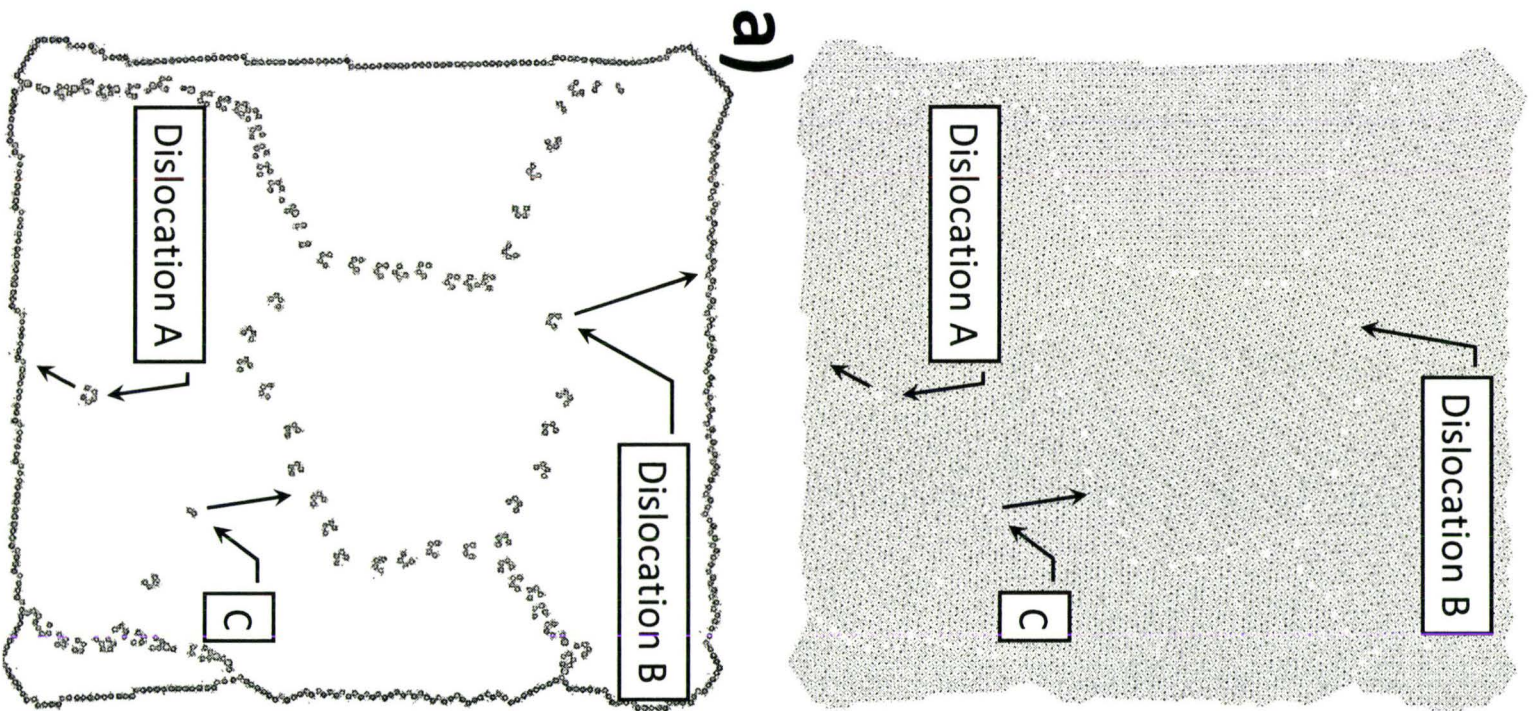


Figure 11.9: Deformation in the $50 \times 50\text{nm}$ sample. Average grain size is 15nm . Dislocations A, C are absorbed by surface or grain boundary respectively. Dislocation B is ejected from the GB and annihilated at the surface. Slides on Figs. 11.9, 11.10, and 11.11 correspond to simulation times $t = 30, 35$ and 40 respectively. Small arrows without labels point to a dislocation trajectory.

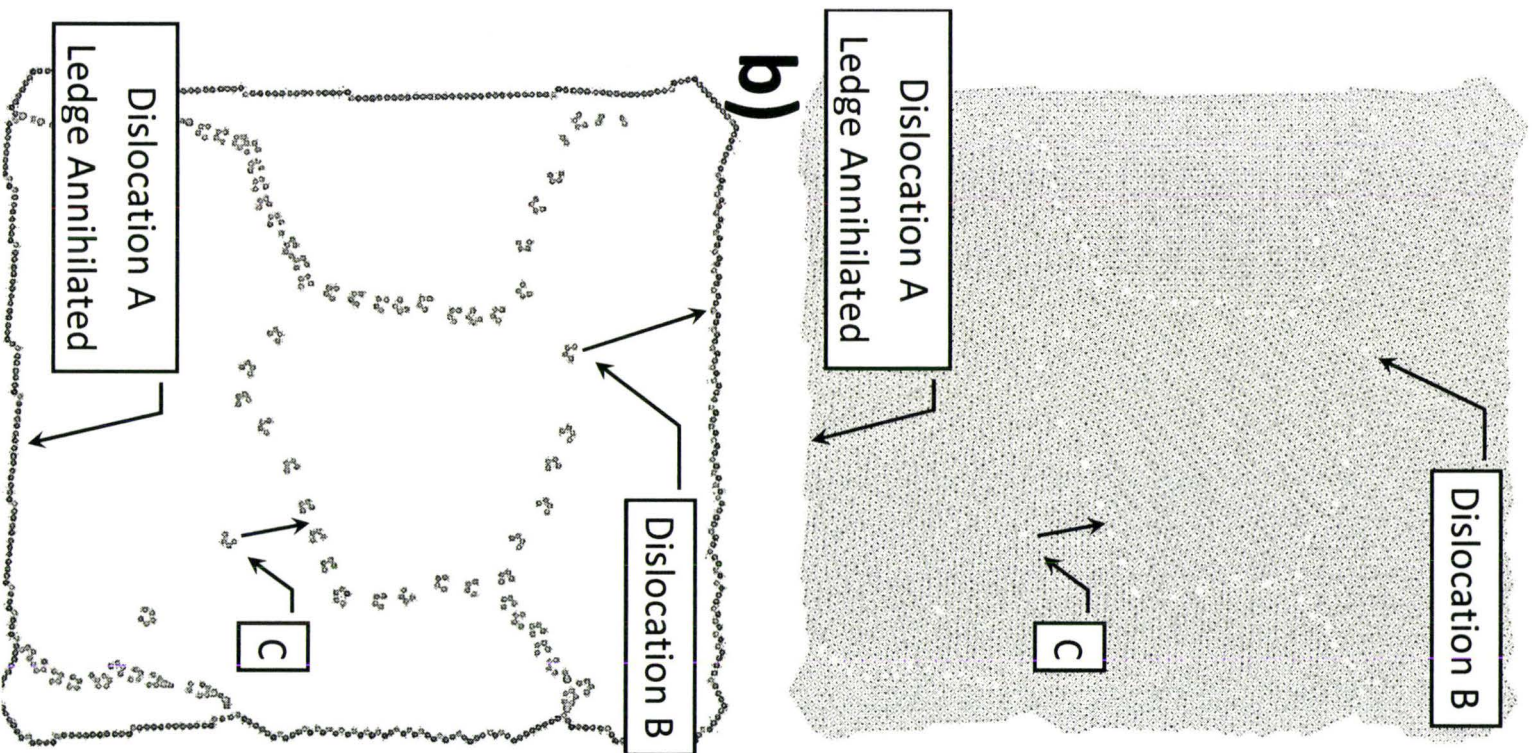


Figure 11.10: Deformation in the $50 \times 50\text{nm}$ sample. Average grain size is 15nm . Dislocations A, C are absorbed by surface or grain boundary respectively. Dislocation B is ejected from the GB and annihilated at the surface. Slides Figs. 11.9, 11.10, and 11.11 correspond to simulation times $t = 30, 35$ and 40 respectively. Small arrows without labels point to a dislocation trajectory.

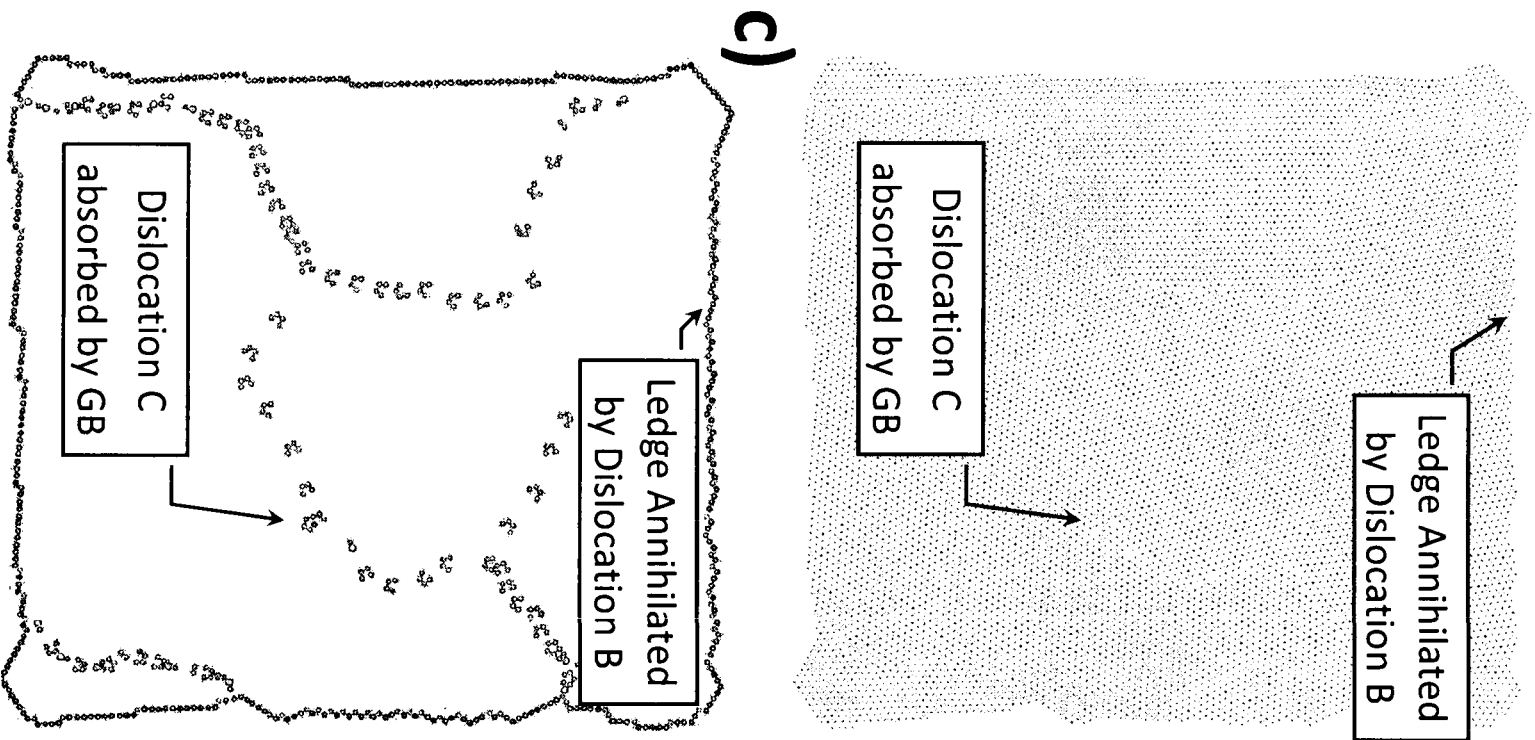


Figure 11.11: Deformation in the $50 \times 50\text{nm}$ sample. Average grain size is 15nm . Dislocations A, C are absorbed by surface or grain boundary respectively. Dislocation B is ejected from the GB and annihilated at the surface. Slides Figs. 11.9, 11.10, and 11.11 correspond to simulation times $t = 30, 35$ and 40 respectively.

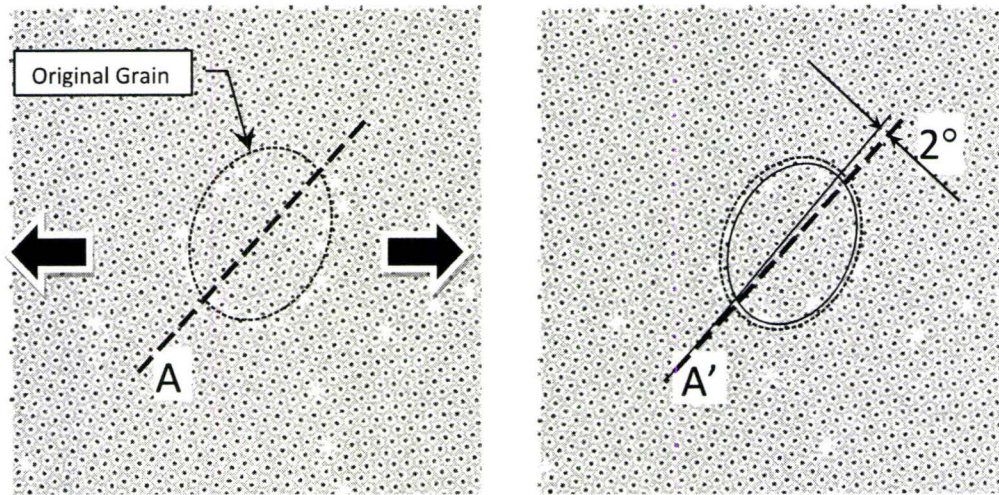


Figure 11.12: Two slides showing a portion of the sample with rotating grain. Initial time is $t=30$ and final time $t=40$. Dashed lines A and A' are parallel. The dotted line shows the original shape of the grain. It is superimposed onto the deformed grain on the right.

relieve the stress. The process can be described as periodic nanovoid growth and nanovoid healing by annihilating dislocations. Once there was no mobile dislocations available in the proximity of the void, the deformation proceeded by void growth and fracture Fig. 11.13.

To analyze the strength, we plotted an average strain in the crystal found by locating peaks in the density field (see section 11.5) against applied strain. A linear relationship was found up to about 2-3% of deformation, suggesting an elastic deformation i.e. on unloading the sample would return to its initial state. After about 3% of deformation, all samples exhibited change in deformation behaviour from elastic to plastic deformation. Plastic deformation proceeded by dislocation glide, grain rotation and fracture, as discussed above. We measured two characteristic values on stress strain curves. The first was a average strain at the yield point which was determined as the intersection between the average strain curve and a line parallel to the linear part of the curve at 0.002 applied strain rate. When average yield strains in the sample were plotted against the grain size, we found an increase in the yield stress with increasing grain size, which suggest a 'reversed' Hall-Petch effect on a nanoscale (Fig. 11.15left). At scales above 15 to 20nm, we found that curve started to plateau suggesting a turn to regular strengthening behaviour. Hall-Petch plot is

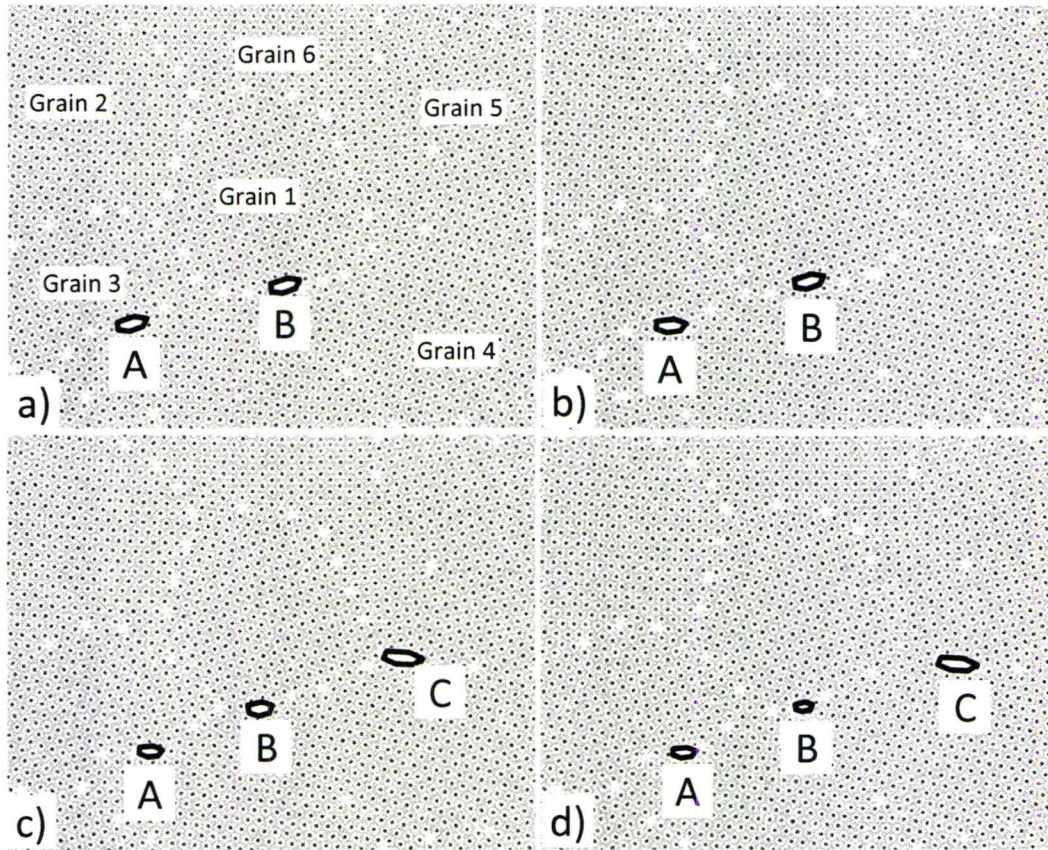


Figure 11.13: Three voids A, B and C are displayed in four consecutive times 25, 35, 45 and 50. Voids A and B are nucleated and continue to grow as simulation proceeds. In the second half (slides c, d) a third void C is nucleated while A and B void almost annihilate. It is also interesting to point out the dynamic nature of the process as the voids are 'gliding' along the grain boundary.

usually plotted as function of $1/\sqrt{d}$, where d is the grain size (Fig. 11.15top right panel). In this case, we found a linear dependence of strength on grain size. Finally we plotted average strain in the sample during the flow to find similar results as in the case of yield strength.

Comparison with Experiments

In our simulation measurements, we observed a decrease in the strength with decreasing grain size in samples with no porosity and on timescales comparable with experimental work. After the initial elastic deformation mode, plastic deformation

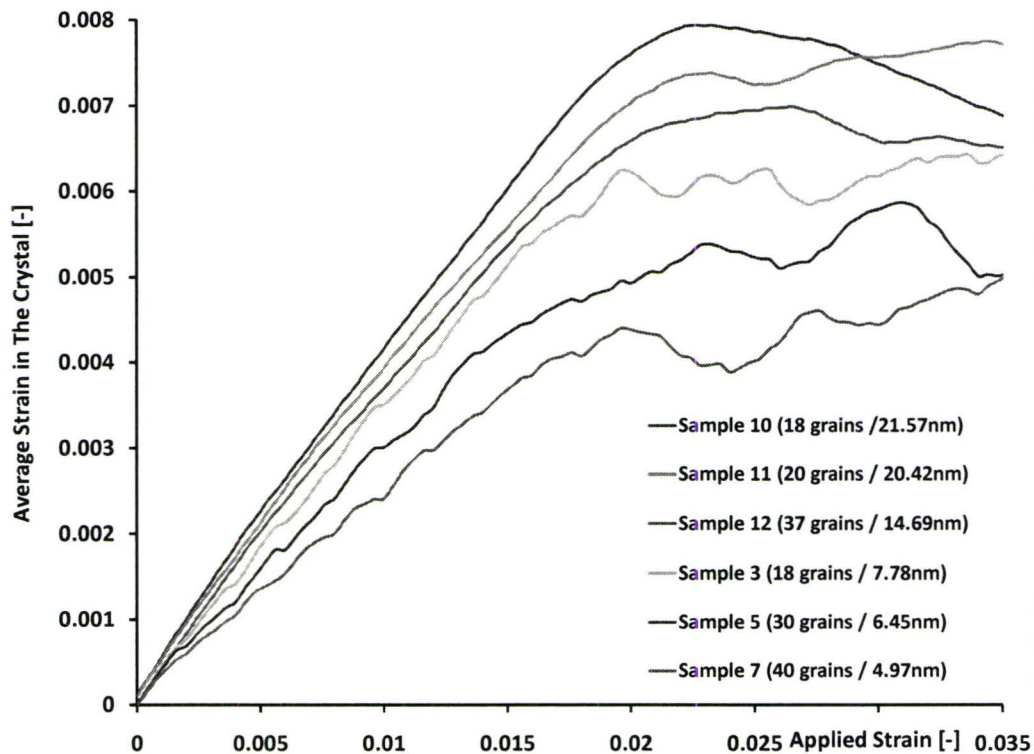


Figure 11.14: The effect of grain size on deformation. The average strain in the sample as function of applied strain. The curves show materials response to mechanical deformation by uniaxial tensile load. At low strains deformation is mainly elastic. Above $\approx 2\%$ of deformation plastic deformation sets in and the material starts to flow and deform plastically. Dependence of flow stress on grain size is displayed on Fig. 11.15.

proceeded by dislocation glide, grain rotation, and grain growth. Decay of low angle grain boundaries was a source of mobile dislocations during plastic flow. This is in agreement with TEM studies (section 3.1.3), where traces of dislocation activity was found. Moreover, we observed grain growth which is consistent with high resolution TEM (HRTEM) studies on NC Ag by Ichikawa et. al. [87]. Dislocation removed from or annihilated at the grain boundaries caused grains to rotate, as suggested by Murayama [125], who observed rotational movement of grain in HRTEM of Fe. An increasing ratio of grain boundaries to bulk material in NC materials caused a shift from dislocation mediated deformation to deformation carried by grain boundaries. As a result, we observed the formation of cracks at triple junctions and grain bound-

aries for lower grain sizes as reported by Kumar [22]. We did not observe any partial dislocation activity which might be caused by high stacking fault energy inherent in our 2D system. When plotting the grain size dependence of the yield strains, we found a decreasing trend with decreasing grain size, which suggests 'reversed' Hall-Petch behaviour. Limited by sample size we observed a plateau in the yield strain plot for grain sizes above 15nm. When the inverse square root of the grain size was plotted versus the yield strain, we found a negative linear relationship.

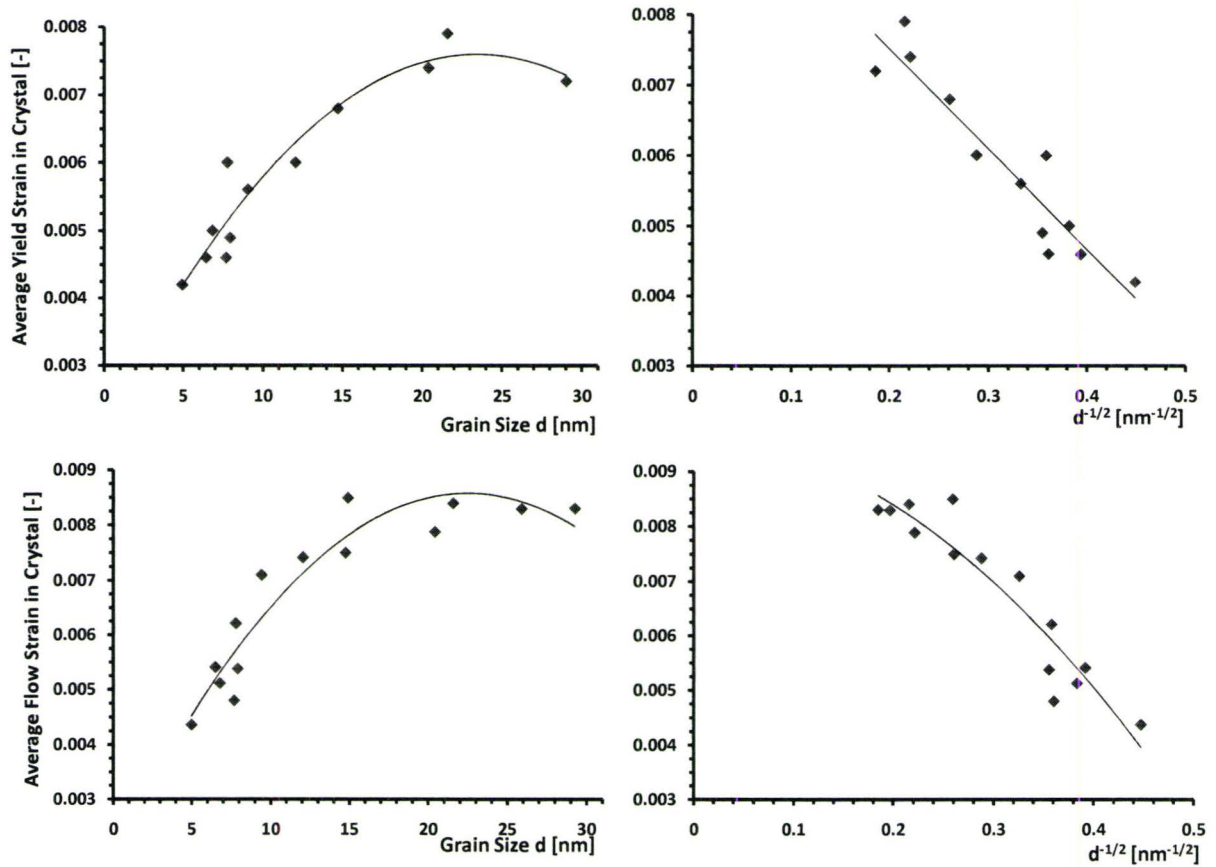


Figure 11.15: Hall-Petch type plot (right) and average strain plotted against the grain size (left). Top two slides correspond yield strain and bottom slides correspond to an average flow strain in the crystal. An increase in yield strain with increasing grain size can be found up to 15nm grain size, where the curve starts to plateau. The solid lines are guides to the eye.

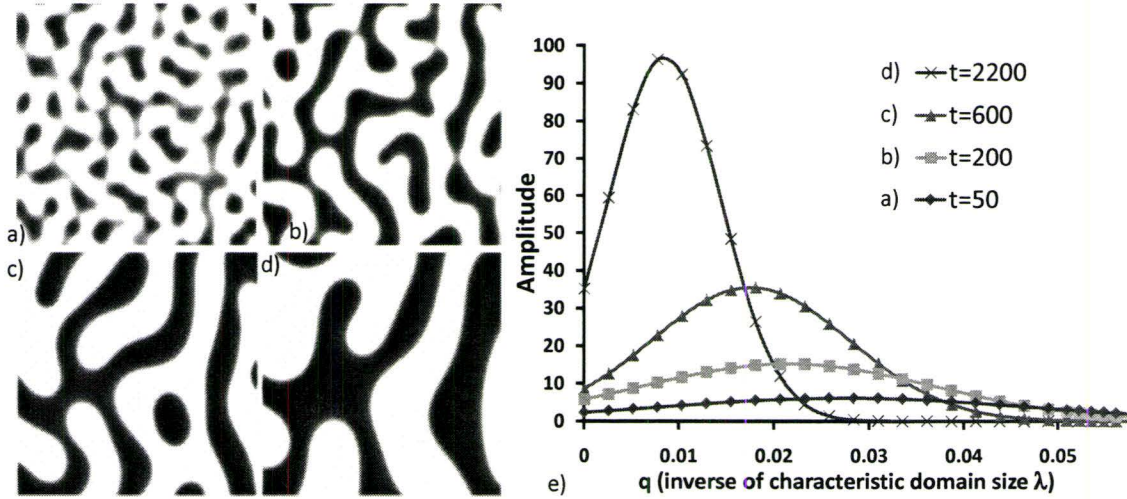


Figure 11.16: **Left:** Four time sequences in the evolution of the concentration field (gray scale) in a binary system with no dislocations present. superimposed on the corresponding density field. Dislocations are labeled by a square on the dislocation core surrounded by a circle. The time sequence (a)-(d) corresponds to $t = 50, 200, 600$ and 2200 . System size is: $800\Delta x \times 800\Delta x$, where $\Delta x = \pi/4$. The density difference $\delta N = 0$, while $L = 2.65$, $R_1/R_0 = 1/4$ ($R_0 = 1$) and all other parameters are the same as Fig. 9.1. **Right:** 2D structure factor calculated for the concentration profiles on the left.

11.9 Applications to Spinodal Decomposition

In previous sections we have discussed the application of MPFC model to dislocation behaviour, strain distribution, and strengthening effects in nanocrystalline materials due to grain boundaries. We continue our discussion by focusing on the study of strengthening by phase boundaries in spinodal decomposition. In chapter 5, we discussed details of spinodal decomposition process, during which smooth fluctuations in concentration are created. Studies of the domain growth kinetics in solid mixtures showed that the characteristic linear dimension λ – the domain size – grows according to a law given by $\lambda(t) \sim t^{1/3}$ [126]. Dislocations have been found to change the domain growth kinetics. At early stages of domain growth, dislocations and domains are randomly distributed and only few dislocations interact with the domain interface. At this stage, domain growth is exponentially fast and unaltered by dislocations. Later, when domains have grown in size, interfacial strain interacts with an increasing number of dislocations, dislocation density at the phase boundary

increases. Increasing dislocation density, together with mobility of the dislocations, are the limiting factors defining the growth rate of still relatively-fast moving interface [12]. When the decreasing velocity of the interface is decreasing the mobility of the dislocations is no longer a limiting factor to domain growth. Accelerated domain growth is now facilitated by increased interfacial tension (Fig. 5.3). At late times, when the velocity of the interface is low, the presence of dislocations is no longer a limiting factor and dislocations move slowly with the interface at the growth rate of $t^{1/3}$. Fully-developed domains interact with dislocations, hindering their motion, and causing material to harden.

To validate our model and verify basic kinetics, we first studied spinodal decomposition in a two dislocation-free systems. The first system was a binary mixture of A and B atoms with an atomic radii $R_A/R_B=0.1$ (i.e. 10% difference) and in the second system, atomic sizes differed by 25%.

Simulations began with a liquid phase of average dimensionless density difference $\delta N = 0$, which first solidified into a polycrystalline solid phase then subsequently phase separated as the reduced temperature (ΔB_o , Fig.9.1) was lowered below the spinodal.

The morphology changed from initially random fluctuations (Fig. 11.16a) to smooth coarse fluctuations in concentration (Fig. 11.16b-d). To analyze the morphology and kinetics of phase separation, we calculated structure factor by calculating a Fourier transformation of the concentration field. When plotted (Fig. 11.16e), we observed a position of the maxima in structure factor – characteristic wavelength – of the morphology. From Fig. 11.16e, we see that the characteristic wave vector decreases with time (i.e. size of the domain increases with time). By repeating the analysis over all time steps of the simulation, we obtained the time dependence of the characteristic domain wavelength. When plotted on $\log(t) - \log(\lambda)$, we were able to calculate growth rate and found a good agreement with $t^{1/3}$ growth rate Fig. 11.17.

In the example on Fig.11.16 both crystal structures (for species A and B) matched perfectly at the interface plane. To maintain coherency the lattice was distorted by *coherency strains* due to misfit between lattice parameters. The strains associated with a coherent interface raise the total energy of the system, and for larger atomic misfit it becomes energetically favorable to accommodate the interfacial strains by a misfit dislocation. To better isolate the effect of phase separation on dislocation

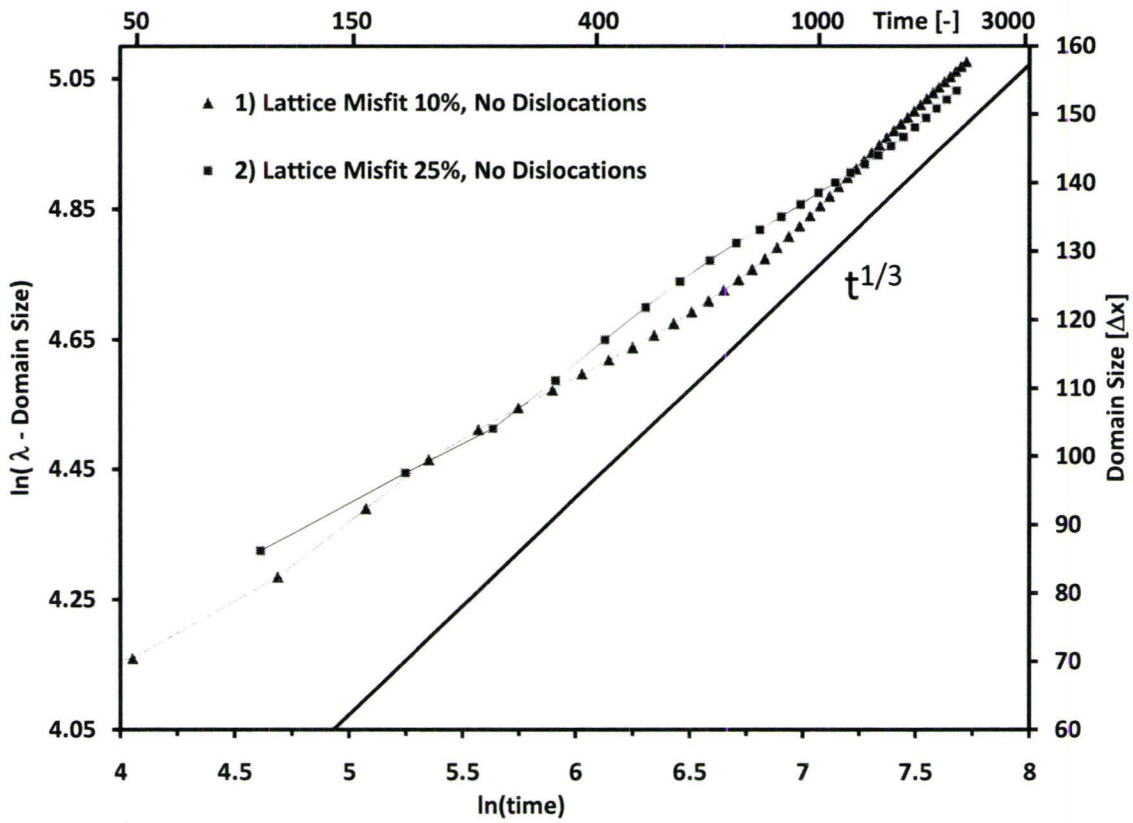


Figure 11.17: Log-Log plot of the characteristic linear dimension (domain size) at time t after the quench, for the simulation shown in Fig. 11.16. Domain size is extracted from structure factor (Fig. 11.16e.)

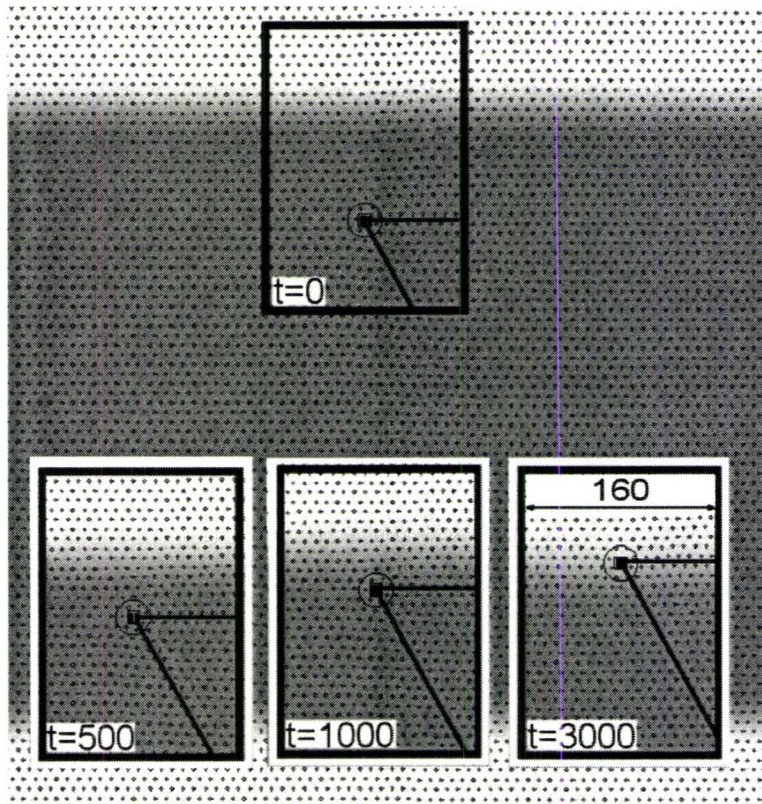


Figure 11.18: A dislocation migrates toward a coherent phase boundary, thus relaxing mismatch strain. An 800×800 (units of Δx) portion of the actual simulation domain is shown. The data shows four time frames in the motion of the dislocation. Parameters of the simulation are the same as in Fig. 11.16, except the misfit between the lattice parameters, which was increased to 0.5.

we studied dislocation motion near a coherent interface in the alloy.

In simulations, we increased the misfit between lattice parameters to 50% and placed a dislocation next to the interface. The dislocation was generated inside the perfect crystalline lattice using the same approach as in the section 11.6 where the dislocation glide was studied. After the initial equilibration, dislocation motion was visualized by locating a dislocation core. Fig. 11.18 demonstrates dislocation motion near the interface. The four frames on the figure show the dislocation moving to the interface, driven by coherency strains. Once the dislocation accommodated the misfit strain it became attached to the interface.

Figure 11.19 shows the temporal evolution of the phases during spinodal de-

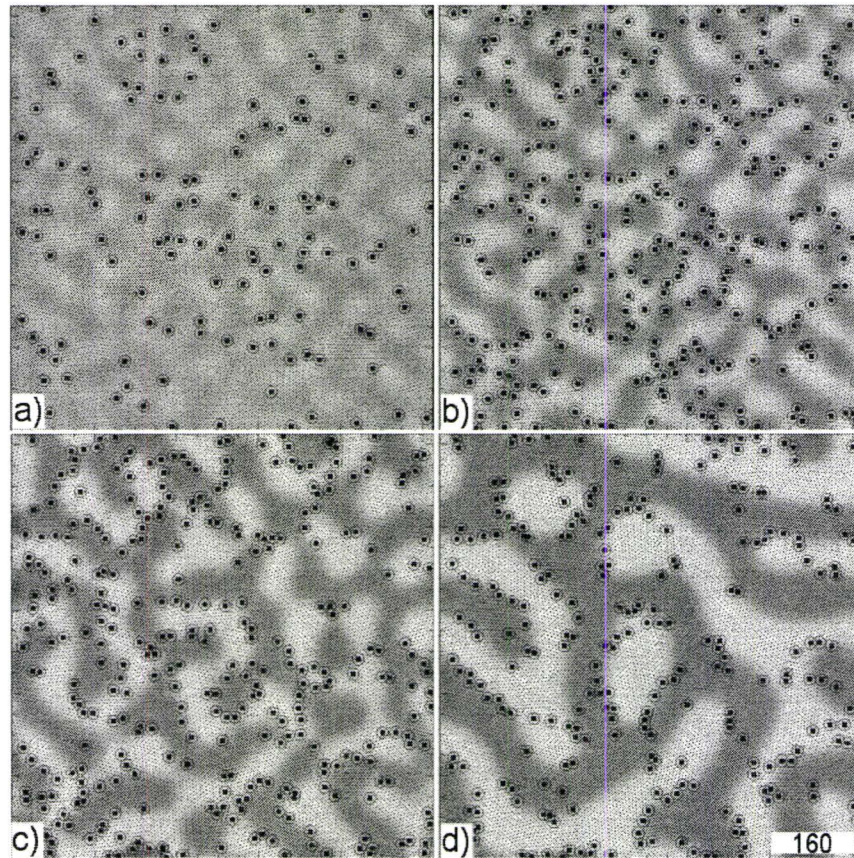


Figure 11.19: Four time sequences in the evolution of the concentration field (gray scale), superimposed on the corresponding density field. Dislocations are labeled by a square on the dislocation core surrounded by a circle. The time sequence (a)-(d) corresponds to $t = 100, 200, 800$ and 2500 , respectively. The system size is: $1024\Delta x \times 1024\Delta x$, where $\Delta x = \pi/4$.

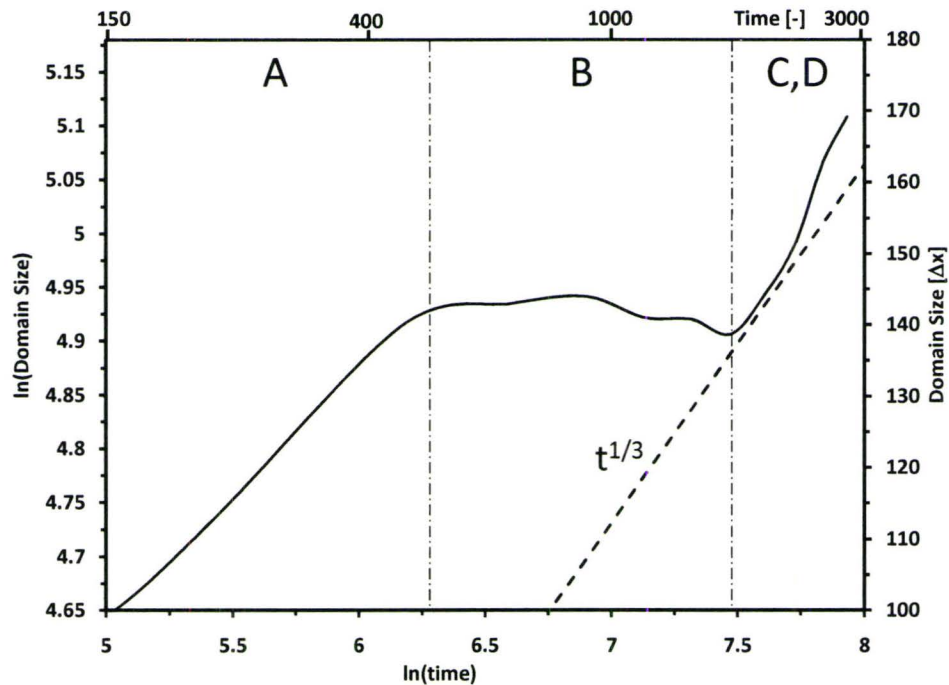


Figure 11.20: The solid line represents a time dependence of inverse of the mean wave vector of the (circularly averaged) 2D structure factor of the concentration field corresponding to the simulation in Fig. 11.19. The dashed line is a guide to the eye at a slope $t^{1/3}$. Growth regimes are outlined by dash-dotted vertical lines. Regime A is an initial growth with kinetics unaltered by dislocations. In regime B domains experience drag from the dislocations and slow down in growth rate. Regimes C, D are expanded in Fig.11.21.

composition of a binary alloy with dislocations present. Figures 11.20 and 11.21 show the corresponding growth rate of the domains.

Simulation began as in the first case, with a liquid phase of average dimensionless density difference $\delta N = 0$, which first solidified into a polycrystalline solid phase then subsequently phase separated as the reduced temperature (ΔB_o) was lowered below the spinodal. Initial conditions were chosen such that a number of dislocations would be present in the solid after the solidification. In a gray scale, the darker color corresponds to B-rich concentration profile. Dislocations are labeled by a square on the dislocation core surrounded by a circle. The four slides indicate the initially random distribution of dislocation through the sample (Fig. 11.19a,b). In this regime we observed rapid changes in morphology. The growth rate calculated from the structure

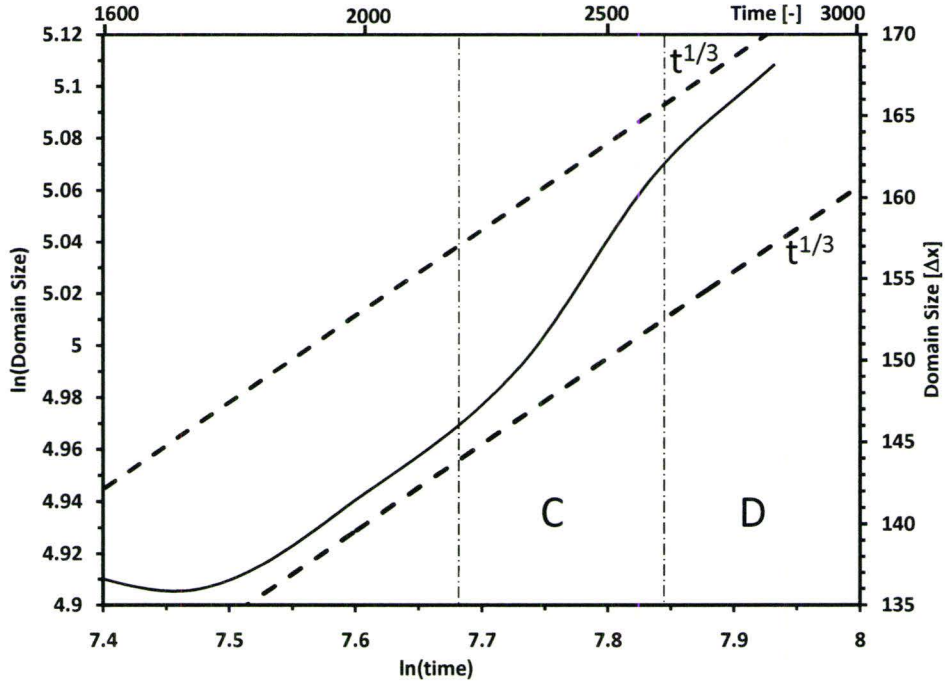


Figure 11.21: The domain growth rate at late times for simulation displayed in Fig. 11.19. The dashed lines are guides to the eye at a slope $t^{1/3}$. Growth regimes are outlined by dash-dotted vertical lines. Regime C is an accelerated regime, D corresponds to asymptotical regime.

factor is similar to the growth rate of the dislocation free system. This is displayed on Fig. 11.20 as regime "A". With continuous domain growth, the interfacial strain increases and more dislocations are attracted to the phase boundary (Fig. 11.19c). Limited by dislocation mobility, we observed plateau –slow down– in domain growth (Fig. 11.20, regime "B"). At $t \approx 2000$, almost all dislocations are attached to the grain boundary, which is manifested by accelerated domain growth. The accelerated regime is plotted separately on Fig. 11.21 as regime "C". Finally, at late times, a growth rate approaches the asymptotic regime ($t^{1/3}$) (Fig. 11.21 as regime "D"). These findings are in agreement with the findings in Refs.[103, 12].

Chapter 12

Extension to Three Dimensions

In the review of deformation processes in NC materials, we found that deformation is accompanied by a number of processes on multiple length and time scales. Deformation processes are sensitive to material structure. A simple example is a different number of slip systems in a face centered, body centered or hexagonal crystal structure. Another example mentioned was nucleation and propagation of partial dislocations during the deformation of NC materials observed by MD and XRD. Partial dislocations are due to the high stacking fault energy prohibitive in two dimensional systems. This is only a brief list of examples necessitating extension of MPFC modeling technique to three dimensions (3D).

As was discussed in section 7.1.2 it is the correlation function that defines the crystal symmetry in DFT free energy. The free energy used in previous chapters takes the form of Eq. 7.17:

$$\mathcal{F} = \int d\vec{r} \left(\frac{\rho}{2} [a\Delta T + c(k_0^2 + \nabla^2)^2] \rho + u \frac{\rho^4}{4} \right). \quad (12.1)$$

Here the term $(k_0^2 + \nabla^2)^2$ represents a two-point correlation function. The expression in Fourier space has the form $(k_0 - k^2)^2$. When plotted, it has a clearly defined peak at k_0 . The position of the peak represents an equilibrium wave vector in Fourier space, or the lattice spacing in real space. If used in the free energy without any other constraints, it will produce a triangular crystal lattice in 2D and BCC in 3D. Elder et. al. [127], for example, used this free energy to study dislocation and grain-boundary melting in three dimensional BCC crystal structure. To simulate other

crystal structures, the correlation function entering the free energy must be modified (i.e. must contain more peaks to represent a real material). Each peak corresponds to the crystal structure parameter, reciprocal lattice vector. Kroger [75] noted that not only is the position of the peaks important, but that their relative height can change the crystal structure. A correlation function for a particular material can be found by performing a MD simulation. A typical example of the correlation function for copper is displayed on Fig. 7.3. The correlation function $\hat{c}(k)$ is measured in a frequency space and as such is a function of the wave vector.

To simulate the 3D structure of copper, we used the same dynamics as in 2D case, Eq. 8.1. There were two possible approaches; either take an inverse Fourier transformation of $\hat{c}(k)$ and solve the dynamics equation (Eq. 8.1) in real space or transforming the equation into the Fourier (frequency) space. The latter approach has the advantage of avoiding a complicated solution of high order gradient terms, which was the main reason we favored the second approach.

In frequency space, the equation of motion of the diffusional PFC (Eq. 7.33) becomes

$$\frac{d\hat{\rho}_k}{dt} = -|k|^2\hat{\rho}_k - G\hat{N}L_k - \bar{\rho}\hat{C}(|k|)\hat{\rho}_k \quad (12.2)$$

where $\hat{\rho}_k = FFT[\rho]$ (i.e. $\hat{\rho}(k_x, k_y, t) = FFT[\rho(x, y, t)]$) and $G\hat{N}L_k \equiv FFT[\nabla^2(NL(\rho(x, y, t)))]$, where $NL = (\hat{\rho}_k)^2/2 - (\hat{\rho}_k)^3/3$.

Using full implicit discretization, we get:

$$\frac{\hat{\rho}_k^{n+1} - \hat{\rho}_k^n}{\Delta t} = -|k|^2\hat{\rho}_k^{n+1} - G\hat{N}L_k^{n+1} - \bar{\rho}\hat{C}(|k|)|k|^2\hat{\rho}_k^{n+1} \quad (12.3)$$

where the n and $n + 1$ means using the ρ at the n and $n + 1$ times, respectively. This equation is algebraic and to solve it we separate out $\hat{\rho}_k^{n+1}$, i.e.,

$$\hat{\rho}_k^{n+1} = \frac{\hat{\rho}_k^n - \Delta G\hat{N}L_k^{n+1}}{1 + \Delta t|k|^2 + \bar{\rho}|k|^2 C(|k|)} \quad (12.4)$$

We simulated the above equation using a mesh with periodic boundary conditions. Initial random fluctuations with the strength $\xi = 0.25$ were introduced into an undercooled melt to initiate the solidification process. The results are shown in

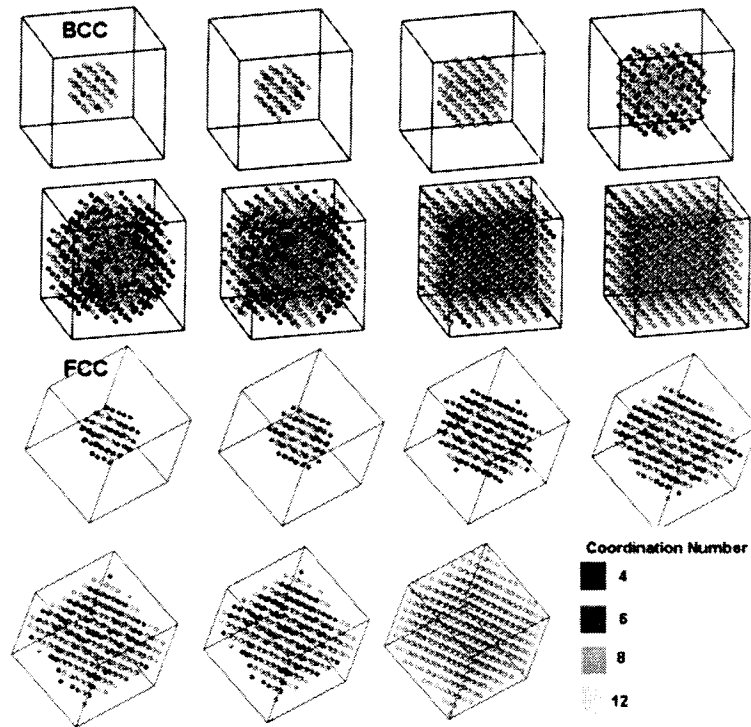


Figure 12.1: A single crystal growth with BCC and FCC structures simulated by Eq. 12.2. Coordination numbers of crystalline structures indicate a coordination number 8 in BCC and a coordination number 12 in FCC structure.

Fig. 12.1, which illustrates a FCC structure. By changing the reference density ρ_0 we were able to grow a stable BCC crystal using the same model as noted above. Having access to both BCC and FCC structure would allow us to look at the deformation processes of various crystal structures in the future. Fig. 12.1 shows a single crystal BCC structure as simulated by Eq. 12.4.

Chapter 13

Conclusion

This thesis presented and applied two new contributions to the *phase field crystal* modeling technique. The first was the development of a *modified* phase field crystal model (MPFC). This methodology offers a unique combination of accessible length scales and time scales, which are suitable to address problems in deformation and phase transformations in nanocrystalline (NC) materials. The MPFC method exploits separation time scales by introducing fast time scale to the diffusional time scale of the original PFC model. The separation of timescales is controlled by tunable parameters α and β , which are related to the effective speed of sound and the vacancy diffusion coefficient, respectively. A stability analysis of the linearized equation of motion showed a critical elastic length scale that sets the distance over which the disturbance will "instantaneously" travel. The basic properties of the model were verified by plotting displacements in the case of an effectively one dimensional bar and two dimensional double notched sample. In both cases we found a good agreement with theoretical expectations and experimental results. Measurements of dislocation velocity were consistent with those predicted by the Orowan equation. We found a linear relationship between the applied shear rate and dislocation velocity. The model was then applied to study the grain size strength dependence in nanocrystalline materials. When plotting the grain size dependence of the yield strains, we found a decreasing trend with decreasing grain size, which suggests 'reversed' Hall-Petch behaviour. We also observed a plateau in the yield strain plot for grain larger than above 15nm. At 15nm grain size, the deformation regime changed from dislocation-controlled to a regime where most of the deformation was carried by grain boundaries

that manifested itself in grain rotation, grain growth, and void nucleation and growth.

The second contribution presented in this thesis was the development and application of phase field crystal model to binary alloys. We examined connection between the density functional theory (DFT) of freezing and phase-field modeling. More specifically, it was shown that both the phase field crystal model and the regular solution commonly used in material science can be obtained from DFT, within certain limits. These calculations relied on parameterizing the direct two-point correlation function that enters DFT by three quantities related to the elastic energy stored in the liquid and crystalline phases, as well as the lattice constant.

Using the DFT connection, a simple binary alloy model was developed that self-consistently incorporates physical features inaccessible through other phase field approaches. The simplified alloy PFC model was shown to be able to simultaneously model solidification, phase segregation, grain growth, and elastic as well as plastic deformations in anisotropic systems with multiple crystal orientations on diffusive time scales. In particular, this model was applied to the study of spinodal decomposition. The model was calibrated and the basic kinetics of spinodal decomposition was verified by studying decomposition in a perfect crystal. We observed the growth rate of compositional domains to be consistent with the reported value of $t^{1/3}$. In the case where dislocations were present in the alloy sample, the kinetics was shown to be different as compared to the dislocation free sample. An initial slow down in the domain growth rate was observed, due to increased interface strains and the mobility of the dislocation. With continuous growth, the number of dislocations at the phase boundary increased, thus increasing the elastic strain in the sample. Increased stresses resulted in accelerated growth. At late times, the $t^{1/3}$ growth rate is again attained. We found there to be good agreement between our results and those in previously published studies.

Finally, we presented an extension of the model to three dimensions. The extension represents an important progress towards the simulation of real materials, since a number of deformation processes can be only observed in three dimensions. To obtain three dimensional structures, a correlation function for copper was used. This correlation function was found through molecular dynamics simulations and then used as an input to our model, as a function of wave vector k . This necessitated the solving of the equation of motion in a frequency space, through which we were able

to simulate single BCC and FCC crystals.

To solve the partial differential equation of motion for the modified phase field crystal model (MPFC), I developed an efficient solver that utilizes a multigrid technique. We measured its computational efficiency and convergence to find an improvement in both measures as compared to traditional iterative solvers. Moreover we found improved stability as compared to the explicit time marching scheme that had previously been used.

It is expected that both the alloy MPFC formalism and the MPFC with inclusion of instantaneous elastic modes will play an important role in linking material properties to microstructure development in a manner that *fundamentally* links the meso-scale to the atomic scale.

Appendix A

Deriving the New Phase-Field Crystal Model Starting from Hydrodynamics of Solids

In this chapter we detail the derivation of the new phase-field crystal model from hydrodynamics of solids. We can motivate the derivation of our semi-empirical model by considering the laws for mass and momentum conservation applied to a crystal system described by Eq. 7.4. These are given by

$$\begin{aligned} \rho \vec{v} &= \vec{g} \\ \frac{\partial \rho}{\partial t} &= -\nabla \cdot \vec{g} \\ \frac{\partial g_i}{\partial t} &= -\nabla_j \sigma_{ij}^R + d_i = -\frac{\delta \Pi}{\delta u_i} \end{aligned} \quad (\text{A.1})$$

where ρ , \vec{g} and \vec{v} denote the local mass density (non-zero everywhere), momentum and velocity, respectively (the subscript i denote their components), while u_i are the three components of the local displacement \vec{u} . The tensor σ_{ij}^R is the reactive part of the stress (i.e. that which can be related to local thermodynamic quantities) [128], while d_i represent the three components of a local *dissipative* force acting on the crystal. The nature of \vec{d} will be discussed further below. The term $\delta \Pi / \delta u_i$ in the last of Eqs. A.1 implies that we can equivalently derive momentum conservation from an

energy functional of the form

$$\Pi = \int_{sys} \left(f[\rho(\vec{x}, t)] + \frac{1}{2}\rho(\vec{x}, t)v^2 + u_i d_i \right) dV \quad (\text{A.2})$$

where the first term on the right hand side of Eq. A.2 is a phenomenological Gibb's free energy density, the second term is the local kinetic energy and the last term is the work due to internal dissipative forces (d_i) acting during solid deformation. The dissipation energy term gives rise so-called configurational forces on the system, which are created by the motion of defects, vacancies and grain boundaries [129]. In the context of the present study, the free energy density $f[\rho(\vec{x}, t)]$ is chosen to be minimized by periodic crystal densities. It is the existence of such minima that leads to elastic energy of solids [16]. Namely, small deviations of the density from its equilibrium state give rise to (recoverable) elastic deformation energy. Density states with topological defects represent plastically deformed crystals, which are constrained in local (time-dependent) minima far from equilibrium.

We can reduce the system of Eqs. A.1 into Eq. 8.1 as follows. We first take the time derivative of the (second) mass conservation equation and the divergence of the (third) momentum conservation equation. This gives, respectively,

$$\begin{aligned} \frac{\partial^2 \rho}{\partial t} &= -\frac{\partial(\nabla \cdot \vec{g})}{\partial t} \\ \frac{\partial(\nabla \cdot \vec{g})}{\partial t} &= -\nabla_i \frac{\delta \Pi}{\delta u_i} \end{aligned} \quad (\text{A.3})$$

Substituting for the first term in the second of Eqs. A.3 using the first equation, we arrive at

$$-\frac{\partial^2 \rho}{\partial t} = -\nabla_i \frac{\delta \Pi}{\delta u_i} \quad (\text{A.4})$$

To proceed further Π must be related explicitly to the density field $\rho(\vec{x}, t)$.

A constitutive relation between the coarse-grained density ρ and the local crystal displacement field u_i is obtained by assuming that the density changes very slowly, allowing us to write $\rho = \rho_o(\vec{x}) + \delta\rho(\vec{x}, t)$, where $\rho_o(\vec{x})$ is a reference (equilibrium) density field of the crystal. We next take the divergence of the first equation in Eq. (A.1) and use the (second) mass conservation equation to eliminate \vec{g} . Expanding to linear

order in $\delta\rho$, velocity and their gradients, we obtain

$$\frac{\partial}{\partial t} \left(\nabla \cdot \vec{u} + \frac{\delta\rho}{\rho_o} \right) = -\frac{\partial}{\partial t} \left(\dot{\vec{u}} \cdot \frac{\nabla\rho_o}{\rho_o} \right) \quad (\text{A.5})$$

Equating the expressions in the brackets of the left and right hand sides of Eq. (A.5) we obtain

$$\rho - \rho_o = -\nabla \cdot (\rho_o \vec{u}) = \rho_o \frac{\partial u_j}{\partial x_j} - u_j \frac{\partial \rho_o}{\partial x_j} \quad (\text{A.6})$$

Returning to Eqs. A.4, we perform the functional integral on the right hand side, obtaining

$$\frac{\delta\Pi}{\delta u_i} = \int_{sys} \frac{\delta f[\rho(\vec{x}, t)]}{\delta \rho(\vec{x}', t)} \frac{\delta \rho(\vec{x}', t)}{\delta u_i(\vec{x}, t)} d\vec{x}' + d_i(\dot{\vec{u}}) \quad (\text{A.7})$$

We use the constitutive relation Eq. A.6 to simplify the expression $\delta\rho/\delta u_i$ in Eq. A.7. Doing so we obtain

$$\frac{\delta\rho}{\delta u_i} \approx \rho_o \delta_{ij} \frac{\partial}{\partial x_j} \delta(\vec{x} - \vec{x}') - \delta_{ij} \frac{\partial \rho_o}{\partial x_j} \delta(\vec{x} - \vec{x}') \quad (\text{A.8})$$

Substituting for Eq. A.8 in Eq. A.7 we obtain

$$\frac{\delta\Pi}{\delta u_i} = \delta_{ij} (\rho_o \nabla_j \mu) + d_i(\dot{\vec{u}}) \quad (\text{A.9})$$

where $\mu \equiv \delta F/\delta\rho$ is the generalized chemical potential of the crystal. The simplest form we can take for the dissipation force is of the form

$$d_i = \beta\rho(\vec{x}, t)\dot{\vec{u}} \quad (\text{A.10})$$

where β is a constant. Substituting d_i and Eq. A.9 into Eq. A.4 finally gives Eq. 8.1.

The dissipation force in Eq. A.10 depends on the velocities not their gradients, as is typically done in deriving the viscosity tensor in continuum mechanics. As mentioned above \vec{d} is a a form of configurational force, arising directly from local changes in mass flux due to defects, vacancies and grain boundaries. In an infinite periodic crystal, this form of \vec{d} would be incorrect since the system is translationally invariant. However, in a crystal containing free surfaces, at least one of which is always be constrained, translational invariance is broken and the form of the dissipative force

in Eq. A.10 is phenomenologically correct. We also note that when a crystal is in coexistence with its melt [16], the form of Eq. A.10 naturally gives rise to a Stokes-type dissipation when coherent portions the crystal break off and move through liquid phase.

Appendix B

Derivation of Simple Binary Alloy Model

This appendix goes through the expansion required to arrive at the simplified alloy model presented in section 9. For this calculation the free energy functional in Eq. (9.7) is expanded in the variables n and δN , as defined in Eq. (9.27), up to order four (noting that terms of order n or δN can be dropped since they integrate to zero in the free energy functional as they are all defined around their average values). In addition it will be assumed that δN varies on length scales much larger than n . This is a reasonable on long time (diffusion) times scales, where solute and host atoms intermix on length scales many times larger than the atomic radius. This assumption allows terms of order $n\delta N$ to be eliminated from the free energy. The result of these expansions and approximations is that the free energy functional can be written as

$$\begin{aligned} \frac{\mathcal{F}}{\bar{\rho}k_B T} = & \int d\vec{r} \left[f_o + B^\ell \frac{n^2}{2} - \frac{n^3}{6} + \frac{n^4}{12} + nF\nabla^2 n \right. \\ & + \frac{\delta N}{2} \left(1 - \frac{C^{AA} + C^{BB} - 2C^{AB}}{4} \right) \delta N \\ & + \frac{\delta N^4}{12} + \frac{\beta}{2\bar{\rho}} (1 - n^3) \delta N + nG\nabla^4 n \\ & \left. + \frac{dC}{4\bar{\rho}} \left((\bar{\rho} - \rho_\ell)^2 - \rho_\ell^2 n^3 \right) \delta N \right] \end{aligned} \quad (\text{B.1})$$

where

$$\begin{aligned}
 f_o &= \ln\left(\frac{\bar{\rho}}{2\rho_\ell}\right) - (1 - \rho_\ell/\bar{\rho}) - \bar{\rho}\hat{C}_0^{AB}/4 \\
 &\quad - \frac{1}{8}(\bar{\rho} + 2\rho_\ell^2/\bar{\rho} - 4\rho_\ell)(\hat{C}_0^{AA} + \hat{C}_0^{BB}) \\
 B^\ell &= 1 - \bar{\rho}\hat{C}_0 + \bar{\rho}^{-1}(\beta + \rho_\ell^2 d\hat{C}_0/2)\delta N + \delta N^2 \\
 F &= -\bar{\rho}\hat{C}_2 + \rho_\ell^2 d\hat{C}_2 \delta N/2\bar{\rho} \\
 G &= -\bar{\rho}\hat{C}_4 + \rho_\ell^2 d\hat{C}_4 \delta N/2\bar{\rho} \\
 dC &= C^{AA} - C^{BB},
 \end{aligned} \tag{B.2}$$

while $\hat{C}_n \equiv (\hat{C}_n^{AA} + \hat{C}_n^{BB} + 2\hat{C}_n^{AB})/4$ and $d\hat{C}_n \equiv \hat{C}_n^{AA} - \hat{C}_n^{BB}$.

The previous equation can finally be cast into a form similar to that presented in Section 9.4 of the text,

$$\begin{aligned}
 \frac{\mathcal{F}}{\bar{\rho}k_B T} &= \int d\bar{r} \left[f_o + \frac{n}{2} [B^\ell + B^s(2R^2\nabla^2 + R^4\nabla^4)] \right] n \\
 &\quad - \frac{n^3}{6} + \frac{n^4}{12} + \frac{w}{2}\delta N^2 + \frac{\delta N^4}{12} + \frac{L^2}{2}|\nabla\delta N|^2 \\
 &\quad + \gamma\delta N + \frac{H^4}{2}\delta N\nabla^4\delta N
 \end{aligned} \tag{B.3}$$

where $B^s = F^2/(2G)$, $R = \sqrt{2G/F}$, $w = (1 - \Delta\hat{C}_0/2)$, $L^2 = \Delta\hat{C}_2/2$, $H^2 = -\Delta\hat{C}_4/2$ and $2\bar{\rho}\gamma = \beta(1 - n^3) + dC((\bar{\rho} - \rho_\ell)^2 - \rho_\ell^2 n^3)/2$ ($\Delta\hat{C}_n$ as in Eq. 9.13).

The dependence of the coefficients in B^ℓ , B^s and R on the density difference can be explicitly obtained by expanding them in δN as well. This gives,

$$\begin{aligned}
 B^\ell &= B_0^\ell + B_1^\ell \delta N + B_2^\ell \delta N^2 \\
 B^s &= B_0^s + B_1^s \delta N + B_2^s \delta N^2 + \dots \\
 R &= R_0 + R_1 \delta N + R_2 \delta N^2 + \dots
 \end{aligned} \tag{B.4}$$

where

$$B_0^\ell = 1 - \bar{\rho}\hat{C}_0, \tag{B.5}$$

$$\bar{\rho}B_1^\ell = \beta + \rho_\ell^2 d\hat{C}_0/2, \quad (\text{B.6})$$

$$B_2^\ell = 1, \quad (\text{B.7})$$

$$B_0^s = -\bar{\rho}(\hat{C}_2)^2/\hat{C}_4, \quad (\text{B.8})$$

$$B_1^s = -\hat{C}_2\rho_\ell^2(\hat{C}_2d\hat{C}_4 - 2\hat{C}_4d\hat{C}_2)/4\bar{\rho}\hat{C}_4^2, \quad (\text{B.9})$$

$$B_2^s = -\rho_\ell^2(\hat{C}_2d\hat{C}_4 - \hat{C}_4d\hat{C}_2)^2/8\bar{\rho}^3\hat{C}_4^3, \quad (\text{B.10})$$

$$R_0 = \sqrt{2\hat{C}_4/\hat{C}_2}, \quad (\text{B.11})$$

$$R_1/R_0 = -\rho_\ell^2(d\hat{C}_4/\hat{C}_4 - d\hat{C}_2/\hat{C}_2)/4\bar{\rho}^2, \quad (\text{B.12})$$

and

$$R_2/R_0 = -\rho_\ell^4(\hat{C}_2d\hat{C}_4 - \hat{C}_4d\hat{C}_2)(\hat{C}_2d\hat{C}_4 + 3\hat{C}_4d\hat{C}_2)/32\bar{\rho}^4\hat{C}_4^2\hat{C}_2^2. \quad (\text{B.13})$$

Appendix C

Multigrid - Full Approximation Scheme

In this section, we develop a nonlinear Full Approximation Storage (FAS) multigrid method to solve the system in equations 10.1 at the implicit time level. The fundamental idea of nonlinear multigrid is analogous to the linear case. First, the errors to the solution have to be smoothed so that they can be approximated on a coarser grid. An analogue of the linear defect equation is transformed to the coarse grid. The coarse grid corrections are interpolated back to the fine grid, where the errors are again smoothed. However, because the system is nonlinear we do not work with the errors, but rather with full approximations to the discrete solution on the coarse grid.

Equations 10.1 can be rewritten as:

$$NSO(\rho^n, \rho^{n+1}, \mu^{n+1/2}, v^{n+1}) = (f^n, g^n, e^n) \quad (\text{C.1})$$

where

$$\begin{aligned} NSO(u^n, u^{n+1}, c^{n+1/2}, v^{n+1}) = & \quad (\text{C.2}) \\ & \left(\left(\frac{\beta dt}{2} + 1 \right) u_{i,j}^{n+1} + \alpha^2 \nabla^2 c_{i,j}^{n+1/2}, \right. \\ & \left. (-1 - r) u_{i,j}^{n+1} + \hat{\phi}(u_{i,j}^n, u_{i,j}^{n+1}) + c_{i,j}^{n+1/2} + (-\nabla^2 - 2) v_{i,j}^{n+1}, \nabla^2 u_{i,j}^{n+1} + v_{i,j}^{n+1} \right) \end{aligned}$$

and source terms are

$$(f^n, g^n, e^n) = \left(2\rho_{i,j}^n + \rho_{i,j}^{n-1} \left(\frac{\beta dt}{2} - 1 \right), 0, \nabla^2 \rho_{i,j}^n \right) \quad (\text{C.3})$$

In what follows, we assume a sequence of grids Ω_k . ν is the number of pre-smoothing and post-smoothing steps. An iteration step for the nonlinear multigrid method using the V-cycle is formally written as follows:

FAS cycle

$$\begin{aligned} & \left\{ \rho_k^{m+1}, \mu_k^{m+1/2}, v_k^{m+1} \right\} = \\ \text{FAScycle} & \left\{ k, \rho_k^{n-1}, \rho_k^n, \rho_k^m, \mu_k^{m-1/2}, v_k^m, \text{NSO}_k, f_k^n, g_k^n, e_k^n, \nu \right\} \end{aligned} \quad (\text{C.4})$$

That is $\left\{ \rho_k^{m+1}, \mu_k^{m+1/2}, v_k^{m+1} \right\}$ and $\left\{ \rho_k^m, \mu_k^{m-1/2}, v_k^m \right\}$ are approximations of $\rho_k(x_i, y_j)$ and $\mu_k(x_i, y_j)$ and $v_k(x_i, y_j)$ before and after FAS cycle, respectively. Now we define a FAS cycle:

Presmoothing

Compute $\left\{ \bar{\rho}_k^m, \bar{\mu}_k^{m-1/2}, \bar{v}_k^m \right\}$ by applying ν smoothing steps to $\left\{ \rho_k^m, \mu_k^{m-1/2}, v_k^m \right\}$

$$\left\{ \bar{\rho}_k^m, \bar{\mu}_k^{m-1/2}, \bar{v}_k^m \right\} = \text{SMOOTH}^\nu \left(\rho_k^n, \rho_k^m, \mu_k^{m-1/2}, \text{NSO}_k, f_k^n, g_k^n, e_k^n \right), \quad (\text{C.5})$$

which means performing ν smoothing steps with initial approximation $\rho_k^m, \rho_k^n, \mu_k^{m-1/2}$, source terms f_k^n, g_k^n, e_k^n and the *SMOOTH* relaxation operator to get $\bar{\rho}_k^m, \bar{\mu}_k^{m-1/2}, \bar{v}_k^m$

One *SMOOTH* relaxation operator step consists of solving the system given below by 3×3 matrix inversion for each i and j .

$$\begin{pmatrix} \beta dt/2 + 1 & 4\alpha^2 dt^2/dx^2 & 0 \\ (-1-r) - 3/2(\rho_{i,j}^{n,2} + \rho_{i,j}^{m,2}) & 1 & 4/dx^2 - 2 \\ 2/dx^2 & 0 & 1 \end{pmatrix} \begin{pmatrix} \bar{\rho}_{i,j}^m \\ \bar{\mu}_{i,j}^{m-1/2} \\ \bar{v}_{i,j}^m \end{pmatrix} =$$

$$\left(\begin{array}{l} \underbrace{2\rho_{i,j}^n + \rho_{i,j}^{n-1} (\beta dt/2 - 1) + 4\alpha^2 dt^2/dx^2 (\bar{\mu}_{i-1,j}^{m-1/2} + \mu_{i+1,j}^{m-1/2} + \mu_{i,j+1}^{m-1/2} + \bar{\mu}_{i,j-1}^{m-1/2})}_{f_k^n - \text{sourceterm}} \\ (\bar{v}_{i-1,j}^m + v_{i+1,j}^m + v_{i,j+1}^m + \bar{v}_{i,j-1}^m)/dx^2 + 1/2 (\rho_{i,j}^n{}^3 + \rho_{i,j}^m{}^3) - 3/2 (\rho_{i,j}^n{}^2 + \rho_{i,j}^m{}^2) \rho_{i,j}^m \\ (\bar{\rho}_{i-1,j}^m + \rho_{i+1,j}^m + \rho_{i,j+1}^m + \bar{\rho}_{i,j-1}^m)/2dx^2 \underbrace{(+\rho_{i-1,j}^n + \rho_{i+1,j}^n + \rho_{i,j+1}^n + \rho_{i,j-1}^n - 4\rho_{i,j}^n)/2dx^2}_{g_k^n - \text{sourceterm}} \end{array} \right) \quad (C.6)$$

Compute Defect

$$(\bar{d}1_k^m, \bar{d}2_k^m, \bar{d}3_k^m) = (f_k^n, g_k^n, e_k^n) - NSO_k (\bar{\rho}_k^n, \bar{\rho}_k^m, \bar{\mu}_k^{m-1/2}, \bar{v}_k^m) \quad (C.7)$$

Restrict the defect and $\{\bar{\rho}_k^m, \bar{\mu}_k^{m-1/2}, \bar{v}_k^m\}$

$$(\bar{d}1_{k-1}^m, \bar{d}2_{k-1}^m, \bar{d}3_{k-1}^m) = I_k^{k-1} (\bar{d}1_k^m, \bar{d}2_k^m, \bar{d}3_k^m) \quad (C.8)$$

$$(\bar{\rho}_{k-1}^m, \bar{\mu}_{k-1}^{m-1/2}, \bar{v}_{k-1}^m) = I_k^{k-1} (\bar{\rho}_k^m, \bar{\mu}_k^{m-1/2}, \bar{v}_k^m) \quad (C.9)$$

The restriction operator I_k^{k-1} maps k -level functions to $(k-1)$ -level functions. A *full weighting* restriction operator is applied according to Eq. 10.11.

Compute the RHS

$$(f_{k-1}^n, g_{k-1}^n, e_{k-1}^n) = (\bar{d}1_{k-1}^m, \bar{d}2_{k-1}^m, \bar{d}3_{k-1}^m) + NSO_{k-1} (\bar{\rho}_{k-1}^n, \bar{\rho}_{k-1}^m, \bar{\mu}_{k-1}^{m-1/2}, \bar{v}_{k-1}^m) \quad (C.10)$$

Compute an approximate solution $\{\hat{\rho}_{k-1}^m, \hat{\mu}_{k-1}^{m-1/2}\}$ of the coarse grid equation on Ω_{k-1} i.e. solve

$$NSO_{k-1} (\hat{\rho}_{k-1}^n, \hat{\rho}_{k-1}^m, \hat{\mu}_{k-1}^{m-1/2}, \hat{v}_{k-1}^m) = (f_{k-1}^n, g_{k-1}^n, e_{k-1}^n) \quad (C.11)$$

if $k = 1$, we explicitly invert 3×3 matrix to obtain the solution. If $k > 1$ we solve Eq. C.11 by performing a **FAS** k -grid cycle using $\{\bar{\rho}_{k-1}^m, \bar{\mu}_{k-1}^{m-1/2}\}$ as an initial approximation:

$$\begin{aligned} & \{\hat{\rho}_{k-1}^m, \hat{\mu}_{k-1}^{m-1/2}, \hat{v}_{k-1}^m\} = \quad (C.12) \\ \text{FAScycle} \{ & k-1, \rho_{k-1}^n, \bar{\rho}_{k-1}^m, \bar{\mu}_{k-1}^{m-1/2}, \bar{v}_k^m, \mathbf{NSO}_{k-1}, f_{k-1}^n, g_{k-1}^n, e_{k-1}^n, \nu \} \end{aligned}$$

Compute the coarse grid correction (CGC)

$$\hat{v}1_{k-1}^m = \hat{\rho}_{k-1}^m - \bar{\rho}_{k-1}^m \quad (C.13)$$

$$\hat{v}2_{k-1}^{m-1/2} = \hat{\mu}_{k-1}^{m-1/2} - \bar{\mu}_{k-1}^{m-1/2} \quad (C.14)$$

$$\hat{v}3_{k-1}^m = \hat{v}_{k-1}^m - \bar{v}_{k-1}^m \quad (C.15)$$

Interpolate the correction (CGC)

$$\hat{v}1_k^m = I_{k-1}^k \hat{v}1_{k-1}^m \quad (C.16)$$

$$\hat{v}2_k^{m-1/2} = I_{k-1}^k \hat{v}2_{k-1}^{m-1/2} \quad (C.17)$$

$$\hat{v}3_k^m = I_{k-1}^k \hat{v}3_{k-1}^m \quad (C.18)$$

The interpolation operator I_{k-1}^k maps $(k-1)$ -level functions to k -level functions. Here, the coarse values are transferred to the four nearby fine grid points according to *bilinear operator* in Fig. 10.5.

Compute the corrected approximation on Ω_k

$$\rho_k^{m, \text{afterCGC}} = \bar{\rho}_k^m + \hat{v}1_k^m \quad (C.19)$$

$$\mu_k^{m-1/2, \text{afterCGC}} = \bar{\mu}_k^{m-1/2} + \hat{v}2_k^{m-1/2} \quad (C.20)$$

$$v_k^{m, \text{afterCGC}} = \bar{v}_k^m + \hat{v}3_k^m \quad (C.21)$$

Postsmoothing

Compute $\{\rho_k^{m+1}, \mu_k^{m+1/2}, v_k^{m+1}\}$ by applying ν smoothing steps to $\{\rho_k^{m,after-CGC}, \mu_k^{m-1/2,after-CGC}, v_k^{m,after-CGC}\}$

$$\left\{ \rho_k^{m+1}, \mu_k^{m+1/2}, v_k^{m+1} \right\} = \text{SMOOTH}^\nu \left(\rho_k^n, \rho_k^{m,after-CGC}, \mu_k^{m-1/2,after-CGC}, \mathbf{NSO}_k, f_k^n, g_k^n, e_k^n \right), \quad (\text{C.22})$$

which means performing ν smoothing steps with initial approximation $\rho_k^m, \rho_k^n, \mu_k^{m-1/2}$, source terms f_k^n, g_k^n, e_k^n and the *SMOOTH* relaxation operator to get $\bar{\rho}_k^m, \bar{\mu}_k^{m-1/2}, v_k^m$

Bibliography

- [1] William D. Callister. *Materials Science and Engineering an Introduction*, chapter 7.8, page 160. John Wiley & Sons, New York, 4 edition, 1997.
- [2] H. Gleiter. Nanostructured materials:basic concepts and microstructure. *Acta Materialia*, 48:1–29, 2000.
- [3] E.O. Hall. The deformation and ageing of mild steel. *Proc. R. Soc. London B*, 64:747–753, 1951.
- [4] N.J Petch. The cleavage strength of polycrystals. *Journal of the Iron and Steel Institute*, 174:25–28, May 1953.
- [5] Sidney Yip. The strognest size. *Nature*, 391:532–533, February 1998.
- [6] J. A. Warren and W. J. Boettinger. Prediction of dendritic growth and microsegregation patterns in a binary alloy using the phase-field method. *Acta Metallurgica et Materialia*, 43(2):689–703, 2 1995.
- [7] John W. Cahn and John E. Hilliard. Free energy of a nonuniform system. i. interfacial free energy. *The Journal of Chemical Physics*, 28(2):258–267, 1958.
- [8] Bruno Grossmann, K. R. Elder, Martin Grant, and J. M. Kosterlitz. Directional solidification in two and three dimensions. *Phys. Rev. Lett.*, 71(20):3323–3326, Nov 1993.
- [9] Alain Karma and Wouter-Jan Rappel. Phase-field method for computationally efficient modeling of solidification with arbitrary interface kinetics. *Phys. Rev. E*, 53(4):R3017–R3020, Apr 1996.
- [10] Nikolas Provatas, Nigel Goldenfeld, and Jonathan Dantzig. Efficient computation of dendritic microstructures using adaptive mesh refinement. *Phys. Rev. Lett.*, 80(15):3308–3311, Apr 1998.
- [11] Nikolas Provatas, Quanyong Wang, Mikko Haataja, and Martin Grant. Sea-weed to dendrite transition in directional solidification. *Phys. Rev. Lett.*, 91(15):155502, Oct 2003.

- [12] Mikko Haataja and Francois Léonard. Influence of mobile dislocations on phase separation in binary alloys. *Phys. Rev. B*, 69:081201, 2004.
- [13] S. Y. Hu and L. Q. Chen. Solute segregation and coherent nucleation and growth near a dislocationa phase-field model integrating defect and phase microstructures. *Acta Materialia*, 49:463–472, 2001.
- [14] D. Rodney, Y. Le Bouar, and A. Finel. Phase field methods and dislocations. *Acta Materialia*, 51:17–30, 2003.
- [15] K. R. Elder and Martin Grant. Modeling elastic and plastic deformations in non-equilibrium processing using phase field crystals. *Phys. Rev. E*, 70(5):051605, November 2004.
- [16] K. R. Elder, Mark Katakowski, Mikko Haataja, and Martin Grant. Modeling elasticity in crystal growth. *Phys. Rev. Lett.*, 88(24):245701–1–4, June 2002.
- [17] J. Berry, M. Grant, and K. R. Elder. Diffusive atomistic dynamics of edge dislocations in two dimensions. *Physical Review E (Statistical, Nonlinear, and Soft Matter Physics)*, 73(3):031609, 2006.
- [18] N Goldenfeld, BP Athreya, and JA Dantzig. Renormalization group approach to multiscale simulation of polycrystalline materials using the phase field crystal model. *Phys. Rev. E*, 72(2, Part 1):020601(R), AUG 2005.
- [19] P. Stefanovic, M. Haataja, and N. Provatas. Phase-field crystals with elastic interactions. *Phys. Rev. Lett.*, 96:225504, 2006.
- [20] T. V. Ramakrishnan and M. Yussouff. First-principles order-parameter theory of freezing. *Phys. Rev. B*, 19:2775 – 2794, 1979.
- [21] S. Majaniemi and M. Grant. Dissipative phenomena and acoustic phonons in isothermal crystals: A density-functional theory study. *Phys. Rev. B*, 75:054301, 2007.
- [22] K.S. Kumar, H. Van Swygenhoven, and S. Suresh. Mechanical behavior of nanocrystalline metals and alloys. *Acta Materialia*, 53:5743–5774, 2003.
- [23] H. Gleiter. Nanocrystalline materials. *Progress in Materials Science*, 33:223–315, 1989.
- [24] P.G. Sanders, G.E. Fougere, L.I. Thompson, J.A. Eastman, and J.R. Weertman. Improvements in the synthesis and compaction of nanocrystalline materials. *Nanostructured Materials*, 8(3):243–252, 1997.

- [25] P.G. Sanders, C.J. Youngdahl, and J.R. Weertman. The strength of nanocrystalline metals with and without flaws. *Materials Science and Engineering*, A234-236:77–82, 1997.
- [26] A. Chokshi, A. Rosen, J. Karch, and H. Gleiter. On the validity of the hall-petch relationship in nanocrystalline materials. *Scripta Metallurgica*, 23:1679–1684, 1989.
- [27] G.E. Fougere, J.R. Weertman, R.W. Siegel, and S. Kim. Grain-size dependent hardening and softening of nanocrystalline cu and pd. *Scripta Metallurgica*, 26:1879–1883, 1992.
- [28] H. Natter, M. Smelzer, and R. Hempelmann. Nanocrystalline nicke and nickel-copper alloys: synthesis characterization and thermal stability. *Journal of Materials Research*, 13(5):1186–1197, May 1998.
- [29] T. Yamasaki, P. Schloßmacher, K. Ehrlich, and Y. Ogino. Formation of amorphous electrodeposited ni-w alloys and their nanocrystallization. *Nanostructured Materials*, 10(3):375–388, 1998.
- [30] U. Erb. Electrodeposited nanocrystals: Synthesis, properties and industrial applications. *Nanostructured Materials*, 6:533–538, 1995.
- [31] G. Palumbo, F. Gonzalez, A.M. Brennenstuhl, W. Shmayda U. Erb, and P.C. Lichtenberger. In-situ nuclear steam generator repair using electrodeposited nanocrystalline nicke. *Nanostructured Materials*, Vol. 9.:737–746, 1997.
- [32] R.Z. Valiev, I.V. Alexandrov, Y.T. Zhu, and T.C. Lowe. Paradox of strength and ductility in metals processed by severe plastic deformation. *Journal of Materials Research*, 17:5, 2002.
- [33] K. Lu, J.T. Wang, and D. Wei. A new method for sythesizing nanocrystalline alloys. *Journal of Applied Physics*, 69(1):522–524, January 1991.
- [34] K. Lu, J.T. Wang, and D. Wei. Microhardness and fracture properties of nanocrystalline ni-p alloys. *Scripta Metallurgica et Materialia*, 24:2319–2323, 1990.
- [35] Honggang Jiang, Y. Theodore Zhu, Darryl P. Butt, Igor V. Alexandrov, and Terry C. Lowe. Microstructural evolution, microhardness and thermal stability of hpt-processed cu. *Materials Science and Engineering*, A290:128138, 2000.
- [36] Hans J. Fecht. Nanostructured materials and composites prepared by solid state processing. In Carl C. Koch, editor, *Nanostructured Materials - Processing, Properties and Potential Applications*, pages 73–113, Norwich, New York, U.S.A., 2002. William Andrew Publishing Noyes.

- [37] Julia R. Weertman. Mechanical behaviour of nanocrystalline metals. In Carl C. Koch, editor, *Nanostructured Materials - Processing, Properties and Potential Applications*, pages 397–421, Norwich, New York, U.S.A., 2002. William Andrew Publishing Noyes.
- [38] S. Cheng, J.A. Spencer, and W.W. Milligan. Strength an tension/compression asymmetry in nanstructured and ultrafine metals. *Acta Materialia*, 51:4505–4518, May 2003.
- [39] J.R. Weertman. Hall-petch strengthening in nanocrystalline metals. *Materials Science and Engineering*, A166:161–167, 1993.
- [40] G.W. Nieman, J.R. Weertman, and R. W. Siegel. Mechanical behavior of nanocrystalline cu and pd. *Journal of Materials Research*, 6(5):1012–1027, May 1991.
- [41] P.G. Sanders, J.A. Eastman, and J.R. Weertman. Pore distribution in nanocrystalline metals from small angle neutron scattering. *Acta Materialia*, 46(12):4195–4202, 1998.
- [42] L. Lu, M. L. Sui, and K. Lu. Superplastic extensibility of nanocrystalline sopper at room temperature. *Science*, 287(5457):1463–1466, February 2000.
- [43] Lei Lu, Yongfeng Shen, Xianhua Chen, Lihua Qian, and K. Lu. Ultrahigh strength and high electrical conductivity in copper. *Science*, 304:422, 2004.
- [44] A.L. Ortiza and L. Shawb. X-ray diffraction analysis of a severely plastically deformed aluminum alloy. *Acta Materialia*, 52:2185–2197, 2004.
- [45] P.G. Sanders, J.A. Eastman, and J.R. Weertman. Elastic and tensile behavior of nanocrystalline copper and apladium. *Acta Materialia*, 45:4019–4025, 1997.
- [46] A.M. Sherik, U. Erb, G. palumbo, and K.T. Aust. Deviations from hall-petch behaviour in as-prepared nanocrystalline nickel. *Scripta Metallurgica et Materialia*, 27:1185–1188, 1992.
- [47] R.Z. Valiev, F. Chmelik, F. Bordeaux, G. Kapelski, and B. Baudelet. The hall-petch relation in sub-micrograined al-1.5mg alloy. *Scripta Metallurgica et Materialia*, 27:855–860, 1992.
- [48] J. Cheng, Lu L., and Lu K. Hardness and strain rate sensitivity of nanocrystalline cu. *Scripta Materialia*, 54:1913–1918, 2006.
- [49] Khaled M. Youssef, Ronald O. Scattergood, K. Linga Murty, and Carl C. Koch. Ultratough nanocrystalline copper with a narrow grain size distribution. *Appl. Phys. Lett.*, 85:929–931, 2004.

- [50] R. Suryanarayanan Iyer, Claire A. Frey, S.M.L. Sastry, B.E. Waller, and W.E. Buhro. Plastic deformation of nanocrystalline cu and cu0.2 wt. *Materials Science and Engineering*, A264:210–214, 1999.
- [51] S.R. Agnew, B.R. Elliott, C.J. Youngdahl, K.J. Hemker, and J.R. Weertman. Microstructure and mechanical behavior of nanocrystalline metals. *Materials Science and Engineering*, A285:391–396, 2000.
- [52] G.T. Gray, T.C. Lowe, C.M. Cady, R.Z. Valiev, and I.V. Aleksandrov. Influence of strain rate & temperature on the mechanical response of ultrafine-grained cu, ni, and al-4cu-0.5zr. *Nanostructured Materials*, 9:477–480, 1997.
- [53] Valiev R.Z., Kozolv E.V., Ivanov Yu F., Lian J., Nazarov A.A., and Baudalet B. *Acta Materialia*, 42:2467, 1994.
- [54] M. Haouaoui, I. Karaman, H.J. Maier, and K.T. Hartwig. Microstructure evolution and mechanical behavior of bulk copper obtained by consolidation of micro- and nanopowders using equal-channel angular extrusion. *Metallurgical and Materials Transactions A*, 35A:2935, 2004.
- [55] Meyers M.A. and Chawla K.K. *Mechanical behavior of materials*. Prentice-Hall, Englewood Cliffs (NJ), 1980.
- [56] E. Ma. Instabilities and ductility of nanocrystalline and ultrafine-grained metals. *Scripta Materialia*, 49:663–668, 2003.
- [57] F. Ebrahimi, Q. Zhai, and D. Kong. Deformation and fracture of electrodeposited copper. *Scripta Materialia*, 39:315–321, 1998.
- [58] K. Hayashi and H. Etoh. *Metall Trans JIM*, 309:925, 1989.
- [59] G.W. Nieman, J.R. Weertman, and R.W. Siegel. Tensile strength and creep properties of nanocrystalline paladium. *Scripta Metallurgica et materialia*, 24:146–150, 1990.
- [60] Y.M. Wang. Microsample. *Scripta Materialia*, 48:1581–1586, 2003.
- [61] Ning Wang, Zhirui Wang, K.T. Aust, and U. Erb. Room temperature creep behavior of nanocrystalline nickel produced by and electrodeposition technique. *Materials Science and Engineering A*, 237:150–158, 1997.
- [62] J. Markmann, P. Bunzel, H. Rosner an K.W. Liu, K.A. Padmanabhan, R. Birringer, H. Gleiter, and J. Weissmuller. Microstructure evolution during rolling of inert-gas condensed palladium. *Scripta Materialia*, 49:637, 2003.

- [63] Thomas H. Courtney. *Mechanical Behavior of Materials*, chapter High Temperature Deformation of Crystalline Materials, page 302. McGraw-Hill, New York, 1999, 2 edition.
- [64] Y.Estrin, G. Gottstein, and L.S. Shvindlerman. Diffusion controlled creep in nanocrystalline materials under grain growth. *Scripta Materialia*, 50:993–997, 2004.
- [65] Kai Zhang, J. R. Weertman, and J. A. Eastman. The influence of time, temperature, and grain size on indentation creep in high-purity nanocrystalline and ultrafine grain copper. *Appl. Phys. Lett.*, 82:5197, 2004.
- [66] M. Jin, A.M. Minor, E.A. Stach, and J.W. Morris Jr. Direct observation of deformation-induced grain growth during the nanoindentation of ultrafine-grained al at room temperature. *Acta Materialia*, 52:5381–5387, 2004.
- [67] Khaled M. Youssef, Ronald O. Scattergood, K. Linga Murty, Joseph A. Horton, and Carl. C. Koch. Ultrahigh strength and high ductility of bulk nanocrystalline copper. *Appl. Phys. Lett.*, 87:091904, 2005.
- [68] M. Dao, L. Lu, K.W. Liu, H. Rosner, R.J. Asaro, J.T.M. De Hosson, and E. Ma. Toward a quantitative understanding of mechanical behavior of nanocrystalline metals. *Acta Materialia*, 55:4041–4065, 2007.
- [69] Kevin J. Hemker. Understanding how nanocrystalline metals deform. *Science*, 304:221–222, April 2004.
- [70] Zeljka Budrovic, Helena Van Swygenhoven, Peter M. Derlet, Steve Van Petegem, and Bernd Schmidt. Plastic deformation with reversible peak broadening in nanocrystalline nickel. *Science*, 304:273–276, April 2004.
- [71] Migwei Chen, En Ma, Kevin J. hemker, HongWei Sheng, Yinmin Wang, and Xuemei Cheng. Deformation twinning in nanocrystalline aluminum. *Science*, 300:1275–1277, May 2003.
- [72] X. Wu, Y.T. Zhu, M.W. Chen, and E. Ma. Twinning and stacking fault formation during tensile deformation of nanocrystalline ni. *Scripta Materialia*, 54:1685–1690, 2006.
- [73] Veselin Yamakov, Dieter Wolf, Simon R. Phillpot, and Amiya K. Mukherjee. Dislocation processes in the deformation of nanocrystalline aluminium by molecular-dynamics simulation. *Nature Materials*, 1:45–49, September 2002.
- [74] Jørgen B. Sørensen and Jakob Schiøtz. Nanocrystal get twins. *Science*, 300:1244–1245, May 2003.

- [75] Jens Kroger. Elastic behavior and freezing of crystals with square symmetry. Master's thesis, McGill University, 2005.
- [76] Helena Van Swygenhoven. Grain boundaries and dislocations. *Science*, 296:66–67, April 2002.
- [77] J. Schiøtz, Francesco D. Di Tolla, and Kasten W. Jacobsen. Softening of nanocrystalline metals at very small grain sizes. *Nature*, 391:561–563, February 1998.
- [78] Johannes Weertman and Julia R. Weertman. *Elementary Dislocation Theory*, chapter 4, pages 99–103. Oxford University press, Oxford, 1992.
- [79] V. Yamakov, D. Wolf, M. Salazar, S. R. Phillpot, and H. Gleiter. Length-scale effects in the nucleation of extended dislocations in nanocrystalline al by molecular dynamics simulation. *Acta materialia*, 49:2713–2722, 2001.
- [80] D. Wolf, V. Yamakov, S.R. Phillpot, A. Mukherjee, and H. Gleiter. Deformation of nanocrystalline materials by molecular-dynamics simulation: relationship to experiments? *Acta Materialia*, 53:1–40, 2005.
- [81] V. Yamakov, D. Wolfz, and S. R. Phillpot. Deformation mechanism crossover and mechanical behaviour in nanocrystalline materials. *Philosophical Magazine Letters*, 83:385393, 2003.
- [82] Jakob Schiøtz and Karsten W. Jacobsen. A maximum in the strength of nanocrystalline copper. *Science 5 September 2003*., 301:1357 – 1359, 2003.
- [83] H. Van Swygenhoven. Footprints of plastic deformation in nanocrystalline metals. *Materials Science and Engineering A*, 483-484:33–39, 2008.
- [84] D. Hull and D.J. Bacon. *Introduction to dislocations*, page 231. Butterworth-Heinemann, Liverpool, UK, 4 edition, 2001.
- [85] J. Heslop and N.J. Petch. Dislocation locking and fracture in α -iron. *Philosophical Magazine*, 2:649–658, 1957.
- [86] N.J. Petch and A. Crackell. Frictional forces on dislocation arrays at the lower yield point in iron. *Acta Metallurgica*, 3:186–189, 1995.
- [87] Satoshi Ichikawa, Kun'ichi Miyazawa, Hideki Ichinose, and Kunio Ito. The microstructure of deformed nanocrystalline ag and ag/fe alloy. *Nanostructured Materials*, 11(8):1301–1311, 1999.

- [88] Robert J. Asaro, Peter Krysl, and Bimal Kad. Deformation mechanism transitions in nanoscale fcc metals. *Philosophical Magazine Letters*, 83:733–743, 2003.
- [89] S.V. Bobylev, M. Yu. Gutking, and I.A. Ovidko. Transformation of grain boundaries in deformed nc materials. *Acta Materialia*, 52(13):3793–3805, August 2004.
- [90] K. Lu and M. L. Siu. An explanation to the abnormal hall-petch relation in nanocrystalline materials. *Scripta Metallurgica et Materialia*, 28:1465–1470, 1993.
- [91] H. Van Swygenhoven, D. Farkas, and A. Caro. Grain boundary structures in polycrystalline metals at the nanoscale. *Phys. Rev. B*, 62(2):831–838, July 2000.
- [92] H. Van Swygenhoven, D. Farkas, and A. Caro. A molecular dynamics study of polycrystalline fcc metals at the nanoscale. *Materials Science and Engineering*, 309-310:440–444, 2001.
- [93] J. Weertman and J. R. Weertman. *Physical Metallurgy*, chapter 20, pages 1332–1333. North-Holland, Amsterdam, 1965.
- [94] H. Hahn, P. Mondal, and K.A. Padmanabhan. Plastic deformation of nanocrystalline materials. *Nanostructured Materials*, 9:603–606, 1997.
- [95] I.A Ovidko. Deformations of nanostructures. *Science*, 295:2386, March 2002.
- [96] D. A. Porter and K. E. Easerling. *Phase Trnasformations in Metals and Alloys*. Chapman & Hall, London, 1992.
- [97] John W. Cahn. Phase separation by spinodal decomposition in isotropic systems. *The Journal of Chemical Physics*, 42:93, 1965.
- [98] Francois Leonard and Rashmi C. Desai. Spinodal decomposition and dislocation lines in thin films and bulk materials. *Phys. Rev. B*, 58:8277, 1998.
- [99] John W. Cahn. Hardening by spinodal decomposition. *Acta Metallurgica*, 11:1275–1282, 1963.
- [100] Masaharu Kato, T. Mori, and L.H. Schwartz. Hardening by spinodal modulated structure. *Acta Metallurgica*, 28:285–290, 1979.
- [101] John W. Cahn. Nucleation on dislocations. *Acta Metallurgica*, 5:169, 1957.
- [102] C. C. Dollins. Nucleation on dislocations. *Acta Metallurgica*, 18:1209–1215, 1970.

- [103] Mikko Haatajaa, Jennifer Mahon, Nikolas Provatas, and Francois Léonard. Scaling of domain size during spinodal decomposition: Dislocation discreteness and mobility effects. *Appl. Phys. Lett.*, 87:251901, 2005.
- [104] J. T. Plewes. High-strength cu-ni-sn alloys by thermomechanical processing. *Metallurgical and Materials Transactions A*, 6:537–544, 1975.
- [105] Fatma M. Helmi and Lehel Zsoldos. On the thermal decomposition of cu-ni-sn after prior cold-work. *Scripta Metallurgica*, 11:899, 1977.
- [106] Stephen Spooner and Bruce G. Lefevre. Effect of prior deformation on spinodal age hardening in cu-15 ni-8 sn alloy. *Metallurgical Transactions A*, 11A:1085–1093, 1980.
- [107] J.A. Dantzig. Multiscale methods, moving boundaries and inverse problems. Institute for Pure and Applied Mathematics; workshop - online publication, 2003.
- [108] Akusti Jaatinen. Applicability of the phase field crystal model in predicting phase diagrams. Master's thesis, Helsinki University of Technology, 2006.
- [109] R. Evans. The nature of the liquid-vapor interface and other topics in the statistical mechanics of non-uniform, classical fluids. *Advances in Physics*, 28:143–200, 1979.
- [110] Yashwant Singh. Density functional theory of freezing and properties of the ordered phase. *Physics Reports*, 207:351–444, 1991.
- [111] P. Stefanovic, M. Haataja, and N. Provatas. Phase-field crystals with elastic interactions. *TMS Letters*, 3:69–70, 2006.
- [112] Herbert Goldstein, Charles P. Poole, and John L. Safko. *Classical Mechanics*. Addison Wesley, 2001.
- [113] A. H. Cottrell. *The mechanical Properties of Matter*. Willey and Sons, New York, London, Sydney, 1964.
- [114] K. R. Elder, Nikolas Provatas, Joel Berry, Peter Stefanovic, and Martin Grant. Phase field crystal modeling and classical density functional theory of freezing. *Phys. Rev. B*, 75:064107, 2007.
- [115] Kuo-An Wu, Alain Karma, Jeffrey J. Hoyt, and Mark Asta. Ginzburg-landau theory of crystalline anisotropy for bcc-liquid interfaces. *Phys. Rev. B*, 73:094101, 2006.

- [116] W.H. Press, S.A. Teukolsky, W.T. Vetterling, and B.P. Flannery. *Numerical Recipes in Fortran 77*. Cambridge University Press, Cambridge, 1992.
- [117] U. Trottenberg, C.W. Oosterlee, and A. Schuller. *Multigrid*. Academic Press, London, 2001.
- [118] J. Kim, K. Kang, and J. Lowengrub. Conservative multigrid methods for cahn-hilliard fluids. *Journal of Computational Physics*, 193:511–543, 2004.
- [119] T. C. Lubensky, Sriram Ramaswamy, and John Toner. Hydrodynamics of icosahedral quasicrystals. *Phys. Rev. B*, 32(11):7444–7452, Dec 1985.
- [120] K. Kaski, A. Kuronen, and M. Robles. Dynamics of dislocations in a two-dimensional system. In *Computer Simulation Studies in Condensed Matter Physics XIV*. Springer Verlag, 2001.
- [121] W. G. Johnston and J. J. Gilman. Dislocation velocities, dislocation densities, and plastic flow in lithium fluoride crystals. *Journal of Applied Physics*, 30:129, 1959.
- [122] Daniel Post. Chapter iv photoelasticity. *Experimental Mechanics*, 6(8):19A–38A, 1966.
- [123] J.F. Knot and B. Met. *Fundamentals of Fracture Mechanics*. Butterworths, London, 1973.
- [124] F. Baratta and D. Neal. Stress-concentration factors in u-shaped and semi-elliptical edge notches. *The Journal of Strain Analysis for Engineering Design*, 5:121–127, 1970.
- [125] M. Murayama, J. M. Howe, H. Hidaka, and S. Takaki. Atomic-level observation of disclination dipoles in mechanically milled, nanocrystalline fe. *Science*, 295(5564):2433–2435, 2002.
- [126] Peter Haasen. *Phase Transformations in Materials*, volume 5, of *Materials Science and Technology: A Comprehensive Treatment*, chapter 7 Spinodal Decomposition, page 436. VCH, Weinheim, 1991.
- [127] Joel Berry, K. R. Elder, and Martin Grant. Melting at dislocations and grain boundaries: A phase field crystal study. *Physical Review B (Condensed Matter and Materials Physics)*, 77(22):224114, 2008.
- [128] Paul D. Fleming III and Claude Cohen. Hydrodynamics of solids. *Phys. Rev. B*, 13:500–516, 1976.

- [129] Rob Phillips. *Crystals, defects and microstructures. Modeling across scales.* Cambridge University Press, Cambridge, 2001.